Aus der Klinik für Neurologie

Direktor: Univ.-Prof. Dr. med. Lars Timmermann, FEAN

des Fachbereichs Medizin der Philipps-Universität Marburg
in Zusammenarbeit mit:
der Technischen Hochschule Mittelhessen, Gießen, DE

7-Tesla-Ultrahochfeld-Magnetresonanztomographie im Kopf- und Halsbereich mittels 64-Kanal-Signaldetektion und integrierter paralleler 16-Kanal-Sendespule

Inaugural-Dissertation

zur
Erlangung des Doktorgrades der Medizinwissenschaften
(Dr. rer. med.)
an dem Fachbereich Medizin der Philipps-Universität Marburg
vorgelegt von

Markus W. May
aus Bamberg

Marburg, 2022

Angenommen vom Fachbereich Medizin der Philipps-Universität Marburg
am: 31.08.2022
Gedruckt mit Genehmigung des Fachbereichs Medizin

Dekanin:	Prof. Dr. Denise Hilfiker-Kleiner
Referent:	Prof. Dr. med. Susanne Knake
	Prof. Dr. rer. physiol. Boris Keil
1. Korreferent:	Prof. Dr. Martin Fiebich

Für die Familie

Die vorliegende kumulative Dissertation stellt eine Zusammenfassung der Forschungsergebnisse dar, die in den folgenden Publikationen in PubMed-gelisteten internationalen Fachzeitschriften veröffentlicht wurden (*klickbar*):

[1] **May, Markus W.**, Sam-Luca JD Hansen, Mirsad Mahmutovic, Alina Scholz, Nicolas Kutscha, Bastien Guerin, Jason P Stockmann, Robert L. Barry, Ehsan Kazemivalipour, Rene Gumbrecht, Ralph Kimmlingen, Markus Adriany, Yulin Chang, Christina Triantafyllou, Susanne Knake, Lawrence L Wald, Boris Keil. *A Patient-Friendly 16-Channel Transmit/ 64-Channel Receive Coil Array for Combined Head-Neck Magnetic Resonance Imaging at 7 Tesla.* In: Magn Reson Med. 2022; DOI: 10.1002/mrm.29288

[2] Ghotra, Anpreet; Kosakowski, Heather L.; Takahashi, Atsushi; Etzel, Robin; **May, Markus W.**; Scholz, Alina; Jansen, Andreas; Wald, Lawrence L.; Kanwisher, Nancy; Saxe, Rebecca; Keil, Boris. *A size-adaptive 32-channel array coil for awake infant neuroimaging at 3 Tesla MRI.* In: Magn Reson Med. 2021;86:1773–1785. DOI: 10.1002/mrm.28791

[3] Scholz, Alina; Etzel, Robin; **May, Markus W.**; Mahmutovic, Mirsad; Tian, Qiyuan; Ramos-Llorden, Gabriel; Maffei, Chiara; Bilgic, Berkin; Witzel, Thomas; Stockmann, Jason P.; Mekkaoui, Choukri; Wald, Lawrence L.; Yi Huang, Susie; Yendiki, Anastasia; Keil, Boris. *A 48-channel receive array coil for mesoscopic diffusion-weighted MRI of ex vivo human brain on the 3T Connectome scanner.* In: NeuroImage. 2021;231:118256. DOI: 10.1016/j.neuroimage.2021.118256

Alle Publikationen der vorliegenden Dissertation sind online verfügbar und jeweils mit einer Abdruckgenehmigung ([1, 2] John Wiley and Sons Inc.; [3] Elsevier Inc.) versehen.

Inhaltsverzeichnis

Abkürzungsverzeichnis

AI	*Artificial Intelligence*
DL	*Deep Learning*
DW-MRT	Diffusionsgewichtete-MRT
EEG	Elektroenzephalografie
FDA	*United States Food and Drug Administration*
fMRT	funktionale Magnetresonanztomografie
FID	*Free Induction Decay*
FOV	Bildfeld /engl.: Field of View
HF-Puls	Hochfrequenz-Puls
MR	Magnetresonanz
MRI	*Magnetic Resonance Imaging*
MRT	Magnetresonanztomographie
MTRA	Medizinisch-Technische/r Radiologieassistent/in
pTx	*Parallel RF Transmission*
RID	Resonante Induktive Entkopplung /engl.: *Ressonance Inductive Decoupling*
ROI	Bereich von Interesse /engl.: *Region of Interest*
SAR	spezifische Absorptionsrate /engl.: *Specific Absorption Rate*
SNR	Signal-Rausch-Verhältnis /engl.: *Signal Noise Ratio*
T	Tesla
UHF-MRT	Ultrahochfeld-Magnetresonanztomographie
z.B.	zum Beispiel

Zusammenfassung

Die Magnetresonanztomographie (MRT) hat sich als wertvolles Diagnosewerkzeug im klinischen Alltag gezeigt und sich seit seiner Einführung konstant weiterentwickelt. So wurde erst kürzlich der erste 7 T-MRT durch die United States Food and Drug Administration zur klinischen Nutzung freigegeben. Mit einer höheren Magnetfeldstärke ändern sich die physikalischen Effekte und Parameter, die eine positive (kontrastverstärkende Auswirkung), aber auch eine negative (artefaktverstärkende) Auswirkung auf die Bildgebung haben können. So ist es aus technischen Gründen derzeit noch nicht möglich, eine Ganzkörperaufnahme bei einer Feldstärke von 7 T zu generieren, wie es beispielsweise bei 1,5 T möglich ist. Die derzeitige Bildgebung bei 7 T-MRTs beschränkt sich hauptsächlich auf lokale Bereiche wie z.B. das Gehirn, oder das Fuß-, Arm- oder Kniegelenk. Auf Basis der großen Nachfrage aus dem klinischen Bereich, das Bildfeld zu erweitern, ergibt sich die Fragestellung dieser Dissertation:

Ist es möglich, mit dem aktuellen Stand der Technik unter Berücksichtigung der maximal verfügbaren Sende- und Empfangskanäle, die ein derzeitiges kommerzielles 7 T-MRT bietet, ein Bildfeld zu generieren, welches den Kopf- und Halsbereich abdeckt?

Diese Fragestellung wurde durch die Entwicklung von morphologisch angepassten Signalgeneratoren als auch Signaldetektoren gelöst. Das Bildfeld wurde von der Gehirnregion auf den Halsbereich bei 7 T erweitert. Die entwickelte Hardware wurde entworfen, simuliert, konstruiert, getestet und mit einer kommerziell verfügbaren 7 T Gehirnspule verglichen. Ein Fortschritt zum aktuellen Stand der Technik wurde quantifiziert.

Die neu entwickelten Methoden zur Gestaltung und Konstruktion der Sende- und Empfangsstruktur bei 7 T, als auch die zur Prüfung der Funktionalität verwendete Hardware, wurde direkt in abgewandelter Form bei ähnlichen MRT-Forschungsprojekten bei einer Feldstärke von 3 T verwendet und publiziert.

Zusammenfassend wurde mit diesem Projekt sowohl der Grundstein für die klinische Bildgebung als auch für weitere Forschung im kombinierten Kopf- und Halsbereich bei der 7 T-MRT gelegt. Der Einfluss dieses Projekts wird sich voraussichtlich in den nächsten Jahren in klinischen Studien zeigen. Limitierende Faktoren wie beispielsweise die spezifische Absorptionsrate /engl.: *Specific Absorption Rate* (SAR) können durch Softwaremaßnahmen und der Ansteuerung der Spulen in weiteren Doktorarbeiten optimiert werden, um den Bildgebungsprozess zu optimieren.

Abstract

Magnetic Resonance Imaging (MRI) has proven to be a valuable diagnostic tool in everyday clinical practice and has constantly evolved since its introduction. For example, the first MRI was recently cleared for clinical use by the United States Food and Drug Administration. With a higher magnetic field strength, the physical effects and parameters change, which can have a positive (contrast enhancing effect) but also a negative (artifact enhancing) effect on the imaging process. For example, for technical reasons, it is not currently possible to generate a whole-body image at a field strength of 7 T, as is possible at 1,5 T, for example. Current imaging at 7 T MRIs is mainly limited to local areas such as the brain, foot, arm, or knee joint. Based on the great demand from the clinical field to extend the Bildfeld /engl.: Field of View (FOV), the research question of this dissertation arises:

With the current state of the art, considering the maximum available transmit and receive channels offered by a current commercial 7 T-MRI, is it possible to generate a FOV covering the head and neck region?

This problem was solved by the development of morphologically adapted signal generators as well as signal detectors. The FOV was extended from the brain region to the neck region at 7 T. The developed hardware was designed, simulated, constructed, tested, and compared with a commercially available 7 T Brain Coil. An advance on the current state of the art was quantified.

The newly developed methods for designing and constructing the transmit and receive structure at 7 T, as well as the hardware used to test its functionality, have been directly used and published in modified form in similar MRI research projects at a field strength of 3 T.

In summary, this project has laid the foundation for both clinical imaging and further research in the combined head and neck region for 7 T-MRI. The impact of this project is expected to be seen in clinical trials over the next few years. Limiting factors such as SAR can be optimized by software measures and the control of the coils in further PhD work to optimize the imaging process.

1 Einleitung

Die Verbesserung des Bestehenden ist ein kontinuierliches Ziel der Forschung. Der Gewinn von Wissen bietet die Möglichkeit, bessere Entscheidungen zu treffen. Dem richtigen Tun geht dem richtigen Wissen voraus. [Jar15, S.32]
Um an das neue geschaffene Wissen durch die drei vorliegenden Publikationen heranzuführen, sollen in den nächsten Kapiteln, unter Berücksichtigung der formalen Kriterien, das vorangegangene Wissen als Grundlage beschrieben werden.

1.1 Allgemeine Grundlagen der Magnetresonanztomographie

Die Magnetresonanztomographie (MRT), wie sie heute weltweit im klinischen Alltag Verwendung findet, startete im Jahr 1973 mit P. C. Lauterbur [Lau73]. Er publizierte das erste Bild aus einer Magnetresonanz (MR)-Messung. Zusammen mit Sir P. Mansfield, der im Jahr 1977 das erste *in vivo*-Bild eines Fingers publizierte [Man77], erhielten beide den Nobelpreis für Medizin im Jahr 2003 für die „Abbildung mit MR“ [Nob03].
Die MRT nutzt den Eigendrehimpuls $\vec{J}$ (der auch als Präzession oder Kernspin bezeichnet wird) von Atomen mit ungerader Nukleonenzahl. Der Kernspin ist eine bewegte Ladung und erzeugt folglich ein proportionales magnetisches Moment $\vec{\mu}$. Dieses proportionale Verhältnis kann über das gyromagnetische Verhältnis γ dargestellt werden: $\vec{\mu} = \gamma\vec{J}$

Dieses magnetische Moment gilt für Elemente mit ungerader Nukleonenanzahl, da $\vec{J}$ sonst nach außen ausgeglichen wird. In der allgemeinen klinischen MRT wird vornehmlich ^{1}H-Wasserstoff zur Bildgebung genutzt, da der menschliche Körper viel Wasserstoff enthält und das gyromagnetische Verhältnis $\gamma = 2\pi 42,577\frac{MHz}{T}$ von allen stabilen Isotropen bei Wasserstoff am größten ist. Folglich ist hier $\vec{\mu}$ selbst in einer ‘normalen‘ Umgebung am größten. In dieser ‘normalen‘ Umgebung in der nur das Erdmagnetfeld eine externe Magnetisierung darstellt, ist ein sehr schwaches magnetisches Moment messbar. [Moh04]
Wird ein stärkeres statisches magnetisches Feld B_0 von beispielsweise 1,5 Tesla(T) angelegt, zeigt sich eine stärkere Magnetisierung in Richtung des angelegten Magnetfelds, die für die klinische Bildgebung interessanter ist. Die Frequenz der präzedierenden Spins wird als Kreisfrequenz ω_{Larmor} mit dem gyromagnetischen Verhältnis γ im Magnetfeld B_0 und Larmorfrequenz f_{Larmor} definiert: $\omega_{Larmor} = \gamma B_0$

Durch das Senden von Anregungspulsen, auch Hochfrequenz-Puls (HF-Puls) genannt, über die Sendespule wird das B_1^+-Feld erzeugt. In einer sich in der Nähe befindenden Empfangsspule (Rx), wird ein Empfangssignal aus dem *engl.: Free Induction Decay (FID)* induziert, welches die Grundlage der Bildrekonstruktion bildet. [McR06]
Das Empfangssignal besitzt ein besseres Signal-Rausch-Verhältnis /engl.: *Signal Noise Ratio* (SNR) umso höher die Magnetfeldstärke ist: SNR $\sim B_0^{1,65}$ [Poh16].

Die MRT lässt sich verkürzt in drei Schritten darstellen:
1. Anregung der Zielregion 2. Räumliche Kodierung 3. Signalempfang und Verarbeitung
Jeder Schritt hat seine Herausforderungen mit Einfluss auf das Ergebnis. Allerdings ist es die Anregung der Zielregion und das damit verbundene B_1^+-Feld, welches bei der Ultrahochfeld-Magnetresonanztomographie (UHF-MRT) bei 7 T die größte Herausforderung darstellt. Um auf die Bedeutung der Anregung und die Auswirkungen und Möglichkeiten des B_1^+-Felds bei der UHF-MRT einzugehen, wird die Sendetechnik im nächsten Abschnitt kurz dargestellt.

1.2 Sendetechnik: B_1^+ Modulation durch Shimming

Bei der UHF-MRT bei 7 T ist die Larmorfrequenz in der Praxis ca. 300 MHz und somit die Frequenz, auf die eine Sendespule eingestellt wird. Diese Einstellung wird mit der Veränderung der in Reihe geschalteten Kondensatoren in der Sendespule vorgenommen und definieren die Kapazität C. Eine Induktivität L wird durch die Leiterbahn selbst erzeugt und ist vor allem abhängig von den Dimensionen der Leiterbahn. Die Leiterschleife kann vereinfacht als Parallelschwingkreis mit f_0 wie folgt dargestellt werden: $f_0 = \frac{1}{2\pi\sqrt{LC}}$.

Bei der Konstruktion einer Sendespule ist eine hohe Sendeeffizienz gewünscht. Das bedeutet, dass möglichst viel der Input-Energie eines Sendeelements in das Messobjekt übertragen wird. Eine hohe Sendeeffizienz wird durch eine gute Entkopplung der Elemente untereinander gefördert. Des Weiteren sind die Stabilität als auch ein gering erzeugtes SAR-Feld Ziele eines Sendespulendesigns. Aufgrund dieser Zielsetzung wird bei 7 T ein dezidiertes Sendespulendesign für unterschiedliche Körperregionen verwendet.

Die Sendeelemente haben das Ziel, ein möglichst homogenes B_1^+-Feld zu erzeugen. Die Wellenlänge im menschlichen Körper ist bei 7 T ~ 11 cm. Wenn das Verhältnis der Größe des Messobjekts L zur Wellenlänge im Objekt λ_o größer oder gleich 1 ist ($\frac{L}{\lambda_o} \geq 1$), kommt es durch überlagernde Wellen zur Auslöschung des B_1^+-Felds. [Bar90] Dies resultiert in nicht angeregten Bereichen und damit zu dunklen Bereichen im Bild, was eine grundsätzliche Herausforderung der UHF-MRT darstellt. [Moo05, Run22]

Um dieses Problem zu beheben, wurden bereits Hardware-Lösungen bei 4 T [Als98] und bei 7 T [Yan06] mit dielektrischen Polstern gezeigt. Am effektivsten ist die Verwendung von mehreren Sendeelementen in Kombination mit individuellen HF-Pulsen, genannt *Parallel RF Transmission* (pTx) [Ibr00, Hou00b, Kat06, Zhu04]. Um eine pTx-Sequenz zu verwenden, ist eine Infrastruktur am MRT nötig, die alle Sendeelemente unabhängig voneinander mit einer Ansteuerungszeit im Mikrosekunden-Bereich steuern kann.

Die einfachste und zugleich weit verbreitetste Form von pTx ist die statische B_1^+-Modulation, auch "Shimming" genannt [Mao06, Pad16]. Wenn auf das i-te Sendeelement ein Puls gegeben wird, wird ein magnetisches Feld $B_{1,i}^+(r,t)$, sowie ein elektrisches Feld $E_i(r,t)$ erzeugt, wobei sich das erzeugte Magnetfeld:

$B^+_{1,i}(r,t) = 0.5[B^x_{1,i}(r,t) + jB^y_{1,i}(r,t)]$ mit $j = \sqrt{-1}$ aus den räumlichen Orientierungen x und y zusammensetzt, die senkrecht zum statischen Magnetfeld B_0 sind [Hou00a]. Statisches pTx kann dargestellt werden, durch

$$B^+_{1,i}(r,t) = p(t) \sum_{i=1}^{N_T} \omega_i S_i(r) \tag{1.1}$$

wobei ein Puls p(t), der unverändert auf alle Sendekanäle N_T und durch einen komplexen Faktor ω_i individuell skaliert wird. $S_i(r)$ stellt hierbei den individuellen Einflussfaktor mit dem erzeugten $B^+_{1,i}(r,t)$-Feld des jeweiligen Kanals dar. $S_i(r)$ wird in einer vorherigen Messung normiert ermittelt. Beispielsweise wird das i-te Element mit einer definierten Amplitude (zum Beispiel (z.B.) 1 V) angesteuert, wobei alle anderen Kanälen ausgeschaltet sind (0 V). Diese Messung wird mit allen Sendeelementen wiederholt und so jeder Einflussfaktor $S_i(r)$ vorab ermittelt.

Die generierten Felder haben einen maßgeblichen Einfluss auf die SAR-Grenzwerte [Col11]. SAR ist ein sicherheitsrelevanter Parameter der zur Erwärmung des Gewebes führt und deren Grenzwerte sind in der aktuellen Version 3.2 der IEC 60601-2-33 aus dem Jahr 2015 festgehalten. [Com15] Aufgrund dieser Grenzwerte ist das derzeit einzige klinische 7 T-UHF-MRT noch nicht für alle Körperbereiche freigegeben. SAR ist bei der pTx-MRT besonders kritisch. Das elektrische Gesamtfeld spielt hierbei eine wichtige Rolle. Es setzt sich aus einer linearen Überlagerung der Felder jedes Sendekanals zusammen. Das elektrische Gesamtfeld ist zeitlich und räumlich variabel, wodurch an unerwarteten Stellen "Hot Spots" entstehen können. Um sicherzustellen, dass diese Bereiche nicht über den zulässigen Grenzwerten liegen, muss das Spulensystem simuliert werden.

SAR wird entweder gemittelt über ein 10 g-Gewebevolumen oder über das exponierte Volumen, in der Simulation dargestellt und zur Überwachung der Sicherheit und zum Entwurf von pTx-Pulsen verwendet. Es dient dazu die max. Spannung zu ermitteln, welche auf das System gegeben werden kann, um die SAR-Grenzwerte einzuhalten. Die Anzahl an verteilten Sendeelementen kann hierbei durch individuelle Steuerung und somit weiteren Freiheitsgraden helfen, das SAR zu reduzieren. [Lat09]

1.3 Empfangstechnik: Parallele Bildgebung

Nach der Anregungsphase und dem Deaktivieren der Sendespulen über eine Bias-Gleichspannung und einer Diode werden die Empfangselemente resonant geschaltet. Dieser Modus wird Empfangsmodus genannt. Im Empfangsmodus induziert die rotierende Quermagnetisierung der Spins einen elektrischen Strom in der Empfangsspule, der das MR-Signal darstellt.

Das Ziel von Empfangsspulen ist, ein möglichst hohes SNR, woraus ein hohes Empfangssignal mit gutem Bildkontrast folgt. [Hou76, RW00] Theoretisch könnte die Sendespule auch als Empfangsspule interagieren, darunter würde jedoch das SNR leiden. Deswegen werden in der aktuellen klinischen Bildgebung hauptsächlich in Sendeund Empfangsspulen getrennte Systeme verwendet. Einkanal-Empfangsspulen haben ein gutes SNR, jedoch nur im begrenzten räumlichen Umfeld dieses Elements. Dies kann mit der Installation von mehreren Empfangselementen um das Zielobjekt gelöst werden.

Die Möglichkeit der Entkopplung [Roe90] von Mehrkanal-Empfangsspulen führte zur parallelen Bildgebung, welche eine bedeutende Rolle in der Verkürzung der Aufnahmezeit als auch in der Optimierung des SNRs spielt. Die häufigste Entkopplungsmethode ist die geometrischen Entkopplung durch Überlappung der Elemente. Bei einer weiteren Methode durch eine "shared impedance" teilen sich zwei Elemente eine angrenzende Leiterbahn. Bei der induktiven Entkopplung werden induktiv-gekoppelte Spulen in den Leiterbahnen verwendet. Kapazitive Entkopplung wird durch Kondensatoren zwischen den Empfangselementen realisiert. Durch die ungleichmäßige Verteilung von Kondensatoren in einer Leiterschleife kann auch eine Entkopplung realisiert werden. Bei jeder bisher aufgezählten Methode ist eine zusätzliche Entkopplung durch Vorverstärkerentkopplung möglich [Roe90]. Eine gute Entkopplung ermöglicht eine beschleunigte Bildgebung.

Die beschleunigte Bildgebung wird durch das Auslassen von Messpunkten erzielt und nennt sich Unterabtasten. Die Unterabtastung korreliert mit einem Reduktionsfaktor R. Der R-Wert hat Einfluss auf das SNR und somit die Bildqualität

$$SNR_{Beschleunigt} = \frac{SNR_{Normal}}{g\sqrt{R}} \tag{1.2}$$

wobei g der Geometriefaktor und abhängig von der Spulenkonfiguration, der Empfangsspule, dem FOV und dem Ort der gewählten Schicht ist. [Rob08]
Um g zu ermitteln, wird im Vorfeld eine Sensitivitätsmessung durchgeführt und das Sensitivitätsprofil jedes Empfangselements ermittelt.
Hierbei ist jede Empfangsspule in der Region nahe der Spule am sensitivsten. Unter Berücksichtigung dieser Ortsinformationen aus dem Sensitivitätsprofil können Algorithmen wie SENSE [Pru99] oder GRAPPA [Gri02] den unterabgetasteten Datensatz zur Grundlage der Bildrekonstruktion machen.

Im klinischen Alltag wird die parallele Bildgebung als wertvolle Möglichkeit gesehen, die Scannzeit zu verkürzen. Die parallele Bildgebung ist kein Pulsverfahren und nicht auf eine Sequenz limitiert. Es ist ein Rekonstruktionsverfahren welche aus einem unterabgetasteten und somit beschleunigt aufgenommenen Datensatz aus nahezu jeder Art von Impulsfolge einen Datensatz rekonstruieren kann.

1.4 Stand der Technik

Die UHF-MRT bei 7 T hat im Rahmen der Bildgebung mehrere Vorteile, wie z.B. ein höheres SNR, einen höheren Kontrast zwischen den Strukturen oder kürzere Messzeiten. [Tra18, Var18, Bur21]
Die kürzliche Freigabe für das erste 7 T-MRT durch die *United States Food and Drug Administration* (FDA) zur klinischen Nutzung war ein wichtiger Schritt zur Etablierung

der UHF-MRT im klinischen Alltag, um beispielsweise Läsionen zu diagnostizieren, die bei niedrigeren MRT-Feldstärken nicht bemerkbar sind. [Fel19, Sha21]

Die höhere Magnetfeldstärke von 7 T hat durch die verkürzte Wellenlänge sowohl eine kontrast- aber auch eine artefaktverstärkende Auswirkung. Mit Anregungstechniken wie bei 1,5 T oder 3 T können sich artefaktverstärkende Auswirkungen in einem inhomogenem Bildkontrast manifestieren, diese resultieren hauptsächlich aus einem inhomogenem B_1^+-Anregungsfeld. Um diese negativen Auswirkungen zu vermindern, wurden Anregungstechniken entwickelt und angewendet, welche auf dem Prinzip des pTx[Kat06] basieren. Hierzu werden mehrere unabhängige Sendeelemente verwendet.
Als Sendespule bei 1,5 T und 3 T MRTs wird hauptsächlich die im MRT eingebaute "Birdcage" verwendet. Das Sendespulendesign bei der UHF-MRT hingegen war und ist Thema der aktuellen Forschung. [Ela22] Hier wurden bereits z.B. "loops",[Sha14] "loopoles",[Lak20] "bow ties",[Eig21] "ceramic resonators",[Aus14] "dipoles",[Raa11] "Coax-dipole",[vLe22] und andere Dipole-ähnliche Strukturen[Raa11] vorgestellt.

Um für pTx mehrere Sendeelemente gleichzeitig in der UHF-MRT verwenden zu können, müssen diese unabhängig voneinander angesteuert werden können. Im Rahmen der Anregung kann durch die Überlagerung der individuellen Felder ein vorher definiertes Anregungsfeld im FOV entstehen. Dies kann eine homogene Anregung als auch eine lokale Anregung eines 3D-selektiven Volumens sein. [Set09] Das kann mit statischem pTx geschehen. Statisches pTx ist bereits bei 7 T im Gehirn angewendet worden. [Sch14, Mar12, Cur12, Gil11, Mei22] Eine Anwendung für den Kopf- und Halsbereich ist aufgrund mangelnder Hardware noch nicht durchgeführt worden.

Ferner ist seit ca. 20 Jahren die sogenannte Mehrkanal-Empfangstechnologie [Roe90] im radiologischen Alltag bestens implementiert, welche die MR-Bildakquirierung substanziell beschleunigt [Kei11, Coh11, Kei13a]. Diese parallele Bildgebungstechnik wurde mit der simultanen Multischichtbildgebung [Fei10, Set12] erweitert. Diese Bildgebung erlaubt Scan-Zeitverkürzungen ohne signifikanten SNR-Verlust, vorausgesetzt genügend Empfangsspulenelemente sind zur Bildcodierung vorhanden. [Kei13b]. Die Entwicklung der Empfangsstrukturen bewegt sich derzeit zu einer immer größeren Anzahl an Empfangskanälen, die mit bis zu 128-Kanälen für die Gehirnbildgebung für die 7 T-UHF-MRT gipfelt. [Gru21]

Für die 7 T-Gehirnbildgebung existieren bereits seit 2006 eine kommerziell verfügbare 24- [Led06] und seit 2019 eine 32-Kanalspule mit bis zu acht Sendekanälen [Cle19]. In der 7 T-Halsbildgebung wurde das SNR einer Spule [Zha14], durch eine 22 Empfangs- und 4-Kanal-Sendespule verbessert. [Zha17] Eine kombinierte Kopf-Hals-Spuleneinheit ist jedoch aufgrund von ungelösten Problemen im MRT-Hochfrequenzengineering selbst als auch durch physikalische Hindernisse in der UHF-MRT (B_1^+-Inhomogenitäten, B_0-Modulationen, hohes SAR) sowohl in der kommerziellen MRT als auch in der Forschung noch nicht gelungen. Die Erstellung dieser Spuleneinheiten ist das primäre Ziel dieser Arbeit.

2 Zusammenfassung der peer-review Publikationen

Die vorliegende kumulative Dissertation stellt eine Zusammenfassung der Forschungsergebnisse der folgenden Publikationen dar. Diese werden in den folgenden Kapiteln zusammengefasst. Der Schwerpunkt liegt hierbei auf der Publikation [1], die im Journal ”Magnetic Resonance in Medicine” den höchsten fachbezogenen Impactfactor von 4,668 [Jez22] aufweist.

2.1 [1] A Patient-Friendly 16-Channel Transmit/ 64-Channel Receive Coil Array for Combined Head-Neck Magnetic Resonance Imaging at 7 Tesla

Die klinischen Freigabe eines UHF-MRTs für das Gehirn und Extremitäten weckte große Hoffnungen in die Verbesserung der klinischen Diagnostik. Das bessere SNR erlaubt eine höhere Auflösung und führt im Rahmen einer Früherkennung somit zu Diagnosen, die bei niedrigeren Magnetfeldstärken nicht erkannt worden wären [Fel19, Sha21]. So profitieren vor allem neurodegenerative Diagnosen zu Multiple Sklerose (MS) [Tre21, Tre19] oder Amyotrophe Lateralsklerose (ALS) [Val06] von der UHF-MRT. Die derzeitige klinische UHF-MRT beschränkt sich auf das Gehirn als auch auf Extremitäten.

Die Erweiterung des FOV vom Gehirn- auf den Halsbereich ist derzeit eine ungelöste Herausforderung. Derzeit gibt es keine Möglichkeit die UHF-MRT-Bildgebung im Kopf- und Halsbereich so patientenfreundlich wie bei der 3 T-MRT-Bildgebung zu gestalten. Die Lösung dieser Herausforderung war das Ziel dieser Hardware-fokussierten Publikation und stößt auf ökonomische Interesse durch die hier bereits finanzierte Entwicklungsarbeit.

Der aktuell kommerziell verfügbare klinische UHF-MRT-Scanner kann bis zu 16 Sendekanäle und 64 Empfangskanäle unterstützen. Derzeit gibt es kein Spulensystem, welches diese Konfiguration komplett ausnutzt. In dieser Publikation wurde eine kompakte 7 T Spulensystem für den Kopf- und Halsbereich mit 64 Empfängerelementen und einer integrierten 16-Kanal-Sendespule entworfen, konstruiert und validiert. Die Spule wurde für die Abbildung des Gehirns, des Hirnstamms, des Kleinhirns und der Halswirbelsäule optimiert, und darüber hinaus wurde der Patientenkomfort und die Benutzerfreundlichkeit bei der 7 T-UHF-MRT berücksichtigt. Die Verwendung von mehreren morphologisch angepassten Sendespulen bietet die Möglichkeit, im Rahmen der dynamischen pTx das SAR als auch das $B1^{+}$-Feld zu optimieren. Die Verwendung von Mehrkanalempfangsspulen ist wiederum eine Voraussetzung den Bildgebungsprozess im Rahmen der parallelen Bildgebung zu beschleunigen.

In der UHF-MRT wurde bisher das Sendesystem getrennt von dem Empfangssystem verwendet. [Sha14, Gao20] Dadurch wird allerdings das Sichtfeld stark beeinträchtigt und kann in manchen Fällen zu Panikattacken auch während der Datenakquisition führen. Wenn dieser Fall eintritt, muss der Bildgebungsprozess abgebrochen werden. Deswegen wurde im Designprozess der Patientenkomfort berücksichtigt und die gesamte Spule nach dem Vorbild der 3 T Kopf-Halsspule gebaut. Direkt über die Augen wurden keine Leiterelemente angebracht, um die visuelle Stimulation zu ermöglichen. Direkt über den Mund wurden Elemente ausgespart, um eine freie Atmung zu ermöglichen. Zudem wurden Bereiche, die für die Installation und Wartung benötigt werden, freigehalten. Eine Abschirmung des Spulensystems gegenüber den Gradienten wurde nicht benötigt.

Der Abstand zwischen Sende- und Empfangsspulen musste ermittelt werden. Da der Konstruktionsprozess deutlich schneller ist als der Simulationsprozess, wurde das Spulensystem für diesen Schritt konstruiert und die Kopplung direkt an der Konstruktion gemessen. [May19]

Um die Einhaltung der Sicherheitsparameter wie den SAR-Wert aus der Norm IEC 60601-2-33 zu quantifizieren, wurde die Sendespule simuliert. Es wurden die Kopplungsparameter ermittelt, welche ein Indikator für die Spuleneffizienz sind. Hohe Kopplungsfaktoren deuten darauf hin, dass die Energie von Element zu Element übertragen wird, anstatt eine Anregung im Zielobjekt zu erzeugen. Eine hohe Kopplung wurde praktisch in Publikation [1] in Abb. 5 mit Messungen an unterschiedlichen Probanden widerlegt. Die verwendete komplexe Resonante Induktive Entkopplung /engl.: *Ressonance Inductive Decoupling* (RID) wurde in einer Simulation verwendet. Es wurde das erzeugte B_1^+-Feld simuliert, wobei die Empfangsspule dieses leicht verändern kann. [Gol17] Die Simulationen mit 114 Parametern wurde manuell erfolgreich durchgeführt und bildete die Voraussetzung für den Bau-, Test- und Implementierungsprozess.

Die Halterungen, wie auch die Verschraubungen sowie das Gehäuse für das Sende- und Empfangssystem, wurden in einem CAD-Programm unter Berücksichtigung sämtlicher Kabelführungen konstruiert und mit einem 3D-Drucker hergestellt. Die beiden Systeme wurden zusammengeführt und ineinander integriert. Entkopplungsstrukturen wurden installiert und optimiert, um die Unabhängigkeit aller Spulenelemente mit geringst möglichen Signal- und Rauschkopplungen zu gewährleisten.
Die Evaluierung der 7 T-Kopf- und Halsspule erfolgte zunächst mit Prüfkörpern (Phantome) durch die Kenngrößen SNR und mit B_1^+-Felder. Nach erfolgreicher Phantomevaluierung wurde eine *in vivo* Kurzstudie mit einem Probanden zur Evaluierung des FOV vom Kopf und Halsbereich durchgeführt.

Das Potenzial des Spulendesigns zur Erweiterung des FOVs mit der Kombination aus Sende- und Empfangsspule unter Berücksichtigung des Patientenkomforts für die die klinische Anwendung der UHF-MRT wurde in dieser Arbeit durch die Aufnahme des ersten kombinierten Kopf-Halsbildes bei 7 T gezeigt (vgl. Abb. 10 in Publikation [1]).

Originalarbeit:
May, Markus W., Sam-Luca JD Hansen, Mirsad Mahmutovic, Alina Scholz, Nicolas Kutscha, Bastien Guerin, Jason P Stockmann, Robert L. Barry, Ehsan Kazemivalipour, Rene Gumbrecht, Ralph Kimmlingen, Markus Adriany, Yulin Chang, Christina Triantafyllou, Susanne Knake, Lawrence L Wald, Boris Keil. *A Patient-Friendly 16-Channel Transmit/ 64-Channel Receive Coil Array for Combined Head-Neck Magnetic Resonance Imaging at 7 Tesla.* In: Magn Reson Med. 2022;

Impact Factor: 4,668 (2020)
Eigener Anteil: 80%

Organisation des Projekts:

Planung der internationalen Kooperation, Präsentation und Moderation von monatlichen Zwischenergebnissen im internationalen Rahmen, Organisation und Reisekostenbeschaffung durch Stipendien, zeitnahe Beschaffung der Soft- & Hardware wie die benötigten nichtmagnetischen Materialien und Instrumente.

Planung, Design, Simulation, Konstruktion & Validierung:

Festlegung der Zielsetzung, Entwurf und Konstruktion mehrerer Iterationen der 3D-CAD-Modelle, virtuelle Integration von Sende- und Empfangsspulen, Prüfen der Realisierbarkeit in Verbindung mit einer Wartung oder eines Bauteilaustausches, Konzeption sowie Durchführung und iterative Optimierung der Computersimulationen, Bau und Abstimmung der Signalgenerator- und Signaldetektorspulen, Evaluation der Spulensysteme im Labor, Konstruktion von Hilfssystemen für die Messung im Labor als auch am UHF-MRT, Planung der externen Evaluation, Phantomdesign, Konstruktion des Phantoms, Konzeption und Durchführung der Messungen (mittels Phantom und *in vivo*) am UHF-MRT, Auswertung der Daten, Interpretation und Diskussion der Ergebnisse, Verfassen des Manuskripts.

2.2 [2] A Size-Adaptive 32-Channel Array Coil for Awake Infant Neuroimaging at 3 Tesla MRI

Seit Anfang des Jahres 1990 [Kwo92, Oga90] entwickelte sich die funktionale Magnetresonanztomografie (fMRT) zu einer wertvollen Methode in der klinischen, psychatrischen und neurologischen Bildgebung. Mittels fMRT können mit der normalen MRT-Hardware sensorische, motorische und kognitive Prozesse in Hirnregionen dargestellt werden.

Diese Prozesse sind besonders empfindlich, wenn sich das Gehirn in der durchschnittlich stärksten Entwicklung in den ersten Monaten nach der Geburt befindet. [Pod84] Die schnelle Zunahme des Kopfumfangs ist eine Herausforderung in der Entwicklung einer anatomisch angepassten Empfangsspule unter Berücksichtigung der festen Anzahl an Empfangskanälen und eines integrierten Gehörschutzes. Bisher wurden deshalb unterschiedliche Spulen für jeden Entwicklungsstand verwendet [Kei11], was die kommerzielle Verwendung aufgrund der erhöhten Kosten stark limitierte. Die meisten Studien an dieser jungen Probandengruppe wurden in zu großen Empfangsspulen durchgeführt, wodurch das SNR gelitten hat und die Probanden aufgrund des erhöhten Bewegungsspielraums zunächst sediert [Kon02] und später während des Schlafens [Din11, Dam14, Hug17] untersucht wurden.

In diesem Projekt wurde das Konzept eines anpassbaren 32-Kanal-Spulensystems für die pädiatrische Gehirnbildgebung ohne Sedierung realisiert. Das Spulensystem wurde mit einer kommerziellen Spule verglichen. Durch den Einsatz der parallelen Bildgebung wurde eine beschleunigte Bildverarbeitung und ein um den Faktor 2,7 höheres SNR erreicht. Somit wurde eine kindgerechte Kopfspulenanordnung entwickelt, um die räumliche Auflösung, die Empfindlichkeit, die Bewegungsunempfindlichkeit, die beschleunigte Kodierung und die Probandenverträglichkeit in der pädiatrischen MRT zu verbessern.

Originalarbeit:
Ghotra, Anpreet; Kosakowski, Heather L.; Takahashi, Atsushi; Etzel, Robin; **May, Markus W.**; Scholz, Alina; Jansen, Andreas; Wald, Lawrence L.; Kanwisher, Nancy; Saxe, Rebecca; Keil, Boris. *A size-adaptive 32-channel array coil for awake infant neuroimaging at 3 Tesla MRI.* In: Magn Reson Med. 2021;86:1773–1785. DOI: 10.1002/mrm.28791

Impact Factor: 4,668 (2020)
Eigener Anteil: 20%
Design sowie Konstruktion von Behilfsmessinstrumenten und Halterungen zur Datenakquise im Labor, Unterstützung bei der Generierung der Labormessdaten, Interpretation und Diskussion der Ergebnisse, Unterstützung beim Verfassen des Manuskripts

2.3 [3] A 48-Channel Receive Array Coil for Mesoscopic Diffusion-Weighted MRI of Human ex vivo Brain Imaging on the 3T Connectome Scanner

Die Diffusionsgewichtete-MRT (DW-MRT) beruht auf der Bewegung von freien Wassermolekülen durch Diffusion oder der Brown'sche Molekularbewegung. [Ein05, Smo06] Die gewollte Bewegungsempfindlichkeit auf molekularer Ebene der DW-MRT, führt auf globaler Ebene in einem Bereich von Interesse /engl.: *Region of Interest* (ROI) zu Artefakten. Peristaltische, atembedingte, oder kardiale Bewegungen des Probanden führen zur Verschlechterung des Bildes und können es unbrauchbar machen. [Koh07, Bam09, Mal11] Daher müssen Kompromisse eingegangen werden, welche die *in vivo* DW-MRT mit einer Auflösung von 1-3 mm auf den Makrobereich beschränken. [Oka15, Zen18]

Die *ex vivo* Bildgebung bietet hier eine Möglichkeit, lange Aufnahmezeiten von mehreren Tagen ohne Bewegungsartefakte durch den Probanden zu realisieren. Ein Spulensystem kann so gestaltet werden, dass es näher an der Zielregion ist und somit ein höheres SNR erreichen kann. So kann mit der *ex vivo*-DW-MRT eine wesentlich höhere räumliche Auflösung erreicht werden, die es ermöglicht, die Anatomie und Mikrostruktur komplexer Faserbahnen im Mesomaßstab, d. h. im Submillimeterbereich abzubilden. Diese Auflösung geht weit über das hinaus, was *in vivo* möglich ist.

Mit dieser Arbeit wurde die Entwicklung und Konstruktion einer Empfangsspule mit 48 Kanälen für die hochauflösende *ex vivo*-DW-MRT-Gehirnbildgebung auf einem 3T-Connectome-Scanner realisiert. Durch Labormessungen wurde die Funktionsweise validiert als auch die Bildgebungsmetriken an einem Agar-Phantom und einem *ex vivo* menschlichen Gehirn charakterisiert. Das Empfangsspulensystem wurde mit Bedacht auf einen möglichst geringem Abstand zum Gehirn anatomisch angepasst und in zwei trennbare Segmente geteilt. Bildgebende Tests wurden mit einer 64-Kanal-Kopfspule verglichen, welche für den *in vivo*-Einsatz entwickelt wurde. Der SNR-Vergleich zeigte eine 2,9-fache Erhöhung im peripheren Kortex und ein 1,3-fache Erhöhung im Zentrum.

Die 48-kanalige *ex vivo*-Empfangsgehirn verringert auch die Rauschverstärkung bei hochparalleler Bildgebung und ermöglicht Beschleunigungsfaktoren, die bei einem gegebenen Rauschverstärkungspegel um etwa eine Einheit höher liegen.
Die stabile Funktionsfähigkeit der entwickelten Spule wurde demonstriert und ist bereit für hochaufgelöste *ex vivo*-DW-MRT-Studien, die es ermöglichen, die Verbindungen und Mikrostruktur des menschlichen Gehirns auf mehreren Ebenen abzubilden.

Originalarbeit:
Scholz, Alina; Etzel, Robin; **May, Markus W.**; Mahmutovic, Mirsad; Tian, Qiyuan; Ramos-Llorden, Gabriel; Maffei, Chiara; Bilgic, Berkin; Witzel, Thomas; Stockmann, Jason P.; Mekkaoui, Choukri; Wald, Lawrence L.; Yi Huang, Susie; Yendiki, Anastasia; Keil, Boris. *A 48-channel receive array coil for mesoscopic diffusion-weighted MRI of ex vivo human brain on the 3T Connectome scanner.* In: NeuroImage. 2021;231:118256. DOI: 10.1016/j.neuroimage.2021.118256

Impact Factor: 6,556 (2020)
Eigener Anteil: 8%
Methoden-/Projektplanung, Design und Konstruktion von Behilfsmessinstrumenten sowie Halterungen zur Datenakquise im Labor, Design eines Phantoms, Erstellung eines Phantoms, Unterstützung bei der Generierung der Labordaten, Interpretation und Diskussion der Ergebnisse, Unterstützung beim Verfassen des Manuskripts

3 Diskussion

Voraussetzung dieser kumulativen Dissertation war die Anschlussmöglichkeit von 16 Sende- und 64 Empfangselementen an ein 7 T-UHF-MRT. Somit wird die Möglichkeit zur Erstellung von kombinierten komplexen Sende- und Empfangsspulensysteme geschaffen. Primäres Ziel der Forschungsarbeit war die Ausweitung des FOVs von der Gehirn- in die Halsregion, welche in Publikation [1] realisiert und veröffentlicht wurde. Die Entwicklung und Evaluation der Mehrkanal-Sendespulen mit integrierten Mehrkanal-Signaldetektoren bieten eine hohe räumliche Auflösung sowie ein hohes Bild-Kodierungspotential für die beschleunigte UHF-MRT.

Für unterschiedliche Forschungsgebiete sowie klinischen Anwendungsgebiete der UHF-MRT-Bildgebung sollte mit der neu entwickelten Hardware eine patientenfreundliche, sowie durch das geringe Gewicht der Spule, eine für Medizinisch-Technische/r Radiologieassistent/in (MTRA) anwendungsfreundliche Lösung geschaffen werden. Ein für MTRA in klinischer Umgebung handhabbares stabiles Gehäuse wurde realisiert. Bei gleichzeitiger Einhaltung der zulässigen SAR-Grenzwerte und Erhaltung von Bildkontrast und -qualität im Vergleich zu bereits existierenden Spulen konnte hier ein Mehrwert im Bereich der UHF-MRT-Bildgebung erreicht und die Ziele erfüllt werden.

Die Evolution von mehrkanaligen Sendekanälen ähnelt der Entwicklung der mehrkanaligen Empfangsspulen. Zu Beginn der 2000er-Jahre waren MRT-Scanner mit 8 Empfangskanälen ausgestattet. Heute unterstützen die meisten kommerziell verfügbaren 7 T-UHF-MRTs 8 Sendekanäle. Wobei die Verbreitung der Option mit 16 Sendekanälen auch aufgrund der in dieser Arbeit gezeigten Möglichkeiten zunehmen wird.
Im Gegensatz zur damaligen Verbreitung der parallelen Bildgebung durch die Verwendung von mehreren Empfangskanälen und der Optimierung der Hardware, ist eine Verwendung von mehrkanaligen Sendespulen deutlich komplexer, da neue Strukturen simuliert werden müssen. Dies ist notwendig, um bei neuen Strukturen die vorgeschriebenen Grenzwerte einhalten zu können.

In der aktuellen UHF-MRT-Bildgebung werden ab Feldstärken von 7 T verstärkt Dipole als Sendespulen verwendet. [Raa11, vLe22, Ela22, Gil22] In diesem Projekt wurde sich aus mehreren Gründen gegen die Verwendung von Dipolen entschieden. Dipole funktionieren hauptsächlich im elektrischen Fernfeld, wohingegen die verwendeten Leiterschleifenelemente (Loop-Elements) im reaktiven Nahfeld arbeiten. Dipole erzeugen daher in tieferliegenden Geweben ein besseres B_1^+-Feld, wohingegen Loop-Elemente Vorteile im Nahbereich haben. Im Nahbereich erzeugen Dipole aufgrund des höheren elektrischen Feldes einen höheren SAR Wert.

Da SAR ein limitierender Faktor in der UHF-MRT-Bildgebung ist, wurde aufgrund dieser Eigenschaften die Realisierung mit Loop Elementen angestrebt. Ein weiterer Vorteile der Loop-Elemente sind die guten Entkopplungsmethoden wie beispielsweise durch die RID-Entkopplungsstruktur, wohingegen Dipole hauptsächlich durch den geometrischen Abstand voneinander entkoppelt werden. [Raa16]

Eine Besonderheit dieser Arbeit liegt in der methodischen iterativen Umsetzung. So wurde nach einer Phase, in der das Sendekonzept und die Sendespulenverteilung festgelegt wurden, diese in einem CAD-Modell konstruiert. Dieses Design wurde für die Simulation verwendet. In der Publikation [1] wurde großer Aufwand betreiben, um die Simulation unter Berücksichtigung verschiedener Einflussfaktoren (z.B. Herstellertoleranzen, Temperatur, Positionierung des Phantoms) möglichst realistisch zu gestalten. Hierzu wurde das RID-Netzwerk in die Simulation mit einbezogen, was die Komplexität deutlich steigert. So wurden beispielsweise in der Simulation 114 Variablen verwendet, die sich alle gegenseitig beeinflussen. Die Besonderheit dieser Arbeit besteht in der manuellen Umsetzung dieser komplexen Simulation unter Berücksichtigung der derzeitigen Rechenleistung.

Bei dem Vergleich von Simulation mit der konstruierten Spule wies die konstruierte Spule insgesamt bessere Entkopplungswerte zwischen den Elementen auf, wobei es in einigen Fällen zu größeren Diskrepanzen kam. Diese Diskrepanz kann die Genauigkeit der Sicherheitsbewertung der Spule beeinträchtigen. Der Vergleich der simulierten und gemessenen B_1^+-Felder wurde eine akzeptable Diskrepanz von ±20% gezeigt. In Verbindung mit einem Sicherheitsfaktor wurden Sicherheitsbedenken in Bezug auf ein potenziell unvorhersehbares Feldverhalten der Spule entkräftet.

Im Rahmen der interdisziplinären wissenschaftlichen Arbeitsweise konnten die Methoden und kleinere Messvorrichtungen der UHF-MRT auf andere Projekte übertragen werden und diese unterstützen. Hier kann beispielsweise eine Testvorrichtung erwähnt werden, die im Rahmen der UHF-MRT die Vorverstärker ein- und ausschaltet und somit die Empfangselemente aktiviert oder diese deaktiviert.
Diese Messvorrichtung wurde mit Modifikationen wie beispielsweise einem anderen Steckersystem für 3 T-Spulen versehen und konnte bei Publikation [2] und Publikation [3] verwendet werden. Im Gegensatz zu Publikation [1] war jedoch keine Testmessvorrichtung notwendig, welche Sendeelemente unterstützt, da das Birdcage-Sendesystem bei 3 T-MRTs im Scanner fest verbaut ist. Alle drei spezifischen Publikationen eint die initiale Evaluations- und Optimierungsphase unter Messbedingungen, bevor eine erste Messung am Scanner durchgeführt werden kann.

Bei Publikation [1] resultierte der iterative Optimierungsprozess in einer kompletten Neukonstruktion. Die Kopplung und Beeinflussung der Kabelführung zusammen mit der generellen Kopplung aller 64-Empfangselemente mit den darüber liegenden 16-Sendeelementen gestaltete sich aufgrund der hohen Dichte an Leiterschleifen und dem trennbaren Gehäusedesign als sehr herausfordernd. Eine konstruktionsbedingte

Kopplung konnte nicht an allen Stellen ausgeschlossen werden. Besonders bei großen Empfangselementen wurde eine zusätzliche passive Entkopplungsstruktur in der Leiterschleife notwendig, um eine Kopplung mit dem darüber liegenden Sendeelement zu minimieren.

Bei einer Q-Faktor-Messung der Sendeelemente zeigte sich der Vorteil von kleineren Sendeelementen, da bei den größeren ein Faktor von fast 2,2 gemessen wurde. Dies deutet darauf hin, dass dieses Element fast eine Rauschdominanz aufweist. Von Rauschdominanz wird ab einem Faktor von < 2 gesprochen. Diese Erkenntnisse könnte man in einer Simulation oder in einer tatsächlichen Konstruktion messen.
Der tatsächliche Konstruktionsprozess und Bauprozess ist deutlich schneller als der Simulationsprozess, wodurch insgesamt 4 Spulensysteme gestaltet und hergestellt wurden. Diese Geschwindigkeit geht jedoch zulasten eines bereits zuvor auf Seite **??** erwähnten höheren Kostenfaktors. Aufgrund der Kostenintensitivität beschäftigen sich mehr Forschungsgruppen mit der Software- als Hardwareoptimierung in der MRT. Im Rahmen der iterativen Optimierung wurden hier Zwischenergebnisse auf einem Kongress publiziert. [May19]

In der Evaluationsphase zeigte der Vergleich mit einer kommerziell verfügbaren 32-Kanal-Gehirnspule, eine leichte Verbesserung sowohl beim SNR als auch in der Beschleunigung im parallelen Bildgebungsprozess. Wie erwartet, lag der größte Vorteil in der erweiterten Abdeckung des Halsbereichs im Vergleich zum reinen Hirnspulendesign. Die in Publikation [1] verwendete Spule besitzt insgesamt 64 Kanäle wobei 42-Kanäle das Hirn abdecken und zu einer höheren Spulendichte in dem Bereich führte, die zusätzlichen Empfangsspulen wurden im Halsbereich angebracht. Die kommerzielle Spule ist für deutlich kleinere Kopfdurchmesser konstruiert worden. Der kleinere Radius hat zur Folge, dass weniger Probanden und Patienten in das Spulensystem passen als die hier geschaffene Lösung. Zudem sind die Empfangselemente näher am Probanden, woraus potentiell ein besseres SNR resultieren könnte. Die Kopf-Halsspule zeigt jedoch in der Gehirnregion ein um den Faktor 1.5 höheres und im Gehirnstamm um den Faktor 3,4 höheres SNR. (vgl. Publikation [1] in Abb. 7)

Das erste große in-vivo Bild zeigt die Machbarkeit der kombinierten Gehirn- als auch Halswirbelsäulenbildgebung mit einer Messung bei $7\,\mathrm{T}$ unter Verwendung von B_1^+ Shimming mit 16-Sendekanälen und der parallelen Bildgebung mit 64-Empfangselementen. (vgl. Publikation [1] in Abb. 10)

Aktuelle Forschung

Das Ergebnis stellt einen hohen wissenschaftlichen Erkenntniswert dar und bietet Lösungsansätze für Probleme in der UHF-MRT, die über längere Zeit ungelöst waren. Diese Arbeit bietet die Basis für Forschungsprojekte vor allem im Bereich der Neurologie, die in Zeitschriften mit höherem Impact-Factor publiziert werden können z.B.[All22].
Als Beispiel kann hier auch die aktuelle COVID-19 Forschung genannt werden. Bei

Patienten, die unter dem Sammelbegriff Long-COVID leiden, wurde unter anderem eine dysfunktionale Hirnstamm-/Vagusnerven-Signalübertragung diagnostiziert, [Pro21] die eine Ursache für Long-COVID sein könnte, deren Untersuchung bereits gefordert wurde [Aza21] und mit diesem Projekt ermöglicht wird. Mit der im Rahmen dieses Projekts erstellten Hardware wird derzeit auch unter anderem der Vagusnerv näher untersucht, um Ursachen und Behandlungsmethoden für Long-COVID zu finden.

Ausblick

Die besonderen nichtmagnetischen Anforderungen in Bezug auf Komponenten sind ein Grund für die hohen Kosten einer kommerziell verfügbaren UHF-MRT-Spule, die sich im 6-stelligen Bereich abspielen. Aus wirtschaftlicher Sicht herrscht folglich großes Interesse an der Vervielfältigung dieser Arbeit, da die Entwicklungskosten mit der Herstellung eines funktionsfähigen Prototyps hiermit geleistet wurden.
Aufgrund der hohen Entwicklungskosten, in Kombination mit überschaubaren Stückzahlen für einen kleinen Absatzmarkt, wurde dieses Risiko für dieses Projekt nicht in der freien Wirtschaft realisiert. Dieses Projekt zeigt eine Möglichkeit einer Realisierung, worauf mögliche Firmen aufbauen können und weswegen in naher Zukunft auch kommerzielle kombinierte Kopf- und Halsspulen bei 7 T-verfügbar sein werden.

Bei einer möglichen kommerziellen Umsetzung könnte hier auch das Gehäuse optimiert werden. Der initiale Gedanke der Befestigungsstäbe, die an der Seite der Spule angebracht wurden, war die RID-Netzwerke mit einer möglichst geringen Toleranz von 0,1 mm übereinander platzieren zu müssen, um die benötigte Entkopplung von oberen und unteren Sendeelementen realisieren zu können.
Diese Annahme zeigte sich jedoch im Konstruktionsprozess als Fehleinschätzung. Die Entkopplungsstrukturen benötigen jedoch keine solche exakte Platzierung zueinander, was den Grund für die Existenz der durchaus klobigen Befestigungsstäbe an der Spulenausenseite eliminiert. Bei einer Neukonstruktion kann die Fixierung von den beiden Spulengehäusen zueinander durchaus graziler gestaltet und somit für den Patienten anschaulicher gestaltet werden.

Bei speziellen Interessensregionen wie beispielsweise dem Vagusnerv oder dem Hirnstamm kann die entwickelte Hardware noch weiter verbessert werden. Zudem besteht noch Ausblick auf weitere Optimierung der Bildgenerierung. Hier ist vor allem die Anwendung von angepassten Pulsen unter Verwendung von pTx zu nennen. Diese Methode wird dynamisches pTx genannt.
Dynamisches pTx wurde in dieser Arbeit nicht durchgeführt, da das statische pTx zum Beweis der FOV-Erweiterung ausreicht. Hier könnte eine weitere Doktorarbeit ansetzen. Leitão et al. zeigte kürzlich eine neue Möglichkeit zur Homogenisierung des B_1^+-Felds durch pTx. [Lei22] Zudem bietet die Anwendung von dynamischen pTx auf diesem Spulensystem die Möglichkeit der SAR-reduktion, welcher ein limitierender Faktor bei der klinischen Bildgebung ist.

Die Elektroenzephalografie (EEG) spielt in der Kombination mit der UHF-MRT eine bedeutende Rolle bei der aktuellen Erforschung von Epilepsie. [Sal21] Um das Potenzial ein EEG für zukünftige Untersuchungen und Auswirkungen für die Kopf- und Halsregion zu ermöglichen, wurde im Designprozess dieser Spule ein Kabelloch gelassen. Hier können spätere EEG-Kabel durchgeführt werden, um EEG-Untersuchungen zu ermöglichen.

Die fMRT ist von großem Interesse der allgemeinen wissenschaftlichen aktuellen Forschung und 7 T-Datensätze der Gehirnregion alleine werden in hochrangig publiziert. [All22] Mit dieser Arbeit wird die Grundlage für die Ausweitung in den Halsbereich geschaffen. Menschheitsfragen wie diese können vielleicht in Zukunft damit beantwortet werden:

- Wie genau und wie schnell breiten sich Läsionen von MS in Hirn und Wirbelsäule aus?
- Wie genau funktioniert die Signalübertragung zwischen Hirn und Wirbelsäule?
- Wie verändert eine Verletzung die Kommunikation zwischen Hirn und Wirbelsäule?

Zusammenfassend kann festgehalten werden, dass von einer Erweiterung des FOVs die klinische UHF-MRT profitiert und somit ein Mehrwert für die Menschheit geschaffen wurde. Der Mehrwert liegt besonders in der Möglichkeit, eine frühere Diagnose wie bei MS stellen zu können. Unter anderem kann die Diagnose von MS durch *Deep Learning* (DL) gestützte Algorithmen noch weiter verbessert werden, da dies ein aktuelles Thema der Forschung ist. [Ros22]

Aktuelle Publikationen können die Scangeschwindigkeit mittels DL-Algorithmus so verkürzen, ohne die Bildqualität bemerkbar zu beeinträchtigen. Hier sind die Gewinner der "fastMRI Challenge 2019" [Pez20, Che22] zu erwähnen. *Artificial Intelligence* (AI) oder DL bietet die Möglichkeit zur weiteren UHF-MRT-Bildverbesserung, im Speziellen die Kontrastverbesserung sowie Rauschunterdrückung. DL-Algorithmen benötigen jedoch zu Beginn sehr große Trainingsdatensätze. Derzeit werden über 10.000 Datensätze bei aktuellen 3 T Publikationen verwendet, die zunächst manuell einzeln ausgewertet werden müssen, um sie zu klassifizieren. [Gau21] Datensätze die an unterschiedlichen Scannern aufgenommen wurden, unterscheiden sich jedoch und müssen zunächst homogenisiert werden. [Cla20, Li 20] Es wurde aber auch gezeigt, dass selbst in Studien, die Lerndatensätze aus verschiedenen Standorten verwendet hatten, mit einheitlicher Scanner-Feldstärke und nach einer Protokollharmonisierung systematische Unterschiede zu erheblichen Verzerrungen der Ergebnisse führen können. [SZ15]

Die höher aufgelösten 7 T Datensätze bieten jedoch das Potential einen Lerndatensatz aufzubauen, um beispielsweise Datensätze, die mit niedriger Magnetfeldstärke aufgenommen wurden (z.B. 3 T), in einer Auflösung darstellen zu lassen, als wären sie bei 7 T aufgenommen worden. In der Praxis könnte dieser Ansatz mit über 10.000 Datenaufnahmen herausfordernd werden, da diese diagnostiziert und doppelt (bei niedrigem und hohem B_0-Feld z.B. 1,5 T und 7 T) aufgenommen werden müssen und zudem scannerabhängig sind.

Literaturverzeichnis

[All22] E. Allen et al. „A Massive 7T fMRI Dataset to Bridge Cognitive Neuroscience and Artificial Intelligence”. *Nature Neuroscience*, 25(1):S.116–126, 2022.

[Als98] D. Alsop et al. „A Spiral Volume Coil for Improved RF Field Homogeneity at High Static Magnetic Field Strength”. *Magn. Res. in Med.*, 40(1):S.49–54, 1998.

[Aus14] A. Aussenhofer et al. „An Eight-Channel Transmit/Receive Array of TE01 Mode High Permittivity Ceramic Resonators for Human Imaging at 7T”. *Journal of Magnetic Resonance*, 243:S.122–129, 2014.

[Aza21] E. Azabou et al. „Vagus Nerve Stimulation: A Potential Adjunct Therapy for COVID-19”. *Frontiers in Medicine*, V.8, 2021.

[Bam09] R. Bammer et al. „New Methods in Diffusion-Weighted and Diffusion Tensor Imaging”. *Magn. Res. in Imag. Clinics of NA*, 17(2):S.175–204, 2009.

[Bar90] H. Barfuss et al. „In Vivo Magnetic Resonance Imaging and Spectroscopy of Humans with a 4 t Whole-Body Magnet”. *NMR in Biomedicine*, 3(1):S.31–45, 1990.

[Bur21] B. Burkett et al. „Clinical 7-T MRI for Neuroradiology: Strengths, Weaknesses, and Ongoing Challenges”. *Neuroradiology*, 63(2):S.167–177, 2021.

[Che22] E. Chen et al. „Pyramid Convolutional RNN for MRI Image Reconstruction”. *IEEE transactions on medical imaging*, PP, 2022.

[Cla20] W. Clarke et al. „Multi-Site Harmonization of 7 Tesla MRI Neuroimaging Protocols”. *NeuroImage*, 206:S.1165, 2020.

[Cle19] J. Clement et al. „A Combined 32-channel Receive-loops/8-channel Transmit-dipoles Coil Array for Whole-brain MR Imaging at 7T”. *Magn. Res. in Med.*, 82(3):S.1229–1241, 2019.

[Coh11] J. Cohen-Adad et al. „32-Channel RF Coil Optimized for Brain and Cervical Spinal Cord at 3T”. *Magn. Res. in Med.*, 66(4):S.1198–1208, 2011.

[Col11] C. Collins et al. „Calculation of Radiofrequency Electromagnetic Fields and Their Effects in MRI of Human Subjects”. *Magn. Res. in Med.*, 65(5):S.1470–1482, 2011.

[Com15] I.E. Commission et al. IEC 60601-2-33: Ed. 3.2- Medical Electrical Equipment Part 2-33: Particular Requirements for the Basic Safety and Essential Performance of Magnetic Resonance Equipment for Medical Diagnosis, 2015.

[Cur12] A. Curtis et al. „Slice-by-Slice B1+ Shimming at 7 T”. *Magn. Res. in Med.*, 68(4):S.1109–1116, 2012.

[Dam14] E. Damaraju et al. „Functional Connectivity in the Developing Brain: A Longitudinal Study from 4 to 9months of Age". *NeuroImage*, 84:S.169–180, 2014.

[Din11] I. Dinstein et al. „Disrupted Neural Synchronization in Toddlers with Autism". *Neuron*, 70(6):S.1218–1225, 2011.

[Eig21] T. Eigentler et al. „32-Channel Self-Grounded Bow-Tie Transceiver Array for Cardiac MR at 7Tesla". *Magnetic Resonance in Medicine*, 86(5):S. 2862–2879, 2021.

[Ein05] A. Einstein. „Über Die von Der Molekularkinetischen Theorie der Wärme Geforderte Bewegung von in Ruhenden Flüssigkeiten Suspendierten Teilchen". *Annalen der Physik*, 322(8):S.549–560, 1905.

[Ela22] I. Elabyad et al. „A Novel Antisymmetric 16-Element Transceiver Dipole Antenna Array for Parallel Transmit Cardiac MRI in Pigs at 7 T". *NMR in Biomedicine*, page S.4726, 2022.

[Fei10] D. Feinberg et al. „Multiplexed Echo Planar Imaging for Sub-Second Whole Brain FMRI and Fast Diffusion Imaging". *PLOS ONE*, 5(12):S.15710, 2010.

[Fel19] R. Feldman et al. „7T MRI in Epilepsy Patients with Previously Normal Clinical MRI Exams Compared against Healthy Controls". *PloS One*, 14(3):S.0213642, 2019.

[Gao20] Y. Gao et al. „A 16-Channel AC/DC Array Coil for Anesthetized Monkey Whole-Brain Imaging at 7T". *NeuroImage*, 207:S.116396, 2020.

[Gau21] R. Gauriau et al. „A Deep Learning-based Model for Detecting Abnormalities on Brain MR Images for Triaging". *Radiology. Artificial Intelligence*, 3(4):S.200184, 2021.

[Gil11] K. Gilbert et al. „A Radiofrequency Coil to Facilitate B_1^+ Shimming and Parallel Imaging Acceleration in Three Dimensions at 7 T". *NMR in biomedicine*, 24(7):S.815–823, 2011.

[Gil22] K. Gilbert et al. „Integration of an RF Coil and Commercial Field Camera for Ultrahigh-Field MRI". *Magn. Res. in Med.*, 87(5):S.2551–2565, 2022.

[Gol17] L. Golestanirad et al. „Feasibility of Using Linearly Polarized Rotating Birdcage Transmitters and Close-Fitting Receive Arrays in MRI to Reduce SAR in the Vicinity of Deep Brain Simulation Implants". *Magn. Res. in Med.*, 77(4):S.1701–1712, 2017.

[Gri02] M. Griswold et al. „Generalized Autocalibrating Partially Parallel Acquisitions GRAPPA". *Magn. Res. in Med.*, 47(6):S.1202–1210, 2002.

[Gru21] B. Gruber et al. „A 128-Channel head coil array for Cortical Imaging at 7 Tesla". In *27th Annual Meeting of ISMRM*, page S.0176, Virtual Meeting (Covid-19), 2021.

[Hou76] D. Hoult et al. „The Signal-to-Noise Ratio of the Nuclear Magnetic Resonance Experiment”. *Journal of MR*, 24(1):S.71–85, 1976.

[Hou00a] D. I. Hoult. „The Principle of Reciprocity in Signal Strength Calculations-A”. *Concepts in MR*, 12(4):S.173–187, 2000.

[Hou00b] D. Hoult et al. „Sensitivity and Power Deposition in a High-Field Imaging Experiment”. *J. of Magn. Res. in Med.*, 12(1):S.46–67, 2000.

[Hug17] E. Hughes et al. „A Dedicated Neonatal Brain Imaging System”. *Magn. Res. in Med.*, 78(2):S.794–804, 2017.

[Ibr00] T. Ibrahim et al. „Application of Finite Difference Time Domain Method for the Design of Birdcage RF Head Coils Using Multi-Port Excitations”. *Magn. Res. in Med.*, 18(6):S.733–742, 2000.

[Jar15] T. Jaretz et al. *„Wissen, gerechtfertigte Meinung und Nichtwissen: Das Menon- und Gettierproblem im Kontext”*. Diplomica Verlag, 2015.

[Jez22] P. Jezzard. „Magnetic Resonance in Medicine, General Journal Information”. *Wiley Online Library*, 01.04.2022.

[Kat06] U. Katscher et al. „Parallel RF Transmission in MRI”. *NMR in Biomedicine*, 19(3):S.393–400, 2006.

[Kei11] B. Keil et al. „Size-Optimized 32-Channel Brain Arrays for 3 T Pediatric Imaging”. *Magn. Res. in Med.*, 66(6):S.1777–1787, 2011.

[Kei13a] B. Keil et al. „A 64-Channel 3T Array Coil for Accelerated Brain MRI”. *Magn. Res. in Med.*, 70(1):S.248–258, 2013.

[Kei13b] B. Keil et al. „Massively Parallel MRI Detector Arrays”. *Journal of MR*, 229:S.75–89, 2013.

[Koh07] D. Koh et al. „Practical Aspects of Assessing Tumors Using Clinical Diffusion-Weighted Imaging in the Body”. *MRMS: an official journal of Japan Society of Magnetic Resonance in Medicine*, 6(4):S.211–224, 2007.

[Kon02] Y. Konishi et al. „Functional Brain Imaging Using fMRI and Optical Topography in Infancy”. *Sleep Medicine*, 3:S.41–S43, 2002.

[Kwo92] K. Kwong et al. „Dynamic Magnetic Resonance Imaging of Human Brain Activity during Primary Sensory Stimulation”. *Proceedings of the National Academy of Sciences*, 89(12):S.5675–5679, 1992.

[Lak20] K. Lakshmanan et al. „The Loopole Antenna”. *Concepts in magnetic resonance. Part B, Magnetic resonance engineering*, 2020:S.8886543, 2020.

[Lat09] R. Lattanzi et al. „Electrodynamic Constraints on Homogeneity and Radiofrequency Power Deposition in Multiple Coil Excitations”. *Magn. Res. in Med.*, 61(2):S.315–334, 2009.

[Lau73] P. Lauterbur. „Image Formation by Induced Local Interactions: Examples Employing Nuclear Magnetic Resonance”. *Nature*, 242(5394):S.190–191, 1973.

[Led06] P. Ledden et al. „Twenty-Four Channel Receive-Only Array for Brain Imaging at 7T". *Proc. Intl. Soc. Mag. Reson.*, page S.422, 2006.

[Lei22] D. Leitao et al. „parallel transmit pulse design for saturation homogeneity push for magnetization transfer imaging at 7t". *Magn. Res. in Med.*, 2022.

[Li 20] H. Li et al. „Denoising Scanner Effects from Multimodal MRI Data Using Linked Independent Component Analysis". *NeuroImage*, 208:S.116388, 2020.

[Mal11] A. Malayeri et al. „Principles and Applications of DWI in Cancer Detection, Staging, and Treatment Follow-up". *RadioGraphics*, 31(6):S.1773–1791, 2011.

[Man77] P. Mansfield et al. „Medical Imaging by NMR". *The British Journal of Radiology*, 50(591):S.188–194, 1977.

[Mao06] W. Mao et al. „Exploring the Limits of RF Shimming for High-Field MRI of the Human Head". *Magn. Res. in Med.*, 56(4):S.918–922, 2006.

[Mar12] F. Martino et al. „Spin Echo Functional MRI in Bilateral Auditory Cortices at 7 T: An Application of B_1 Shimming". *NeuroImage*, 63(3):S.1313–1320, 2012.

[May19] M. May et al. „Design Considerations of a 64-Channel Receive / 16-Channel Transmit Coil Array for Head, Neck, and Cervical-Spine Imaging at 7 T". In *27th Annual Meeting of ISMRM*, page S.1519, Montréal, QC, Canada, 2019.

[McR06] Donald W McRobbie. *MRI from Picture to Proton*. Cambridge University Press, Cambridge, UK; New York, 2006.

[Mei22] C. Meixner et al. „Hybrid B1+ -Shimming and Gradient Adaptions for Improved Pseudo-Continuous Arterial Spin Labeling at 7 Tesla". *Magn. Res. in Med.*, 87(1):S.207–219, 2022.

[Moh04] Aleš. Mohorič et al. „Magnetic Resonance Imaging System Based on Earth's Magnetic Field". *Instrumentation Science and Technology*, 32(6):S. 655–667, 2004.

[Moo05] PF. Moortele et al. „B(1) Destructive Interferences and Spatial Phase Patterns at 7 T with a Head Transceiver Array Coil". *Magn. Res. in Med.*, 54(6):S.1503–1518, 2005.

[Nob03] Nobel Assembly at Karolinska Institutet (03.2022). „The Nobel Prize in Physiology or Medicine 2003". https://www.nobelprize.org/prizes/medicine/2003/press-release/, 2003.

[Oga90] S. Ogawa et al. „Brain Magnetic Resonance Imaging with Contrast Dependent on Blood Oxygenation". *Proceedings of the National Academy of Sciences*, 87(24):S.9868–9872, 1990.

[Oka15] H. Okano et al. „Brain-Mapping Projects Using the Common Marmoset". *Neuroscience Research*, 93:S.3–7, 2015.

[Pad16] F. Padormo et al. „Parallel Transmission for Ultrahigh-field Imaging". *Nmr in Biomedicine*, 29(9):S.1145–1161, 2016.

[Pez20] N. Pezzotti et al. „An Adaptive Intelligence Algorithm for Undersampled Knee MRI Reconstruction“. *IEEE Access*, 8:S.204825–204838, 2020.

[Pod84] S. Poduslo et al. „Myelin Development in Infant Brain“. *Neurochemical Research*, 9(11):S.1615–1626, 1984.

[Poh16] R. Pohmann et al. „SNR and MR Tissue Parameters in Human Brain Imaging at 3, 7, and 9.4 Tesla Using Current Receive Coil Arrays“. *Magn. Res. in Med.*, 75(2):S.801–809, 2016.

[Pro21] A. Proal et al. „Long COVID or Post-acute Sequelae of COVID-19 (PASC): An Overview of Biological Factors That May Contribute to Persistent Symptoms“. *Frontiers in Microbiology*, 12:S.698169, 2021.

[Pru99] K. Pruessmann et al. „SENSE: Sensitivity Encoding for Fast MRI“. *Magn. Res. in Med.*, 42(5):S.952–962, 1999.

[Raa11] A. Raaijmakers et al. „Design of a Radiative Surface Coil Array Element at 7T“. *Magn. Res. in Med.*, 66(5):S.1488–1497, 2011.

[Raa16] A. Raaijmakers et al. „Dipole Antennas for Ultrahigh-Field Body Imaging: A Comparison with Loop Coils“. *NMR in Biomedicine*, 29(9):S.1122–1130, 2016.

[Rob08] P. Robson et al. „Comprehensive Quantification of Signal-to-Noise Ratio and g-Factor for Image-Based and k-Space-Based Parallel Imaging Reconstructions“. *Magn. Res. in Med.*, 60(4):S.895–907, 2008.

[Roe90] P. Roemer et al. „The NMR Phased Array“. *Magn. Res. in Med.*, 16(2):S.192–225, 1990.

[Ros22] F. Rosa et al. „Multiple Sclerosis Cortical Lesion Detection with Deep Learning at Ultra-High-Field MRI“. *NMR in biomedicine*, page S.4730, 2022.

[Run22] VM. Runge et al. „The Clinical Utility of MRI According to Field Strength, Specifically Addressing the Breadth of Current State-of-the-Art Systems, Which Include 0.55 T, 1.5 T, 3 T, and 7 T“. *Investigative Radiology*, 57(1):S.1–12, 2022.

[RW00] T. W. Redpath and C. J. Wiggins. Estimating achievable signal-to-noise ratios of MRI transmit-receive coils from radiofrequency power measurements: Applications in quality control. *Physics in Medicine and Biology*, 45(1):S.217–227, 2000.

[Sal21] F. Salehi et al. „Ultra-High Field 7-Tesla Magnetic Resonance Imaging and Electroencephalography Findings in Epilepsy“. *Journal l'Association Canadienne Des Radiologistes*, page S.846, 2021.

[Sch14] S. Schmitter et al. „Cerebral TOF Angiography at 7T: Impact of B1+Shimming with a 16-Ch Tx Array“. *Magn. Res. in Med.*, 71(3):S.966–977, 2014.

[Set09] K. Setsompop et al. „Broadband Slab Selection with B1+ Mitigation at 7T via Parallel Spectral-Spatial Excitation“. *Magn. Res. in Med.*, 61(2):S.493–500, 2009.

[Set12] K. Setsompop et al. „Blipped-Controlled Aliasing in Parallel Imaging for Simultaneous Multislice Echo Planar Imaging with Reduced g-Factor Penalty”. *Magn. Res. in Med.*, 67(5):S.1210–1224, 2012.

[Sha14] G. Shajan et al. „A 16-Channel Dual-Row Transmit Array in Combination with a 31-Element Receive Array for Human Brain Imaging at 9.4 T”. *Magn. Res. in Med.*, 71(2):S.870–879, 2014.

[Sha21] H. Sharma et al. „Utility of 7 Tesla MRI Brain in 16 ‘MRI Negative‘ Epilepsy Patients and Their Surgical Outcomes”. *Epilepsy & Behavior Reports*, 15:S.424, 2021.

[Smo06] M. Smoluchowski. „Zur Kinetischen Theorie Der Brownschen Molekularbewegung Und Der Suspensionen”. *Annalen der Physik*, 326(14):S.756–780, 1906.

[SZ15] Karen Simonyan and Andrew Zisserman. Very Deep Convolutional Networks for Large-Scale Image Recognition. *arXiv:1409.1556 [cs]*, 2015.

[Tra18] S. Trattnig et al. „Key Clinical Benefits of Neuroimaging at 7T”. *NeuroImage*, 168:S.477–489, 2018.

[Tre19] C. Treaba et al. „Longitudinal Characterization of Cortical Lesion Development and Evolution in Multiple Sclerosis with 7.0-T MRI”. *Radiology*, 291(3):S.740–749, 2019.

[Tre21] C. Treaba et al. „Cortical and Phase Rim Lesions on 7 T MRI as Markers of MS Disease Progression”. *Brain Communications*, 3(3):S.134, 2021.

[Val06] P. Valsasina et al. „Diffusion Tensor MRI of the Spinal Cord in Amyotrophic Lateral Sclerosis”. *European Journal of Neurology*, 13, 2006.

[Var18] M. Vargas et al. „Clinical Neuroimaging Using 7T MRI”. *Journal of Neuroimaging*, 28(1):S.5–13, 2018.

[vLe22] C. vLeeuwen et al. „The Coax Dipole: A Fully Flexible Coaxial Cable Dipole Antenna with Flattened Current Distribution for Body Imaging at 7Tesla”. *Magn. Res. in Med.*, 87(1):S.528–540, 2022.

[Yan06] Q. Yang et al. „Manipulation of Image Intensity Distribution at 7.0 T”. *J. of Magn. Res. in Imag.*, 24(1):S.197–202, 2006.

[Zen18] Hongkui Zeng. Mesoscale connectomics. *Current Opinion in Neurobiology*, 50:S.154–162, 2018.

[Zha14] W. Zhao et al. „19ch Rx Array and 4ch Tx Array Coil for Cervical Spinal Cord Imaging at 7T”. *Magn. Res. in Med.*, 72(1):S.291–300, 2014.

[Zha17] B. Zhang et al. „7T 22-Channel Wrap-around Coil Array for Cervical Spinal Cord and Brainstem Imaging”. *Magn. Res. in Med.*, 78(4):S.1623–1634, 2017.

[Zhu04] Yudong Zhu. Parallel excitation with an array of transmit coils. *Magn. Res. in Med.*, 51(4):S.775–784, 2004.

Received: 8 November 2021 | Revised: 12 April 2022 | Accepted: 13 April 2022

DOI: 10.1002/mrm.29288

RESEARCH ARTICLE

Magnetic Resonance in Medicine

A patient-friendly 16-channel transmit/64-channel receive coil array for combined head–neck MRI at 7 Tesla

Markus W. May[1] | Sam-Luca J. D. Hansen[1] | Mirsad Mahmutovic[1] | Alina Scholz[1] | Nicolas Kutscha[1] | Bastien Guerin[2,3] | Jason P. Stockmann[2,3] | Robert L. Barry[2,3] | Ehsan Kazemivalipour[2,3] | Rene Gumbrecht[4] | Ralph Kimmlingen[4] | Markus Adriany[4] | Yulin Chang[5] | Christina Triantafyllou[4] | Susanne Knake[6,7] | Lawrence L. Wald[2,3,8] | Boris Keil[1,7]

[1]Institute of Medical Physics and Radiation Protection, Department of Life Science Engineering, Mittelhessen University of Applied Sciences, Giessen, Germany

[2]Athinoula A. Martinos Center for Biomedical Imaging, Department of Radiology, Massachusetts General Hospital, Charlestown, Massachusetts, USA

[3]Harvard Medical School, Boston, Massachusetts, USA

[4]Siemens Healthcare GmbH, Erlangen, Germany

[5]Siemens Medical Solutions USA, Inc., Malvern, Pennsylvania, USA

[6]Department of Neurology, Philipps-Universität Marburg, Marburg, Germany

[7]Center for Mind, Brain and Behavior (CMBB), Philipps-University Marburg, Marburg, Germany

[8]Division of Health Sciences and Technology, Harvard - Massachusetts Institute of Technology, Cambridge, Massachusetts, USA

Correspondence
Markus W. May, Institute of Medical Physics and Radiation Protection, Mittelhessen University of Applied Sciences, Giessen, 35390, Germany
Email: markus.may@lse.thm.de

Purpose: To extend the coverage of brain coil arrays to the neck and cervical–spine region to enable combined head and neck imaging at 7 Tesla (T) ultra-high field MRI.

Methods: The coil array structures of a 64-channel receive coil and a 16-channel transmit coil were merged into one anatomically shaped close-fitting housing. Transmit characteristics were evaluated in a $B_1{}^+$-field mapping study and an electromagnetic model. Receive SNR and the encoding capability for accelerated imaging were evaluated and compared with a commercially available 7 T brain array coil. The performance of the head–neck array coil was demonstrated in human volunteers using high-resolution accelerated imaging.

Results: In the brain, the SNR matches the commercially available 32-channel brain array and showed improvements in accelerated imaging capabilities. More importantly, the constructed coil array improved the SNR in the face area, neck area, and cervical spine by a factor of 1.5, 3.4, and 5.2, respectively, in regions not covered by 32-channel brain arrays at 7 T. The interelement coupling of the 16-channel transmit coil ranged from −14 to −44 dB (mean = −19 dB, adjacent elements <−18 dB). The parallel 16-channel transmit coil greatly facilitates $B_1{}^+$ field shaping required for large FOV neuroimaging at 7 T.

Conclusion: This new head–neck array coil is the first demonstration of a device of this nature used for combined full-brain, head–neck, and cervical-spine imaging at 7 T. The array coil is well suited to provide large FOV images, which potentially improves ultrahigh field neuroimaging applications for clinical settings.

KEYWORDS

7 Tesla (7T), head and neck, MRI, neuroimaging, array coil, ultrahigh field (UHF)

Funding information This work was supported by the National Institutes of Health (NIH), grants 5R01EB006847, 1P41EB030006, 1S10OD023637; and the Federal Ministry of Education and Research Germany (BMBF), grant IN2016-2-226.

1 | INTRODUCTION

Ultra-high field (UHF) 7-Tesla (T) MRI is rapidly evolving both in technology and in the potential for medical and scientific applications. There is a growing need for clinical 7 T neuroimaging to provide combined head and neck imaging to match the standard of care at 1.5 and 3 T for the assessment of a variety of neurodegenerative diseases.[1,2] The capabilities of combined full-brain, neck, and cervical spinal MRI have proven valuable in obtaining more insights into many neurodegenerative diseases, such as multiple sclerosis[3,4] and amyotrophic lateral sclerosis.[5] However, the ability of this technique to detect subtle pathologic characteristics is severely limited by the contrast-to-noise ratio and the spatial resolution of current clinical systems.[6]

For susceptibility-based contrast in particular, UHF imaging at 7 T affords advantages in SNR and contrast-to-noise ratio, which can then be traded off for increased spatial resolution and higher SNR.[7] This improvement in diagnostic power has been proven valuable, especially in the identification of small lesions that are not noticeable at standard MRI field strengths.[8,9] To address these clinical needs of combined head–neck imaging at 7 T, dedicated RF coils are required that enable transmission and reception for a considerably larger FOV than existing 7 T brain-only coils. Current state-of-the-art 7 T head, neck, and cervical-(C)-spine imaging necessitates a change of coil for imaging either brain and head areas or the neck/C-spine region.

UHF-7 T scanners currently utilize up to 64 receive (Rx) channels. Although originally proposed for increasing SNR,[10] the use of simultaneous reception with multiple coils to speed up the image encoding has proven critical for improving 7 T image quality.[11] Particularly in single-shot fMRI, highly parallel array coil technology and accelerated parallel image encoding offer the possibility of considerable reduction in echo spacing, encoding time, and the related mitigation of image distortions and intensity dropouts associated with macroscopic susceptibility gradients in UHF-fMRI. This need has been met by the introduction of commercial 7 T 24-channel and 32-channel Rx brain array coils,[12,13] and more recently, coil array hardware studies have exploited the benefits and potential of close-fitting 64-channel 7 T brain arrays.[14] Dedicated 7 T coils for C-spine imaging are limited in their commercial availability and have been overall less technologically studied than 7 T brain-only array coils. Most of the proposed 7 T C-spine coils are designed on an anatomically shaped close-fitting coil former to be placed on the posterior side of the neck.[15–17] Recently, a 22-channel C-spine array coil showed improved SNR by fully encircling the neck region.[18] Combining head and neck imaging at 7 T is challenging due to multiple factors, including transmit (Tx) (B_1^+) nonuniformity, main magnetic field (B_0) inhomogeneity, and the complexity in optimizing Tx–Rx RF coil array strategies. In particular, B_1^+ inhomogeneities caused by the decreased RF wavelength at 7 T need to be compensated by integrating parallel Tx (pTx) elements combined with excitation methods, such as B_1^+ shimming,[19] tailored pTx pulses,[20,21] or spoke pTx pulses with combined simultaneous multislice acquisition.[22] When both pTx and high-density Rx arrays are employed for UHF imaging, the Tx–Rx functionality is usually mechanically separated into 2 housing segments, where a close-fitting head former houses the receivers, whereas the Tx structure is housed in a separate sliding tubular former and pulled over the subject's head.[23–26] In addition to adding a step not needed in 3 T scanning, the cylindrical structure has limited Tx efficiency in the neck due to the distance of the elements. Clément et al. merged the mechanically separated coil housings and showed an 8-channel Tx/32-channel Rx brain-only array that was optimized for a highly space-constrained head gradient system at 7 T.[27] The Tx and Rx structure was integrated into an anatomically conformal coil housing.

In this study, we designed, constructed, and validated a 7 T head–neck array coil aimed at mimicking the form factor of a 3 T head–neck array. We implemented an UHF head–neck coil for which the Rx and Tx elements were merged into one anatomically shaped close-fitting housing, without the need of the external cylindrical Tx housing. Similar to 3 T head–neck arrays, the coil housing is splittable to allow an easy entry for the patient. We evaluated the constructed array coil for head–neck and C-spine imaging performance using SNR and geometry-factor (G-factor) maps. For brain imaging, we compared it directly to a commercially available 8-channel Tx/32-channel Rx brain-only array. We demonstrated the coil's capability in highly accelerated anatomical images and evaluated the suitability for simultaneous UHF imaging of the brain and C-spine cord.

2 | METHODS

2.1 | Coil design and construction

The coil was designed on an anatomically shaped former consisting of a large posterior head–neck part and an overlapping anterior head–neck portion (Figure 1A,B). The mechanical implementation of the housing split has been shown[26] at 3 T and was implemented in this project.

The head–neck coil contour is based on the 96 percentiles of the male head circumferences,[28] which allows to accommodate nearly all human subjects. The general dimension of the inner coil former in the superoinferior, anteroposterior, and left–right direction was restricted to 382 cm, 252 mm, and 195 mm, respectively.[29] We used computer-aided design software program (Rhino3D V.6.0, Robert McNeel & Associates, Seattle, WA, USA) to 3D-model both array coil housings.

The housing of the anterior head–neck portion includes 24 Rx and 8 Tx elements, and the larger posterior head–neck section comprises 40 Rx and 8 Tx elements. The larger posterior section is designed so that the subject can lie down into the coil rather than using a helmet design, which must be pulled down over the head. A locking mechanism was incorporated to mate the anterior and posterior head coil segments. The Rx and Tx structures were merged into one housing instead of implementing a commonly used separate tubular housing (Figure 1C). Therefore, the Tx structure also follows the anatomical shape of the head and neck region. Patient comfort was considered by incorporating large mouth and eye cutouts. The latter facilitates visual stimulation for functional MRI studies. Additionally, a hole for cables between the anterior and posterior segments was implemented at the superior coil end to enable combined electroencephalogram studies.

All helmet parts were 3D-printed in polycarbonate plastic (Fortus 450, Stratasys, Eden Prairie). The 3D printed materials were not further treated (e.g., primed or painted). The total weight of the constructed head–neck coil, including its electronics and plugs, amounts to 11.3 kg. The posterior and anterior segments individually weigh 6.2 and 5.1 kg, respectively.

An anthropomorphic head–neck phantom was constructed with PA12 plastic using laser sintering 3D-printing technology. The phantom was filled with agar gel,[30] which mimics the average dielectric properties of human muscle tissue at the Larmor frequency of 297.2 MHz.[31] The conductivity and relative permittivity of the phantom were measured to be $\sigma = 0.75\,\mathrm{S/m}$ and $\varepsilon_r = 58.2$, respectively, using a dielectric measurement kit (DAK, Schmid & Partner Engineering AG, Zurich, Switzerland).

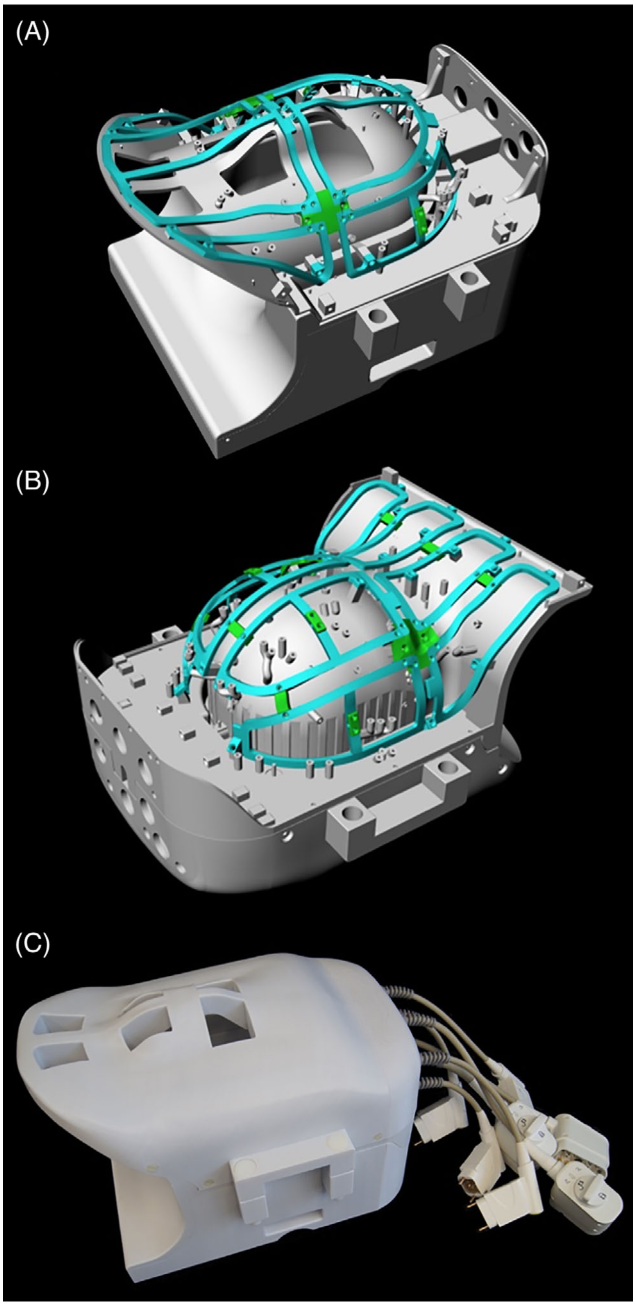

FIGURE 1 CAD model of the constructed 16ch$^{\mathrm{Tx}}$/64ch$^{\mathrm{Rx}}$ head–neck coil. The coil is divided into an anterior and posterior part (A, B). The green highlighted rail structure shows the mounting framing of the anatomically shaped 16-channel Tx array. The assembled head and neck coil (C) features cutouts for the eyes and mouth to facilitate visual stimulation and free breathing, respectively. CAD, computer-aided design; ch, channel; Rx, receive; Tx, transmit.

2.2 | Simulation

A simulation-guided design approach of the 16-channel Tx array was carried out by full-wave electromagnetic analysis using finite element modeling (high-frequency structure simulator (HFSS) Ansys Electronics Desktop 2021 R1, ANSYS Inc., Canonsburg, PA). The simulations were carried out using a high-performance computing server (PowerEdge R740xd, Intel Xeon Gold 6140 CPU 2.30GHz 36 Cores 1.5 TB RAM, Dell

Technologies Inc, Round Rock, TX). Simulation time for the fully tuned, decoupled, and adjusted Tx coil array model was approximately 2 days for the single-compartment head and neck model and 3 days for the multi-tissue HFSS human body model in order to generate all field maps.

The digital version of the head–neck loading phantom was imported into HFSS, and the dielectric parameters were matched to the real values. The Tx structure model included all construction details, including precise dimensions and electrical material properties. All Tx elements were modeled with the 3D computer-aided design software and imported into HFSS. The loop conductor material was defined as copper ($\sigma = 5.8{\cdot}10^7$ S/m) in HFSS. Each channel of the Tx array was excited using a 1 V_{rms} sinusoidal continuous RF wave at the Larmor frequency of 297.2 MHz (7 T) for obtaining the B_1^+ efficiency maps of individual Tx elements. To determine the specific absorption rate (SAR) in the circularly polarized (CP) configuration, an input power of 1 W was applied on the total simulation. In addition, all 16 Tx ports were connected to a 0.07 dB attenuator in the RF co-simulation to account for the cable loss from the coil's feed port to the coil plug.

All discrete RF components (capacitors and inductors) were defined as variable lumped ports in the HFSS computational model in order to allow them to be tuned in the circuit simulator. At the initial step, we simulated each individual loop element to derive the needed capacitors for tuning and matching using an RF co-simulating approach.[32] Decoupling networks between adjacent Tx elements were emulated using a resonant inductive decoupling (RID) circuitry method.[33] The complex excitation profile of each coil was taken as the B_1^+ component of the simulated magnetic field. Because the anatomical conformal 16-channel dual-row Tx coil is not of a purely cylindrical design, we obtained required phases for the CP mode by the actual radially given geometric angular increments of the elements. In addition to the regular CP shim mode, we also evaluated a the CP^{2+} shim configuration (90° phase increments).

The capacitor values of the Tx array were determined in a two-step simulation approach: First, we simulated, tuned, and matched the array to obtain the values of the required capacitors. In the second step, the simulated capacitors values were chosen to match the closest discrete value from the standard capacitor kit. To allow tuning and matching, one variable tuning capacitor and two variable matching capacitors were implemented in each Tx coil element model. Based on the simulated lumped elements values, the Tx coil was then constructed and bench-top-validated (Figure 2).

Due to the geometrical and electrical complexity, the Rx array was not incorporated in the simulation. For realistic SAR simulations, a multi-compartment human dielectric equivalent head–neck model was used (HFSS, ANSYS Inc., Canonsburg, PA).[34]

Local SAR maps (SAR averaged over 10 g of tissue, - IEC/IEEE 62704–4 standard) of the head–neck human model were used to create *Q*-matrices in MatLab (MathWorks, R2019b Natick, MA). The *Q*-matrices were compressed into a set of 2866 virtual observation points[35] with an SAR overestimation factor of 5% of the worst possible local SAR. The virtual observation points were used on the scanner to calculate the maximum local SAR for any complex excitation. A 2.5-fold safety factor was added to the local SAR matrices to account for subject anatomic variability, coil modeling inaccuracies, uncertainties in the MRI scanner RF monitoring system, and overall conservative estimate of local SAR for the initial in vivo scans.[36,37]

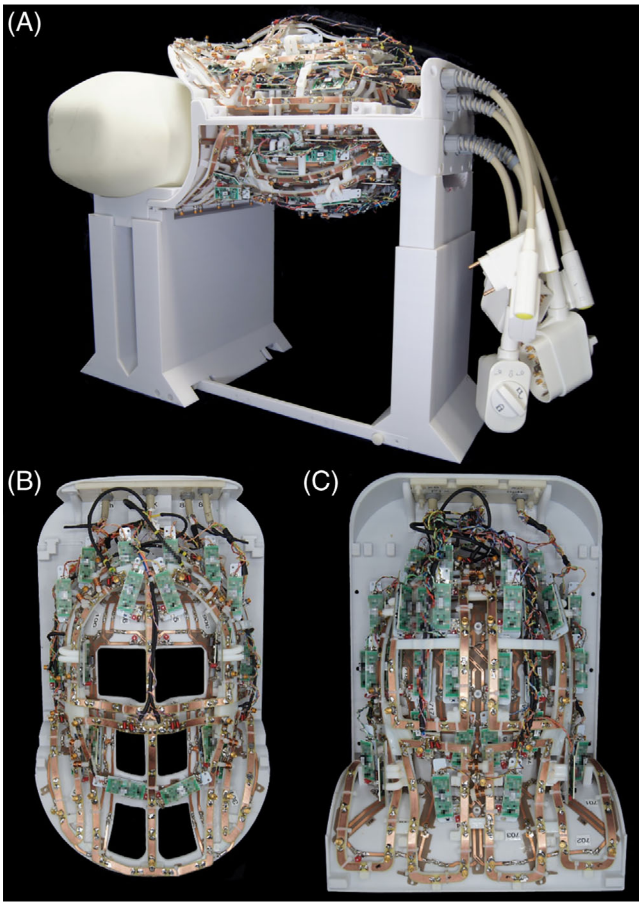

FIGURE 2 Fully assembled $16ch^{Tx}/64ch^{Rx}$ head–neck coil without the covers on top of the stand for bench top measurements. The Tx and Rx coil structures were merged into one anatomically shaped close-fitting housing. The coil housing is splittable to allow an easy entry for the patient

2.3 | Rx array

The 64 Rx elements were made from 0.5 mm-thick semi-flexible FR4 printed circuit board (PCB) material and mounted on the head–neck coil former. The PCB of the Rx structure was externally manufactured (Beta LAYOUT GmbH, Aarbergen, Germany). A single PCB sheet was designed for each anterior and posterior segment to adequately wrap the Rx coil array structure around the coil former. The geometrical loop layout used a mixture of overlapped elements[38] and a shared capacitance degenerately decoupled design[39] (Figure 3). Depending on the loop diameter, we subdivided each element symmetrically with six and eight gaps for small and large loop sizes, respectively. The coil's output circuit comprised a capacitive voltage divider (Series 11, Knowles Capacitors, Norwich, UK) and a variable series capacitor (GFX2700NM, Sprague Goodman, Westbury, NY) to impedance match the element's output to an optimized noise match of 75 Ω. Additionally, the output circuit board used an active detuning circuitry across one of the voltage divider capacitors. Active detuning during transmit was achieved using a PIN diode D_1 (MA4P4002B-402, Macom, Lowell, MA) in series with a tunable inductor L_{ACT} (150-02J08L, CoilCraft Inc., Cary, IL), which together with capacitor C_{T3} resonated at the Larmor frequency. Thus, when the PIN diode D_1 is forward-biased (Tx mode), the resonant parallel $L_{\mathrm{ACT}}C_{\mathrm{T3}}$ circuit inserts a high impedance in series with the coil loop, blocking current flow at the Larmor frequency during transmit. For further enhancement of coil safety, a passive detuning circuit was implemented comprised of a cross-diode D_{x} (MADP-011048TR3000, Macom, Lowell, MA), the RF-choke L_{RFC2} (1812CS-272, CoilCraft Inc., Cary, IL), and the capacitor C_{D}. The latter tunes out the increased inductance due to the slightly elongated copper trace of the passive detuning circuitry path.

Preamplifier decoupling was established to transform the preamplifier input impedance (11.2 + j10.4) Ω to a high series impedance within the loop.[10] The preamplifier's daughterboards were mechanically mounted on the helmet via 3D-printed plastic standoffs. All preamplifiers (Siemens Healthineers AG, Erlangen, Germany) were carefully oriented in the z-direction to minimize Hall effect issues.[40–42] We used the impedance change of the series matching capacitor to transform the input impedance of the preamplifier to a parallel inductance across C_{TM1} of the capacitive voltage divider. This parallel LC circuit resonated at the Larmor frequency and induced the needed high serial impedance into the coil loop. Thus, minimal current flowed in the loop. and inductive coupling to other coils was minimized despite the presence of residual mutual inductance.

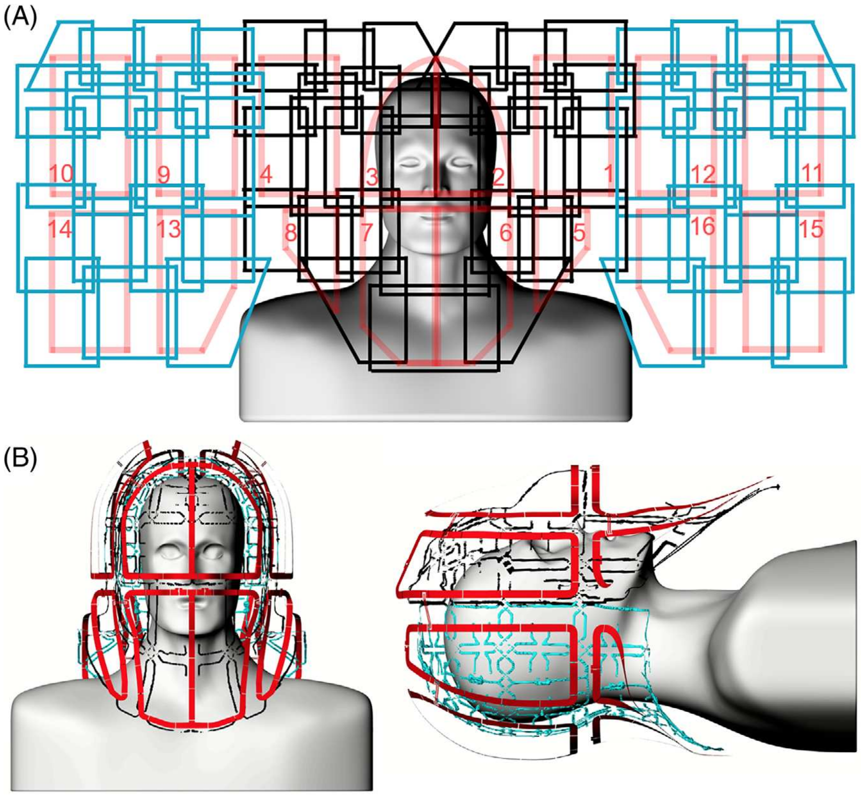

FIGURE 3 Unwrapped loop configuration of the constructed 16ch$^{\mathrm{Tx}}$/64ch$^{\mathrm{Rx}}$ head–neck coil (A). The anterior Rx coil comprises 24 elements (black), and the posterior segment consists of 40 Rx elements (blue). The Tx array is made of 16 elements, arranged in 2 z-stacked rows (red). The Tx loop elements are anatomically shaped and radially encompass the head and neck regions (B)

2.4 | Tx array

The 16-channel Tx array was anatomically shaped and mounted on the same Rx head–neck coil former while maintaining an offset of 3 cm to the Rx structure. The superior eight channels were shaped to conform anatomically along the head. The eight elements on the inferior ring were shaped to follow the neck and shoulder coil frame. The Tx loop element arrangement was laid out in a stacked dual row design with eight elements per row. The Tx array was also constructed using the 0.5 mm-thick semiflexible FR4 PCB material (0.5-Cu-35/0, Masterplatex e.K., Schönwalde-Glien, Germany), which was installed on the Tx rail mounting system. The Tx loop elements were separated with a 2 cm gap, and only the element pairs over the eyes and mouth shared a common conductor path and its series capacitors. This configuration enlarged eye and face cutouts in the coil housing to allow improved patient comfort. The circuit schematics for a representative Tx–Rx element are shown in Figure 4. Based on the electromagnetic simulation, we distributed series tuning capacitors (Series 11, Knowles Capacitors, Norwich, UK) every 3 cm. A variable high-power capacitor (60–0716-10 016-600; Tronser, Engelsbrand, Germany) was incorporated to adjust each element to the Larmor frequency. We used two symmetric matching capacitors C_{M2} to transform the Tx loop's impedance to 50 Ω. A series PIN diode D_2 (MA4P7470F-1072 T, Macom, Lowell, MA) was placed in each loop. Thus, the Tx elements had to be actively tuned by forward biasing the PIN diode while leaving the Tx loop off-resonance during reception. The bias for the PIN diode was supplied through an RF choke (1812CS-272, CoilCraft Inc., Cary, IL). To drive the 16 Tx loops, a bazooka balun was used before the 50 Ω matching network.

Adjacent Tx loops with the 2 cm geometrical gap were decoupled by incorporating a RID network[33] (Supporting Information Figure S1). This method also worked out for the adjacent element pairs that were placed at the two separated coil housing segments, where the decoupling inductor from one Tx element faces the oppositely wound inductor of the neighboring Tx element through the housing plastic wall. To enable a reliable alignment of this cross-housing coupling structure, the anterior coil segment closes the helmet via a snap-in mechanism and two bolt locks. Loop pairs with the shared conductor (eyes and mouth area) were tuned to degeneracy by correctly choosing the rung and loop capacitance to achieve sufficient decoupling.[43]

In the free spaces between the Tx structure and Rx structure, we installed the preamplifiers. Thus, the Tx and Rx structures share the same area of the coil former rather than exist as separate functionalities in two independent housings.

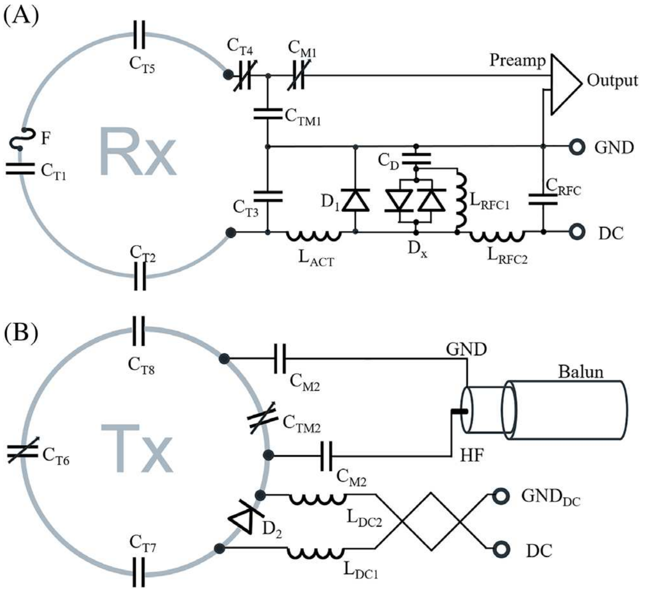

FIGURE 4 Circuit schematics of the Rx loop element (A) and Tx coil (B). Rx loop elements consist of tuning capacitors (C_{T1}, C_{T2}, C_{T3}, C_{T4}, C_{T5}), an active and passive detuning circuitry (D_1, D_X, C_D, L_{RFC1}), and a fast-switching RF fuse (F). The Tx elements consist of series tuning capacitors (C_{T6}, C_{T7}, C_{T8}), a PIN diode (D_2) for active tuning, a balanced drive port with C_{M2}, and a "bazooka balun" to eliminate common mode RF cable currents. The RF choke L_{RFC1} is needed to provide a stable DC voltage potential between the X-diode and the capacitor C_D during the bias switching transient C_{M2}, two matching capacitors.

2.5 | Coil bench measurements

The constructed Rx and Tx array coils were adjusted and optimized with a battery of standardized RF bench level metrics. These bench measurements verified the element tuning, active detuning, nearest-neighbor coupling, and preamplifier decoupling for each coil element. Prior to cable routing, we assessed the unloaded-to-loaded quality factor ratio (Q_{UL}/Q_L) of the Rx elements using the S_{21} double-probe method.[44] For this measurement, the actively detuned nonresonant neighbors were present, including the detuned Tx structure. Also, the frequency shift upon phantom loading was measured with the S_{21} double probe. After installing the cables, we used a custom-made coil plug simulator to control each Rx channel's detuning bias and to power the preamplifiers. All elements were pretuned to resonate at the Larmor frequency. The active detuning circuitry was adjusted by carefully controlling the variable inductance L of the active detuning circuit under an S_{21} double-probe measurement. For fine adjustments, each loop under testing was brought into the tuned state, whereas all neighboring elements were actively detuned. By performing an S_{11} measurement on a vector network analyzer in combination with an RF switching matrix (ZNB8, ZN-Z84, Rohde & Schwarz, Memmingen, Germany), we tuned and matched the Rx coil elements to 75 Ω at the Larmor frequency under a loaded condition. With the RF switch matrix, up to 24 channels could monitored simultaneously.

Nearest neighbor coupling was measured using a direct S_{21} measurement between pairs of elements using coaxial cables directly connected to the preamplifier sockets of the 2 elements under testing. When measuring the S_{21} between an adjacent pair, all other elements of the array were detuned. We measured the preamplifier decoupling of a given loop with all other loops detuned. Preamplifier decoupling was measured as the change in the double-probe S_{21} when the preamplifier socket was terminated in each of 2 different match conditions: In the first case, the coil was terminated with the powered low-impedance preamplifier. In the second case, the coil was terminated by 75 Ω.

The 16-channel Tx coil array was tuned under phantom loading to the Larmor frequency and matched to the 50 Ω system impedance to provide power-matched conditions. The decoupling was optimized by performing a direct S_{21} measurement between adjacent Tx elements, whereas the RID networks were adjusted to provide a sufficient interelement decoupling of <-16 dB. Additionally, the Q_{UL}/Q_Lratio for each Tx element was obtained when the coil element was placed within the populated but detuned array. The bazooka baluns at each Tx coaxial cable were measured with an S_{21} current injection RF probe.[45] Potential variations in tuning, matching, and coupling due to differently sized loading conditions were bench-tested with 5 subjects and the anthropomorphic head–neck phantom.

2.6 | Image acquisition and reconstruction

All experiments used a whole-body 7 Tesla scanner (Magnetom Terra, Siemens Healthineers, Erlangen Germany), equipped with 16 independent RF power amplifiers with 2 kW peak output power per channel, an SC72 gradient coil (G_{max} = 80 mT/m, slew rate = 200 T/m/s), and second- and partial third-order electronic shims. Standardized phantom tests were performed to identify any RF focusing or component heating from interactions between the Tx and Rx coils or between the gradient and RF components.[37]

The Tx field of the 16-channel head–neck array was characterized by mapping the $B_1{}^+$ magnitude in the Tx-only/Rx-only mode, where the signal was received through the 64 Rx elements.

$B_1{}^+$ field maps were acquired using the actual flip-angle imaging method[46] [3D gradient-echo, TR = 5.8/28 ms, TE = 2.73 ms, resolution: 3 mm isotropic, matrix: $64 \times 64 \times 56$, nominal flip angle = 60°, readout bandwidth = 260 Hz/pixel, acquisition time (TA) = 2:07 min]. The $B_1{}^+$ field maps were then normalized by the Tx voltage to obtain $B_1{}^+$ field map units of nT/V.

To assess the head–neck receive performance, SNR and G-factor maps were derived from 2D gradient echo images [TR / TE = 10 s / 3.82 ms, nominal flip angle = 30°, slice = 2 mm, matrix: 192×192, FOV: 256×176 mm^2, readout bandwidth = 340 Hz/Pixel, TA = 14:42 min]. Noise covariance information was acquired using the same pulse sequence but with no RF excitation. SNR maps were calculated for images formed from the noise-covariance weighted root sum-of-square of the individual channel images, where the weights utilize coil sensitivity maps and noise-correlation information.[10,45] To account for the impact of $B_1{}^+$ inhomogeneity on signal intensity over the FOV, the acquired flip-angle imaging map was spatially co-registered with the SNR maps and further used to rescale the native SNR. Because the SNR scan ensured full T_1 relaxation (TR of 10 s), the spatial SNR modulation depends only on the actual flip angle α. By normalizing the measured image SNR to sin(α), the pixel-wise SNR value at a 90-degree angle can be calculated. We compared the imaging performance to a commercially available 8-channel Tx/32-channel Rx brain-only array (Nova Medical, Inc., Wilmington, MA, USA).

Further in vivo measurements were carried out to assess high-resolution morphological combined head–neck imaging (gradient echo sequence: TR/TE/α = 40 ms/5 ms/20°, matrix: 344×344, resolution: $0.3 \times 0.3 \times 2$ mm, bandwidth: 320 Px/Hz). The in vivo feasibility study was performed under the approved institutional review board protocol at the Massachusetts General Hospital (Charlestown, MA, USA). Informed written consent was obtained from each volunteer prior to the study.

3 | RESULTS

RF bench Q-factor metrics of the 64-channel Rx array were measured before and after the addition of the Tx structure. The coil elements at the brain region comprise loop diameters of 40 mm, which showed an unloaded-to-loaded Q-ratio of Q_{UL}/Q_L = 2.8 when surrounded by its nonresonating neighboring Rx elements. The larger elements at the posterior neck region showed a *Q*-ratio of $Q_{\mathrm{UL}}/Q_{\mathrm{L}} = 8.1$, and the neck elements of the anterior segment exhibited a larger distance to the phantom, where a *Q*-ratio of $Q_{\mathrm{UL}}/Q_{\mathrm{L}} = 3.2$ was measured. For the two larger eye loops (rectangular-shaped, $a = 75$ mm and $b = 150$ mm) and the nose loop (quadratic-shaped, $a = 100$ mm), we measured an unloaded-to-loaded *Q*-ratio of 2.2 and 2.0, respectively. Thus, all constructed Rx loops were sample-noise dominated. When the detuned Tx elements were mounted onto the coil former, a slight decrease in the unloaded *Q*-factor of all Rx elements was observed. Upon sample loading, a resonance frequency upshift of 1–4 MHz was measured, where the larger Rx elements around the neck and face showed the higher range of the measured frequency shift (4 MHz). The decoupling between the tuned and active detuned states provided an isolation of >43 dB. Adjacent pairs of Rx loops showed an average geometrical decoupling of -15 ± 3 dB. The decoupling of next nearest neighbors ranged from −11 dB to −26 dB with a mean value of −18 dB. All decoupling values were further reduced by 17 ± 2 dB via preamplifier decoupling. Cable trap tuning was measured with a set of current probes and yielded an approximately 40 dB RF current suppression at the Larmor frequency.

The 16 Tx loop elements were mounted with an offset of 30 mm relative to the Rx helmet structure. The eight superior elements serving the brain region showed an average *Q*-ratio of 1.3 when surrounded by the detuned Rx structure and its nonresonant neighboring Tx elements. The unloaded-to-loaded *Q*-ratio of the inferior placed Tx elements ranged from 1.3 to 2.5. Upon sample loading, a resonance frequency upshift of up to 3.2 MHz was measured.

The installed RID networks could be easily adjusted to <−18 dB for minimal coupling between the adjacent Tx elements using the variable high-power capacitors (Supporting Information Figure S1). The next nearest Tx neighbors showed an interelement coupling ranging from −14 to −44 dB (mean = −19 dB) while loaded with the phantom. Thus, no further decoupling networks were necessary to decouple nonadjacent Tx elements. The overall Tx array's coupling values remained nearly constant across different body loads (Figure 5). When comparing the measured S-matrix obtained from the phantom with the simulated S-matrix (Supporting Information Figure S2), the measured decoupling values were overall more favorable. Some decoupling values, however, showed substantial differences between the S_{21} measurement and simulation.

Figure 6 shows the noise correlation coefficient matrices for both the 64-channel Rx elements of the head–neck coil and the 32-channel vendor coil. The 64-channel noise correlation ranged from 0.1% to 58%, with an average of 11.7% for the off-diagonal elements. For the 32-channel, these numbers ranged from 0.08% to 47%, with a mean of 5.1%. Figure 7 shows the unaccelerated SNR map comparisons between the constructed head–neck and vendor coils for the brain, neck, and C-spine regions obtained from an in vivo measurement. In the brain area, the SNR maps show roughly equivalent performance for both coils. In the central brain region, the constructed 64-channel coil showed slightly lower SNR than the 32-channel standard coil by 5%. However, in the face, lower brain stem, and C-spine region, the constructed 64-channel head–neck array outperformed the 32-channel vendor coil by a factor of 1.5, 3.4, and 5.2, respectively.

Figure 8 shows the inverse G-factor maps obtained from representative transversal slices from the brain, lower

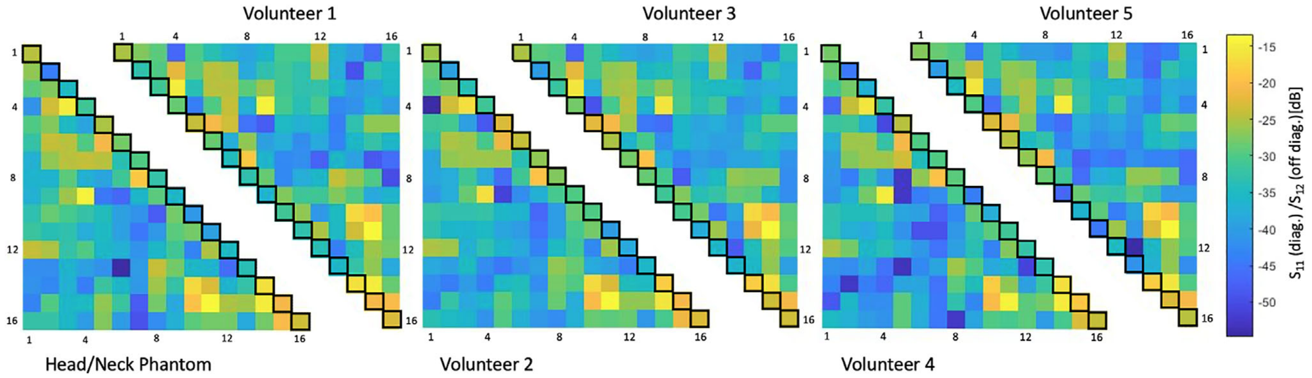

FIGURE 5 Six representative S-matrices of the 16-channel Tx array for different coil loads obtained from bench measurements. Matching (S_{11}, diagonal elements of each triangled matrix) and interelement coupling (S_{21}, off diagonal of each triangled matrix) were obtained from a head neck phantom and five volunteers. The 16-channel Tx coil shows only modest variation in coupling across different loading sizes

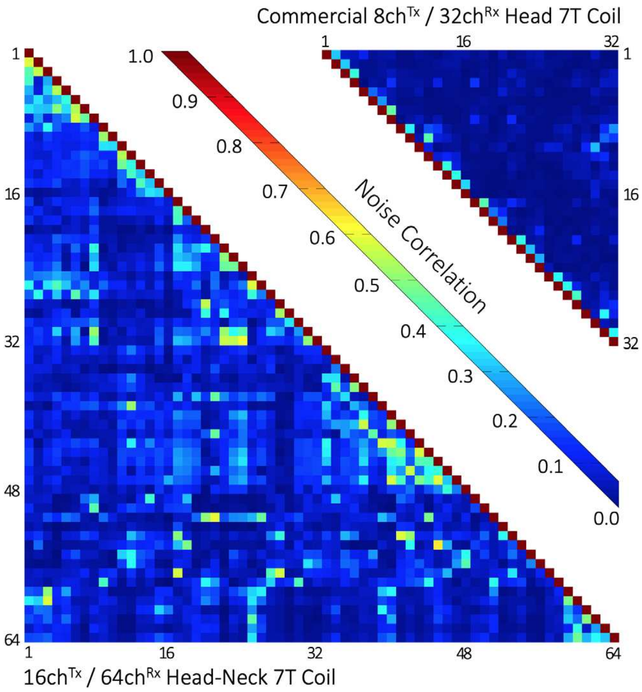

FIGURE 6 Noise correlation comparison between the constructed 16ch^{Tx}/64ch^{Rx} head–neck coil and the commercial 8ch^{Tx}/32ch^{Rx} head-only coil. The average noise correlations of the head–neck and the commercial coils were measured to be 11.7% (range 0.1%–58%) and 5.1% (0.08%–47%), respectively

brainstem, and C-spine for 1D and 2D accelerations. The constructed 64-channel head–neck array shows slightly improved G-factor values in the brain and brain stem areas. However, the 64-channel head–neck coil clearly outperforms the encoding capabilities of the vendor coil at the C-spine region: The constructed coil provides the ability to accelerate at approximately one unit higher at a given noise amplification compared to the 32-channel vendor brain array coil. It should be mentioned, however, that the commercially available brain coil is not suited for imaging the C-spine.

Figure 9 compares the simulated and measured B_1^+ field maps for the individual Tx channels obtained from the head–neck phantom. Quantitatively, the spatial distributions between simulations and their measurements showed good correlation for each individual channel. Compared to the measurement, the simulation provides about 11% higher B_1^+ efficiency. Locally, however, the B_1^+ values differ by up to ±24%. The B_1^+ field maps of both the CP and CP^{2+} configurations are shown in Supporting Information Figure S4. The maximum B_1^+ obtained from the CP mode at the center of the phantom was 96 nT/V in the simulation as compared to 80 nT/V in the measurement. Qualitatively, the CP and CP^{2+} shim configurations show a good agreement between the measured data and the simulation. On average, the simulation shows an 11% higher B_1^+ efficiency. Locally, however, the B_1^+ values differ in a range from ±20%.

SAR simulations obtained from a multi-compartment human body model are shown in Supporting Information Figure S5. The 10 g-SAR maps were generated with an input power of 1 W for the total simulation. The maximum SAR was determined to be 0.368 W/kg/W.

Initial B_1^+-shimmed in vivo images showed promising results for large-FOV head–neck imaging studies for clinical settings at 7 T. Figure 10 shows a sagittal image with a region of coverage from the full brain down to the C7 vertebral level with reasonable B_1^+ shimming.

4 | DISCUSSION

In this study, we designed, constructed, and validated a high-density 7 T head–neck coil consisting of 64 Rx and 16Tx coil elements. The coil was optimized to image the brain, brainstem, cerebellum, and C-spine; furthermore, patient comfort and user-friendliness at 7 T was addressed.

The Rx and Tx structures were merged into one housing rather than separating them into a receiver helmet and tubular Tx topology. Accomplishing this, the technical challenges associated with 7 T high-field MRI had to be solved within the highly space-constrained environment.

The array coil performance was evaluated via i) bench-level measurements such as Q_{UL}/Q_L-ratios, tuned-detuned isolation, and neighboring coupling; ii) system-level validations, which included component heating, and Tx B_1^+ maps; and iii) in vivo performance tests, which were carried out by pixel-wise SNR maps, G-factor maps, and noise correlation.

32-channel and 64-channel brain arrays are well understood for 7 T brain imaging.[12,14,47,48] However, when extending the coverage toward the neck and C-spine area, there are additional challenges present in the coil design and construction process. It renders the issue of Tx/Rx coupling and temporal signal stability more difficult and requires design alternations compared to array coils built with separated Rx and Tx structures.

The constructed coil showed slight improvements in both SNR and acceleration compared to the standard 32-channel brain array. As expected, most of the benefit was in the extended coverage when compared to the brain-only coil design. Previous coil hardware studies have shown that using 32 channels improve the quality of simultaneous brain and C-spine imaging at 3 T.[49] However, in order to serve the neck/C-spine region with detectors, the number of available elements around the brain has to be substantially reduced to cover the neck/C-spine if the total element count is fixed at 32. This renders brain imaging suboptimal compared to 32-channel brain-only

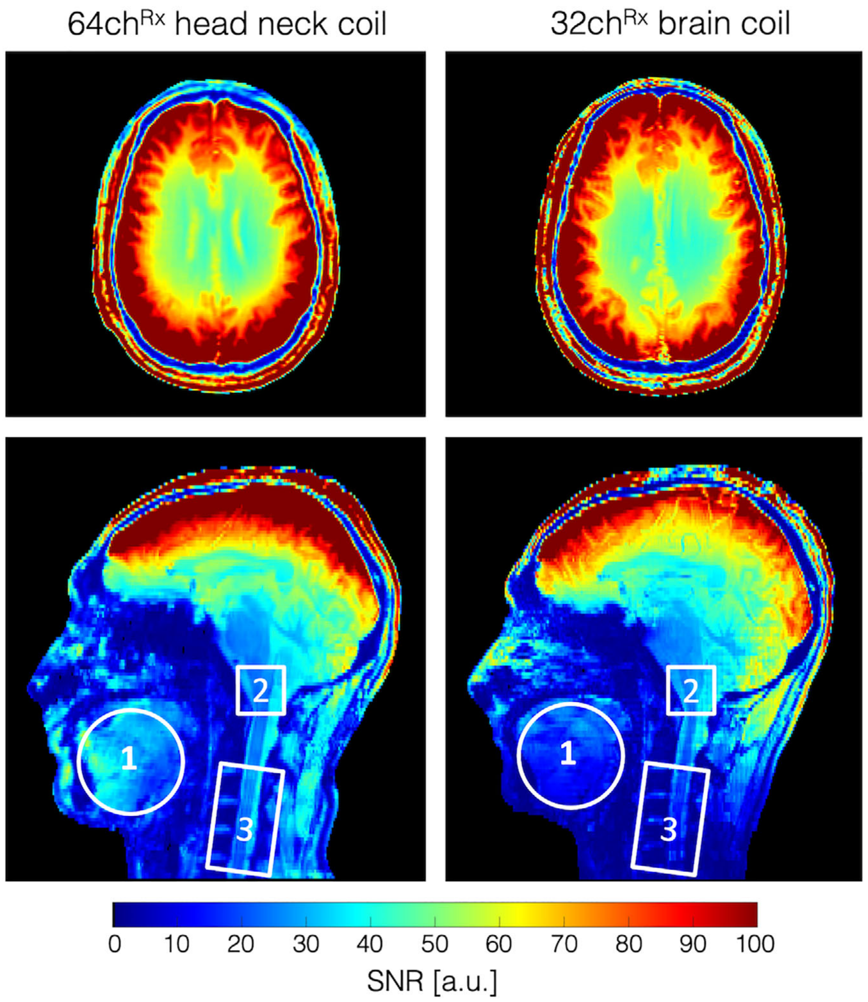

FIGURE 7 In vivo SNR map for the 64-channel head–neck array and the commercially available 32-channel head-only coil. In the brain area, the SNR maps show roughly equivalent performance for both coils. However, in the face, lower brain stem, and C-spine region, the 64-channel head–neck array outperforms the 32-channel vender coil by a factor of 1.5, 3.4, and 5.2, respectively C, cervical.

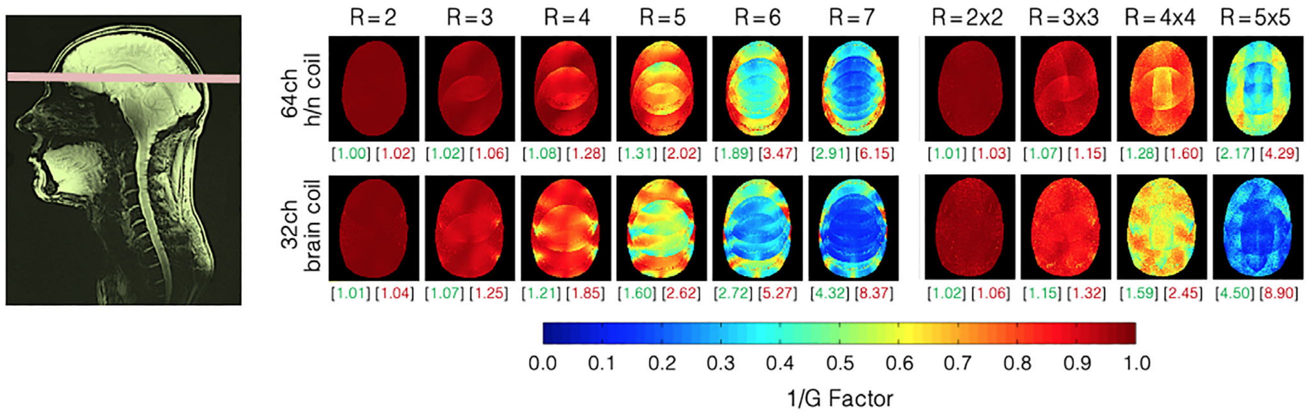

FIGURE 8 Inverse G-factors for representative slice obtained from the 64-channel head–neck and the 32-channel coils. In the brain region, the 64-channel head–neck coil shows slightly lower noise amplifications at all acceleration stages when compared to the 32-channel head coil. The green and red numbers in brackets indicate the mean and maximum G-factors, respectively (noninverted values). Information for slices in the neck area can be found in Supporting Information FigureS3

array coils. The customized 64-channel coil used in this hardware study addressed this limitation by providing sufficient coil elements to maintain the element count around the brain and provide new elements for the face, neck, and C-spine region. In our design, 42 coil elements serve the brain region, which yielded a slightly higher loop density compared to the standard 32-channel brain array.

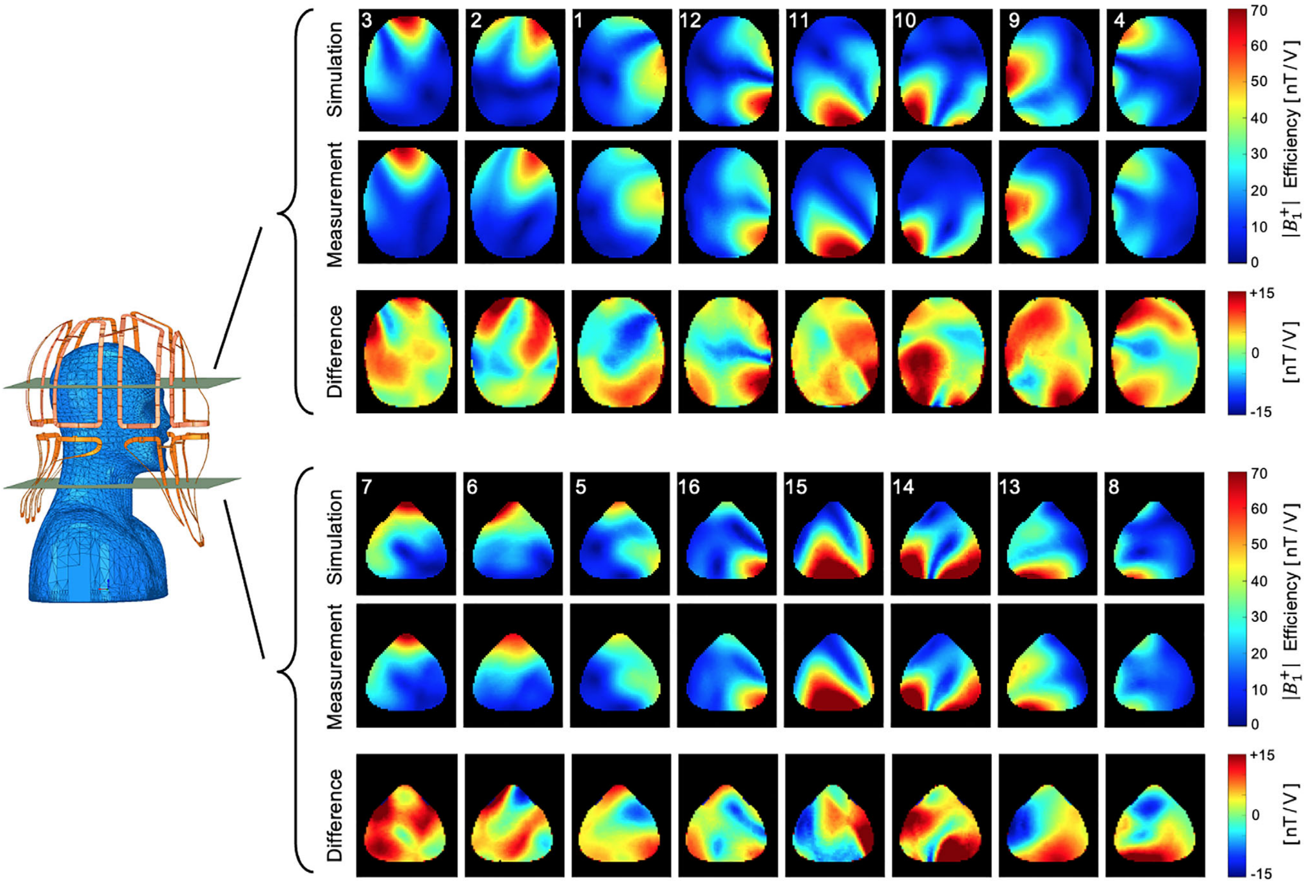

FIGURE 9 Simulated and measured $B_1{}^+$ field maps for each individual channel in 2 representative transverse slices of the brain and neck region. Qualitatively, the spatial distributions of the $B_1{}^+$ fields between the simulation and the measurement showed good correlation

Mounting the Rx and Tx structures on the same coil former shows increased interelement coupling between the Rx and Tx structures. In our first attempt, we incorporated a 15 mm spacing between both structures, which turned out to be insufficient for well-decoupled elements.[50] Actively detuned Rx elements showed overall increased coupling between the Tx channels, and this made it difficult to tune and match the Tx elements properly. In our second attempt, we used a 30 mm offset, which isolated both structures sufficiently. However, especially for the larger Rx coil elements at the neck region, an additional passive detuning circuitry was needed at the opposite side of the drive port to fully decouple the element from the Tx structure. This is attributed to the larger Rx elements with only one detuning location still being able to feature a dipole-like behavior, which highly couples into the Tx array. The incorporated second detuning break point helped to prevent this effect.

The coil construction and the safety assessment required an accurate electromagnetic simulation model. The lumped capacitor elements of the 16-channel Tx array were optimized using the co-simulation method.[32] The outcome was used to guide the Tx array construction process. For safety validation, it was also necessary to capture the interelement coupling behavior of the 16-channel Tx array in the simulation. This was a critical step to accurately model electromagnetic field quantities observed in the phantom. The bench-measured *S*-parameters demonstrated good agreement with the simulated results, indicating an overall successful implementation of the simulated guided design process. The adaptability of the RID networks between adjacent Tx elements added an increased degree of freedom for decoupling the Tx array under a loaded condition while maintaining 50 Ω at the drive port. The RID network was also well suited for decoupling adjacent Tx coil elements, which were geometrically separated by the posterior and anterior housing segments. Further decoupling networks of the nearest Tx neighbors were not necessary because a coupling of <−14 dB was achieved by the geometric distance. The Tx array's *S*-parameters showed only slight to moderate changes under different coil loads, maintaining the required critical tuning and matching condition in subjects of different sizes.

FIGURE 10 Combined head and neck image obtained from a gradient echo sequence, acquired with the constructed $16\text{ch}^{\text{Tx}}/64\text{ch}^{\text{Rx}}$ head–neck coil to demonstrate the extended coil coverage (gradient echo sequence: TR/TE/$\alpha = 40$ ms/5 ms/20°, M: 344 × 344, resolution: 0.3 × 0.3 × 2 mm, BW: 320 Px/Hz) BW, bandwidth; M, matrix.

The measured B_1^+ field maps qualitatively showed a good match between the simulated and measured fields. The differences are likely attributable to the complexity of the overall constructed RF coil system and the inadequacy of capturing all these details in the simulation model. In addition, the B_1^+ maps were simulated without including the receiving array in the model, which can attenuate the B_1^+ field overall or modulate it locally.[51]

In general, the constructed coil showed better overall decoupling values between the elements compared to the simulation, with some larger discrepancies in some cases. This mismatch can compromise the accuracy of the coil's safety assessment. For this reason, a second shim configuration (CP^{2+}) was evaluated. Both shim sets showed a good agreement between simulation and measurement, with local differences of ±20%. However, a 2.5-fold safety factor was added to account for a conservative local SAR estimation.

The mean noise correlation between Rx coil elements was 11.7%. The anterior Rx elements serving the neck area showed the highest noise correlation, with values of up to 58%. These coil elements deliberately have a greater distance from the neck region to allow different body shapes to fit comfortably inside the coil. However, these coil elements are underloaded due to the larger distance to the body, which increases the Q-factor; thus, the coupling between the coil elements increases. In the brain, the receiver sensitivity is comparable with the standard 32-channel head coil. In the central brain region, the constructed head–neck coil showed slightly lower SNR (5%). This is clearly attributed to the overall larger coil size. Key design criteria for the coil were its robust usability for everyday clinical use and to fit larger head-sized subjects when compared to the commercially available 8-channel Tx/32-channel Rx coil array. From the latter implication, the coil size was deliberately chosen to be larger than the commercially available head coil.

Initial large FOV in vivo imaging demonstrated the feasibility of capturing both the brain and C-spine region within one acquisition at 7 T using B_1^+ shimming from 16 Tx channels and the highly parallel reception of 64 coil elements. In future studies, the constructed 7 T array coil will be used to acquire new informative data of the central nervous system involving the brain and spinal cord. The ability of combined whole brain and C-spine cord imaging to provide more insight into the functional coupling between the brain and spinal cord will be valuable.

5 | CONCLUSION

A 64-channel Rx array coil with 16 integrated Tx channels was simulated, constructed, and tested for combined brain and cervical spine imaging at 7 T. We compared the coil to a 32-channel brain-only coil. The highly parallel coil designed in this study is well suited for either brain examinations or head–neck–spine studies. The high SNR of the head–neck Rx coil will likely improve clinical and research studies focused on brain and spinal regions.

ACKNOWLEDGMENTS

We thank Bernd Stoeckel from Siemens Healthineers (Siemens Healthcare GmbH, Erlangen, Germany). for his technical assistance and helpful discussions. This work was supported by the National Institutes of Health [5R01EB006847, 1P41EB030006, 1S10OD023637]; and the Federal Ministry of Education and Research Germany (BMBF) [IN2016-2-226].

CONFLICT OF INTERESTS

Rene Gumbrecht, Ralph Kimmlingen, Markus Adriany, Yulin Chang, Christina Triantafyllou: employees of Siemens Healthineers.

DATA AVAILABILITY STATEMENT

Original data are available from the corresponding author upon reasonable request. The data that support findings of this study are openly available in github at https://github.com/keyarray/headneckcoil.[52]

ORCID

Markus W. May https://orcid.org/0000-0003-3869-9681
Sam-Luca J. D. Hansen https://orcid.org/0000-0002-5353-5573
Mirsad Mahmutovic https://orcid.org/0000-0001-9178-4194
Alina Scholz https://orcid.org/0000-0002-3324-6889
Nicolas Kutscha https://orcid.org/0000-0002-9182-8748
Bastien Guerin https://orcid.org/0000-0002-4746-0886
Jason P. Stockmann https://orcid.org/0000-0001-8454-5347
Robert L. Barry https://orcid.org/0000-0001-6271-9414
Yulin Chang https://orcid.org/0000-0003-2714-2634
Susanne Knake https://orcid.org/0000-0002-6298-0513
Lawrence L. Wald https://orcid.org/0000-0001-8278-6307
Boris Keil https://orcid.org/0000-0003-0805-8330

TWITTER

Markus W. May @Mr_Mayparty

REFERENCES

1. Bruschi N, Boffa G, Inglese M. Ultra-high-field 7-T MRI in multiple sclerosis and other demyelinating diseases: from pathology to clinical practice. *Eur Radiol Exp*. 2020;4:59.
2. Abraham J. Imaging for head and neck cancer. *Surg Oncol Clin N Am*. 2015;24:455-471.
3. Ohgiya Y, Oka M, Hiwatashi A, et al. Diffusion tensor MR imaging of the cervical spinal cord in patients with multiple sclerosis. *Eur Radiol* 2007;17:2499–2504.
4. Ciccarelli O, Wheeler-Kingshott CA, McLean MA, et al. Spinal cord spectroscopy and diffusion-based Tractography to assess acute disability in multiple sclerosis. *Brain*. 2007;130:2220-2231.
5. Valsasina P, Benedetti B, Caputo D, Perini M. Diffusion tensor MRI of the spinal cord in amyotrophic lateral sclerosis. In Proceedings of the 13th Scientific Meeting ISMRM, Seattle, WA, 2006. p. 986.
6. Springer E, Dymerska B, Cardoso PL, et al. Comparison of routine brain imaging at 3 T and 7 T. *Invest Radiol* 2016;51:469–482.
7. Reichenbach JR, Haacke EM. High-resolution BOLD Venographic imaging: a window into brain function. *NMR Biomed*. 2001;14:453-467.
8. Sharma HK, Feldman R, Delman B, et al. Utility of 7 Tesla MRI brain in 16 “MRI negative” epilepsy patients and their surgical outcomes. *Epilepsy Behav Rep* 2021;15:100424.
9. Feldman RE, Delman BN, Pawha PS, et al. 7T MRI in epilepsy patients with previously normal clinical MRI exams compared against healthy controls. *PLoS One* 2019;14:e0213642.
10. Roemer PB, Edelstein WA, Hayes CE, Souza SP, Mueller OM. The NMR phased array. *Magn Reson Med*. 1990;16:192-225.
11. Wiggins GC, Wiggins CJ, Potthast A et al. A 32 channel receive-only head coil and detunable transmit birdcage coil for 7 Tesla brain imaging. In Proceedings of the 14th Annual Meeting of ISMRM, Seattle, WA, 2006. p. 415.
12. Ledden PJ, Mareyam A, Wang S, Gelderen P, Duyn J. 32 channel receive-only SENSE Array for brain imaging at 7T. In Proceedings of the 15th Annual Meeting of ISMRM; Berlin, Germany. 2007. p. 242.
13. Ledden PJ, Mareyam A, Wang S, van Gelderen P, Duyn J. Twenty-four channel receive-only array for brain imaging at 7T. Proceedings of the 14th Annual Meeting of ISMRM, Seattle, WA, 2006. p. 422.
14. Mareyam A, Kirsch JE, Chang Y, Madan G, Lawrence L. Wald LL. A 64-channel 7T array coil for accelerated brain MRI. In Proceedings of the 2021 ISMRM & SMRT Annual Meeting and Exhibition, Virtual meeting, 2020. p. 0764.
15. Sigmund EE, Suero GA, Hu C, et al. High-resolution human cervical spinal cord imaging at 7T. *NMR Biomed* 2012;25:891–899.
16. Zhao W, Cohen-Adad J, Polimeni JR, et al. Nineteen-channel receive array and four-channel transmit array coil for cervical spinal cord imaging at 7T. *Magn Reson Med* 2014;72:291–300.
17. Yu Z, Zhang B, Walczyk J, Chen G, Wiggins G. A 6-channel transmit-receive coil array for 7T cervical spine imaging. In Proceedings of the 24th Annual Meeting of ISMRM, Singapore, 2016. p. 2145.
18. Zhang B, Seifert AC, Kim J-W, Borrello J, Xu J. 7 Tesla 22-channel wrap-around coil array for cervical spinal cord and brainstem imaging. *Magn Reson Med*. 2017;78:1623-1634.
19. Ibrahim TS, Lee R, Baertlein BA, Abduljalil AM, Zhu H, Robitaille P-ML. Effect of RF coil excitation on field inhomogeneity at ultra high fields: a field optimized TEM resonator. *Magn Reson Imaging*. 2001;19:1339-1347.
20. Katscher U, Börnert P, Leussler C, van den Brink JS. Transmit SENSE. *Magn Reson Med*. 2003;49:144-150.
21. Zhu Y. Parallel excitation with an array of transmit coils. *Magn Reson Med*. 2004;51:775-784.
22. Poser BA, Anderson RJ, Guérin B, et al. Simultaneous multislice excitation by parallel transmission. *Magn Reson Med* 2014;71:1416–1427.
23. Keil B, Triantafyllou C, Hamm M, Wald L, Martinos A. Design optimization of a 32-channel head coil at 7T. In Proceedings of the 18th Annual Meeting of ISMRM, Stockholm, Sweden, 2010. p. 1493.
24. Shajan G, Kozlov M, Hoffmann J, Turner R, Scheffler K, Pohmann R. A 16-channel dual-row transmit array in combination with a 31-element receive array for human brain imaging at 9.4 T. *Magn Reson Med*. 2014;71:870-879.
25. Gao Y, Mareyam A, Sun Y, et al. A 16-channel AC/DC Array coil for anesthetized monkey whole-brain imaging at 7T. *Neuroimage* 2020;207:116396.
26. Keil B, Blau JN, Biber S, et al. A 64-channel 3T Array coil for accelerated brain MRI. *Magn Reson Med* 2013;70:248–258.
27. Clément J, Gruetter R, Ipek Ö. A combined 32-channel receive-loops/8-channel transmit-dipoles coil array for whole-brain MR imaging at 7T. *Magn Reson Med*. 2019;82:1229-1241.

28. Rollins JD, Collins JS, Holden KR. United States head circumference growth reference charts: birth to 21 years. *J Pediatr*. 2010;156:907-913.
29. Robert Koch Institut. 92 | Anthropometrie und Blutdruck | Kopfumfang. Berlin, Germany: Robert Koch Instutut 2011:11.
30. Glover GH FBIRN Stability phantom QA procedures. 2009-09-27)[2012-09-01]. 2005. https://www.nitrc.org/frs/download.php/275/%EE%80%80fBIRN%EE%80%81_phantom_qaProcedures.pdf
31. Duan Q, Duyn JH, Gudino N, et al. Characterization of a dielectric phantom for high-field magnetic resonance imaging applications. *Med Phys* 2014;41:102303.
32. Kozlov M, Turner R. Fast MRI coil analysis based on 3-D electromagnetic and RF circuit co-simulation. *J Magn Reson*. 1997;2009:147-152.
33. Avdievich NI, Pan JW, Hetherington HP. Resonant inductive decoupling (RID) for transceiver arrays to compensate for both reactive and resistive components of the mutual impedance. *NMR Biomed*. 2013;26:1547-1554.
34. Vogel MH, Kleihorst RP. Large-scale simulations including a human-body model for MRI. *IEEE/MTT-S Int Microw Symp*. 2007;2007:1345-1348.
35. Eichfelder G, Gebhardt M. Local specific absorption rate control for parallel transmission by virtual observation points. *Magn Reson Med*. 2011;66:1468-1476.
36. Le Garrec M, Gras V, Hang M-F, Ferrand G, Luong M, Boulant N. Probabilistic analysis of the specific absorption rate intersubject variability safety factor in parallel transmission MRI. *Magn Reson Med*. 2017;78:1217-1223.
37. Hoffmann J, Henning A, Giapitzakis IA, et al. Safety testing and operational procedures for self-developed radiofrequency coils. *NMR Biomed* 2016;29:1131–1144.
38. Raaijmakers AJE, Luijten PR, van den Berg CAT. Dipole antennas for ultrahigh-field body imaging: a comparison with loop coils. *NMR Biomed*. 2016;29:1122-1130.
39. Wang J. A novel method to reduce the signal coupling of surface coils for MRI. In Proceedings of the 4th Annual Meeting of ISMRM, NewYork, NY, USA, 1996. p. 1434
40. Possanzini C, Boutelje M. Influence of magnetic field on preamplifiers using GaAs FET technology. Proceedings of the 16th Annual Meeting of ISMRM, Toronto, Canada. 2008;
41. Ian Hoult D, Kolansky G. A magnetic-field-tolerant low-noise SiGe pre-amplifier and T/R switch. In Proceedings of the 18th Annual Meeting of ISMRM, Stockholm, Sweden, 2010. p. 649
42. Lagore R, Roberts B, Fallone BG, de Zanche N. Comparison of three preamplifier technologies: variation of input impedance & noise figure with B0 field strength. In Proceedings of the 19th Annual Meeting of ISMRM, Montréal, Québec, Canada, 2011. p. 1864
43. Lee RF, Giaquinto RO, Hardy CJ. Coupling and decoupling theory and its application to the MRI phased array. *Magn Reson Med*. 2002;48:203-213.
44. Hoult DI. The NMR receiver: a description and analysis of design. *Prog Nucl Magn Reson Spectrosc*. 1978;12:41-77.
45. Kellman P, McVeigh ER. Image reconstruction in SNR units: a general method for SNR measurement. *Magn Reson Med*. 2005;54:1439-1447.
46. Yarnykh VL. Actual flip-angle imaging in the pulsed steady state: a method for rapid three-dimensional mapping of the transmitted radiofrequency field. *Magn Reson Med*. 2007;57:192-200.
47. Adriany G, Auerbach EJ, Snyder CJ, et al. K A 32-channel lattice transmission line array for parallel transmit and receive MRI at 7 Tesla. *Magn Reson Med* 2010;63:1478–1485.
48. Williams SN, Allwood-Spiers S, McElhinney P, et al. A nested Eight-Channel transmit Array with open-face concept for human brain imaging at 7 Tesla. *Front Phys Ther* 2021;9:1-16. doi: 10.3389/fphy.2021.701330
49. Cohen-Adad J, Mareyam A, Keil B, Polimeni JR, Wald LL. 32-channel RF coil optimized for brain and cervical spinal cord at 3 T. *Magn Reson Med*. 2011;66:1198-1208.
50. May M, Etzel R, Laleh G et al. Design Considerations of a 64-Channel Receive/16-Channel Transmit Coil Array for Head, Neck, and Cervical-Spine Imaging at 7 T. In Proceedings of the 27th Annual Meeting of ISMRM, Montréal, Québec, Canada, 2019. p. 1519
51. Golestanirad L, Keil B, Angelone LM, Bonmassar G, Mareyam A, Wald LL. Feasibility of using linearly polarized rotating birdcage transmitters and close-fitting receive arrays in MRI to reduce SAR in the vicinity of deep brain simulation implants. *Magn Reson Med*. 2017;77:1701-1712.
52. May M. Github Respository. Available at: https://github.com/keyarray/headneckcoil. Access on: 03.05.2022

SUPPORTING INFORMATION

Additional supporting information may be found in the online version of the article at the publisher's website.

FIGURE S1. Schematic and implementation of the resonant inductive decoupling (RID) structure to be used for isolating adjacent Tx coil pairs. This decoupling structure was also used to decouple direct neighboring elements across the split housing segments on different formers. In this case, the Former P illustrates the represents of the posterior coil former where Former A is the anterior former.

FIGURE S2. Comparison between measured (A) and simulated (B) *S*-Parameters. Values are obtained from a head–neck agar phantom load. The diagonal elements refer to the S_{11} matching of the coil, where the S_{21} off-diagonal show the interelement coupling. The constructed head and neck coil shows overall more favorable decoupling values in comparison to its simulated version.

FIGURE S3. Inverse G-factors for three transverse slices obtained from the 64-channel head–neck and the 32-channel coils. In the brain region, the 64-channel head–neck coil shows slightly lower noise amplifications at all acceleration stages when compared to the 32-channel head coil. At the neck region, the lower G-factors of the 64-channel coil provide roughly one additional unit of acceleration for a given noise amplification factor when compared to the 32-channel coil. The green and red numbers in brackets indicate the mean and maximum G-factors, respectively (non-inverted values).

FIGURE S4. Comparison of $B_1{}^+$ efficiency between simulated and measured phantom data obtained in the center of the head–neck coil. *Top row*: CP shim configuration with preset phases: Ch1: 64°, Ch2: 20°, Ch3: 340°, Ch4: 296°, Ch5: 54°, Ch6: 18°, Ch7: 342°, Ch8: 306°, Ch9: 249°, Ch10: 203°, Ch11: 157°, Ch12: 111°, Ch13: 226°, Ch14: 198°, Ch15: 162°, Ch16: 134°. *Bottom row*: CP^{2+} shim configuration with 90° increments. Qualitatively, both shim configurations show good correlations of the B_1^+ field pattern. The simulation shows an 11% higher B_1^+ efficiency overall. Locally, however, the B_1^+ values differ in a range from −12% to +18%.

FIGURE S5. Simulated 10 g-SAR with 1 W total input power (for the total simulation) for the CP shim configuration of the human multicompartment model. Sagittal and coronal slices show a maximum intensity projection (MIP) map of the SAR. The maximum SAR was measured to be 0.368 W/kg/W.

How to cite this article: May MW, Hansen S-LJD, Mahmutovic M, et al. A patient-friendly 16-channel transmit/64-channel receive coil array for combined head–neck MRI at 7 Tesla. *Magn Reson Med*. 2022;1-15. doi: 10.1002/mrm.29288

NeuroImage 238 (2021) 118256

Contents lists available at ScienceDirect

NeuroImage

journal homepage: www.elsevier.com/locate/neuroimage

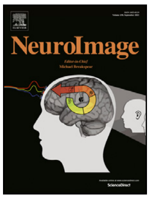

A 48-channel receive array coil for mesoscopic diffusion-weighted MRI of *ex vivo* human brain on the 3 T connectome scanner[☆]

Alina Scholz[a,*], Robin Etzel[a], Markus W. May[a], Mirsad Mahmutovic[a], Qiyuan Tian[b,c], Gabriel Ramos-Llordén[b,c], Chiara Maffei[b,c], Berkin Bilgiç[b,c,d], Thomas Witzel[b,c], Jason P. Stockmann[b,c], Choukri Mekkaoui[b,c], Lawrence L. Wald[b,c,d], Susie Yi Huang[b,c,d], Anastasia Yendiki[b,c], Boris Keil[a,e]

[a] *Institute of Medical Physics and Radiation Protection (IMPS), TH-Mittelhessen University of Applied Sciences (THM), 14 Wiesenstrasse, Giessen 35390, Germany*
[b] *A.A. Martinos Center for Biomedical Imaging, Department of Radiology, Massachusetts General Hospital, Boston, MA, USA*
[c] *Harvard Medical School, Boston, MA, USA*
[d] *Harvard-MIT Division of Health Sciences and Technology, Cambridge, MA, USA*
[e] *Center for Mind, Brain and Behavior (CMBB), Marburg, Germany*

ARTICLE INFO

Keywords:
Magnetic resonance imaging
Diffusion-weighted imaging
RF coil
Receive array coil
Brain imaging
Ex vivo brain

ABSTRACT

In vivo diffusion-weighted magnetic resonance imaging is limited in signal-to-noise-ratio (SNR) and acquisition time, which constrains spatial resolution to the macroscale regime. *Ex vivo* imaging, which allows for arbitrarily long scan times, is critical for exploring human brain structure in the mesoscale regime without loss of SNR. Standard head array coils designed for patients are sub-optimal for imaging *ex vivo* whole brain specimens. The goal of this work was to design and construct a 48-channel *ex vivo* whole brain array coil for high-resolution and high *b*-value diffusion-weighted imaging on a 3T Connectome scanner. The coil was validated with bench measurements and characterized by imaging metrics on an agar brain phantom and an *ex vivo* human brain sample. The two-segment coil former was constructed for a close fit to a whole human brain, with small receive elements distributed over the entire brain. Imaging tests including SNR and G-factor maps were compared to a 64-channel head coil designed for *in vivo* use. There was a 2.9-fold increase in SNR in the peripheral cortex and a 1.3-fold gain in the center when compared to the 64-channel head coil. The 48-channel *ex vivo* whole brain coil also decreases noise amplification in highly parallel imaging, allowing acceleration factors of approximately one unit higher for a given noise amplification level. The acquired diffusion-weighted images in a whole *ex vivo* brain specimen demonstrate the applicability and advantage of the developed coil for high-resolution and high *b*-value diffusion-weighted *ex vivo* brain MRI studies.

1. Introduction

Diffusion MRI (dMRI) is a powerful, non-invasive technique for imaging axonal orientations as well as characterizing white and gray matter microstructure (Conturo et al., 1999; Lagana et al., 2010; McNab et al., 2009; Mori and Zhang, 2006; Okano and Mitra, 2015). The basic premise of dMRI in the human brain is that the diffusion of water molecules in white matter is anisotropic, and that its preferential direction is aligned with the orientation of the underlying fibers (Mori and Zhang, 2006). A series of images, each sensitized to diffusion in a different direction, are acquired and used to infer the most likely orientation of water displacement in every voxel (Basser et al., 1994).

Abbreviations: 48ch, 48-channel; 64ch, 64-channel; ABS, acrylonitrile butadiene styrene; BW, bandwidth; CAD, computer aided design; CSD, constrained spherical deconvolution; dMRI, Diffusion MRI; DKI, diffusion kurtosis imaging; DTI, diffusion tensor imaging; DWI, Diffusion-Weighted Imaging; DWMRI, Diffusion-weighted Magnetic Resonance Imaging; EPI, echo planar imaging; EPROM, Erasable Programmable Read-Only Memory; F, flip angle; FA, fractional anisotropy; FOD, fiber orientation distribution; FOV, field of view; M, matrix; MRI, Magnetic Resonance Imaging; MSMT-CSD, multi-shell, multi-tissue, constrained, spherical deconvolution; PC, polycarbonate; PCB, printed circuit board; PD, proton density; PLP, periodate-lysine-paraformaldehyde; RF, radio frequency; ROI, region of interest; SMS, simultaneous multislice; SNR, signal-to-noise-ratio; TE, echo time; TR, repetition time; VNA, vector network analyzer.

[☆] Funding: This work was supported by the National Institutes of Health [R01EB021265, 1U01EB026996, R01HL131635, 1P41EB030006]; and the Federal Ministry of Education and Research Germany (BMBF) [IN2016-2-226].

[*] Corresponding author.
E-mail address: alina.scholz@lse.thm.de (A. Scholz).

https://doi.org/10.1016/j.neuroimage.2021.118256.
Received 27 April 2021; Received in revised form 4 June 2021; Accepted 7 June 2021
Available online 9 June 2021.

There are several requirements that increase the acquisition time needed for whole-brain dMRI. High spatial resolution is desirable for resolving small brain structures. A large number of diffusion directions must be sampled to improve the angular resolution, *i.e.,* the smallest angle between crossing fiber bundles that can be resolved. Finally, advanced dMRI sampling schemes may require images to be acquired with multiple *b*-values. Satisfying all these requirements would lead to acquisition times that are prohibitive for *in vivo* imaging in the absence of any image acceleration. As a result, trade-offs must be made that restrict *in vivo* whole-brain dMRI to the macroscale regime (Okano and Mitra, 2015; Zeng, 2018), with voxel sizes on the order of 1 to 3 mm. Motion artifacts, which are exacerbated by long acquisitions, and distortions near tissue-air interfaces further degrade the effective resolution that is achievable *in vivo*.

Many of these issues can be circumvented in *ex vivo* dMRI, which allows for longer acquisition times, absence of motion and significantly reduced susceptibility artifacts with appropriate sample preparation (Roebroeck et al., 2019). Furthermore, *ex vivo* imaging enables the placement of coil elements closer to the actual brain tissue to maximize sensitivity. Thus, *ex vivo* imaging can achieve substantially higher spatial and angular resolution, permitting the anatomy and microstructure of complex fiber pathways to be imaged at the mesoscale, sub-millimeter regime, well beyond what is feasible *in vivo*. The impressive level of anatomical detail that can be resolved by *ex vivo* dMRI has already been demonstrated on a variety of human tissue samples (Augustinack et al., 2010; Beaujoin et al., 2018; Fritz et al., 2019; Miller et al., 2011; Modo et al., 2016). *Ex vivo* dMRI, in combination with optical imaging, is an excellent tool for validating dMRI acquisition and analysis methods in human brain tissue (Jones et al., 2020; Mollink et al., 2017).

However, various challenges arise when acquiring *ex vivo* dMRI. These primarily include reduced diffusivity and decreased T2, caused mainly by the fixation, tissue dehydration and lower probe temperature (D'Arceuil et al., 2007; Pfefferbaum et al., 2004; Roebroeck et al., 2019). As a result, dMRI data must be acquired with higher *b*-values *ex vivo* to achieve similar diffusion contrast as *in vivo.* Furthermore, when a conventional *in vivo* head coil is used, it is challenging to center the *ex vivo* brain in the coil and to ensure that it remains stable throughout the long scan time.

In addition to the above challenges, the higher spatial resolution of *post mortem* scans comes at the cost of lower signal-to-noise-ratio (SNR). Several strategies for improving SNR in high-resolution *ex vivo* dMRI have been proposed and tested, mainly focusing on higher magnetic field strengths (Pallebage-Gamarallage et al., 2018; Plantinga et al., 2016), small-bore MRI scanners (Augustinack et al., 2010; Calamante et al., 2012) or high-performance gradient systems (McNab et al., 2013). One of the main innovations introduced by the NIH Blueprint Human Connectome Project was the development of human scanners with ultra-high gradients, which allow high *b*-values to be achieved without loss of SNR (Setsompop et al., 2013). Initial results have already shown the advantages of a 300 mT/m gradient system for imaging whole post-mortem human brains at 0.6 mm isotropic resolution (McNab et al., 2013), or smaller, non-human primate brain samples at 0.8 mm isotropic resolution (Eichner et al., 2020). Those results were obtained with an *in vivo* head coil. Dedicated *ex vivo* brain coils are known to increase signal reception sensitivity, and a few studies have shown the benefits of multi-channel brain array coils for *ex vivo* tissue imaging applications (Edlow et al., 2019; Roebroeck et al., 2015; Sengupta et al., 2018).

The aim of this study was to push the limits of spatial and angular resolution in *ex vivo* dMRI by designing, constructing, and validating a 48-channel (48ch) receive array coil for *ex vivo* whole human brain examinations. The array coil was developed for high spatial resolution and high *b*-value dMRI acquisitions with long scan times (a few hours to a few days) on the 3 T Connectome scanner (McNab et al., 2013; Setsompop et al., 2013). This work presents high-sensitivity *ex vivo* diffusion MRI results obtained in a whole human brain specimen at mesoscale resolution (0.73 mm isotropic) using the 48ch receive coil on the 3 T Connectome scanner and expands on preliminary results that were published in conference proceedings (Scholz et al., 2019).

2. Material and methods

2.1. Coil design and construction

To closely cover a whole human brain, we designed an anatomically-shaped *ex vivo* brain coil former (Fig. 1a and b) based on a nonlinear brain atlas of the International Consortium for Brain Mapping (ICBM). The coil housing was modeled with 3D computer aided design (CAD) software (Rhino3D, Robert McNeel & Associates, Seattle, WA, USA, version 6). It was designed to completely surround the brain with minimal space between the coil elements and imaging volume. The coil former was split into an upper and lower part, such that a whole brain can be placed inside the coil container. Both coil segments close with an overlapping rim structure (Fig. 1c). The coil container can accommodate whole brains with dimensions of 140 mm in the left-to-right direction, an anterior-to-posterior diameter of 182 mm, and a superior-inferior distance of 110 mm. The completed array coil is shown in Fig. 1e–h.

In the bottom coil segment, we incorporated the mechanics for a plugging slide mechanism (Fig. 1g and h), which directly plugs it into the scanner's patient bed. The top coil segment is connected to the scanner using two standard multi-channel coil plugs. The *ex vivo* coil container was designed to allow the brain to be placed at the isocenter of the scanner.

The optimum channel count for the constructed *ex vivo* brain array was determined by (1) the given area of the coil former's surface, and (2) a suitable coil element's *Q*-ratio for maintaining sample noise domination. These constraints resulted in a loop count of 48 and a loop diameter of 54 mm, which comprises an inductance of about 203 nH. The positions of the 48 coil elements on the outer surface of the coil former were derived from a hexagonal/pentagonal tiling pattern (Wiggins et al., 2006), with 30 and 18 coil elements located on the top and bottom segments, respectively (Fig. 1d).The position and outline of all loop elements, which are decoupled geometrically from neighboring loops by critical overlap (Roemer et al., 1990), were incorporated in the CAD model. The majority of the loops was circularly formed, whereas some loops were arbitrarily shaped to fit over the rim structure. The critical overlap was determined empirically in previously tested bench measurements and is about 0.27 times the loop diameter. Standoffs for circuit boards and cable routing were implemented to provide stable mounting positions. The coil former including its cover were then 3D-printed in polycarbonate (PC) using a 3D printer (Fortus 350, Stratasys, Eden Prairie, USA).

2.2. Coil circuit

The loop elements were constructed out of 1.3 mm thick tin-coated copper wire. Compared to flat circuit board copper traces, the wire loops reduce eddy current losses in a high-density array coil architecture (Kumar et al., 0000). Implemented small bridges in the conductor enable one loop to cross over another without touching (Keil and Wald, 2013).

Each coil circuit (Fig. 2) consists of a loop with three symmetrically placed ceramic capacitors (Series 11, Voltronics, Danville, NJ), one variable plastic capacitor (GFX2700NM; Sprague Goodman, Westbury, New York, USA), a matching network to the preamplifier (Siemens AG, Healthineers, Erlangen, Germany), and an actively controllable detuning resonant circuit. A typically redundant passive detuning safety mechanism for *in vivo* examinations was omitted for this *ex vivo* coil.

The variable capacitor C_T (3-33 pF) was used to fine-tune the loop resonance to the Larmor frequency at 3T (123.25 MHz). C_2 and C_3 create a capacitive voltage divider. The variable capacitor C_M (3-33 pF, GFX2700NM; Sprague Goodman, Westbury, New York, USA) provides impedance matching of the loop output to a 50 Ω noise matched condition needed by the preamplifier to operate at the lowest noise figure at

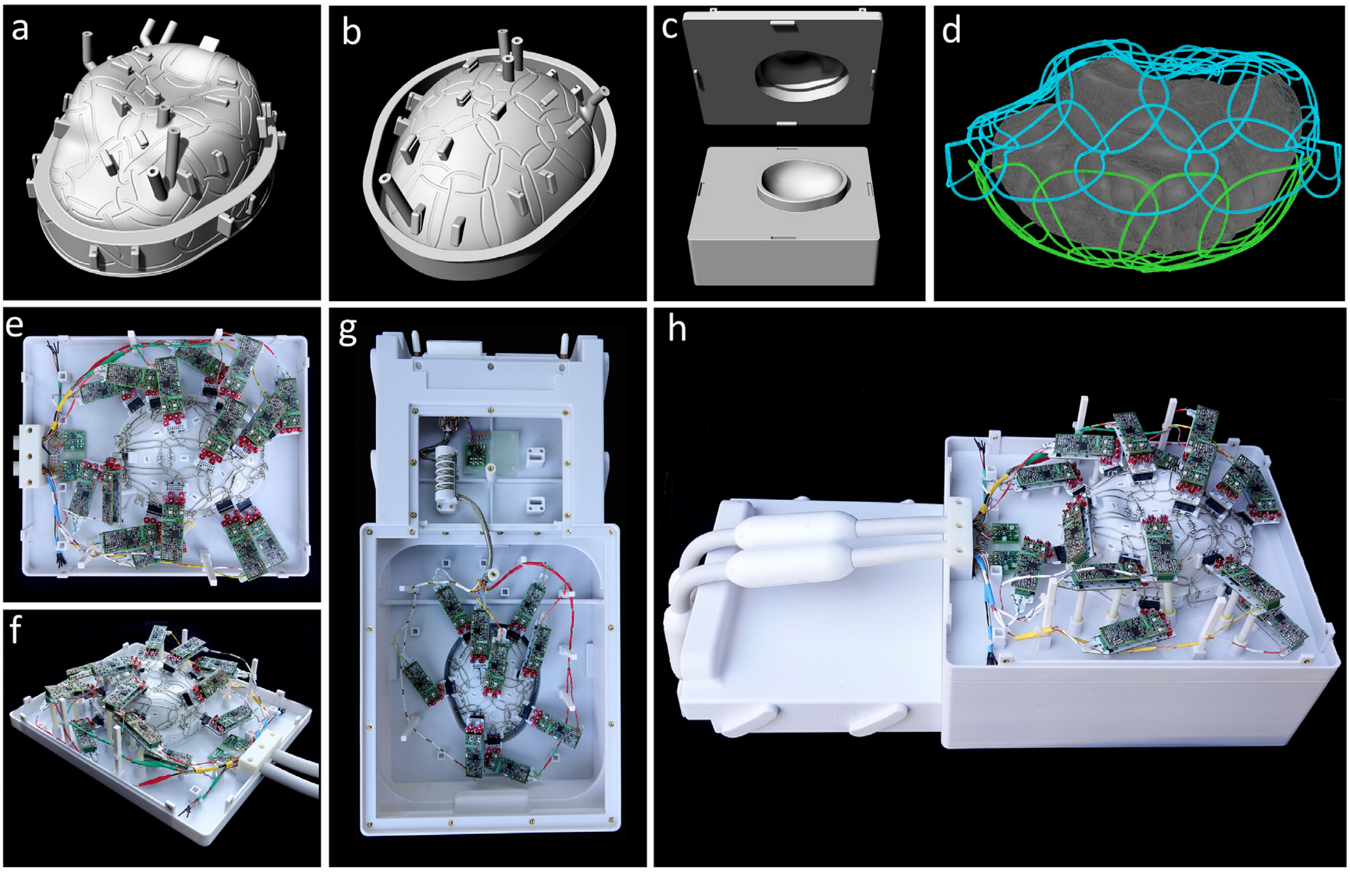

Fig. 1. 48ch *ex vivo* brain coil **(a-c)** Computer aided design model of the coilformer with graved loops and standoffs for preamplifier boards. **(a)** Top coilformer part. **(b)** Bottom coilformer part. **(c)** Inner side of both coilformer parts with overlapping frames to allow geometrical decoupling of the loops from top and bottom part.**(d)** Placement of the 30 top loops (blue) and the 18 bottom loops (green) around the brain (gray). **(e-h)** Completely constructed coil consisting of the top part (e and f) and bottom part (g).

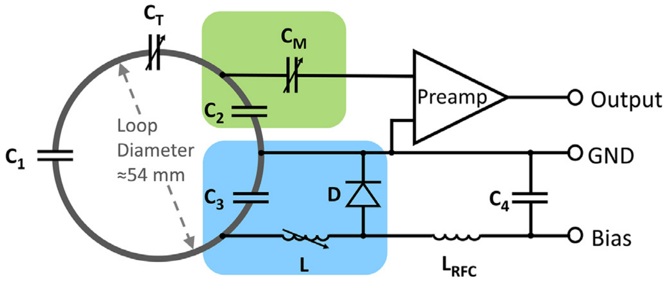

Fig. 2. Circuit schematic for one coil element. Each loop consists of three fixed capacitors (C_1-C_3) and one variable capacitor (C_T). C_T fine-tunes the resonant frequency of the coil to Larmor frequency corresponding at 3T. C_2 and C_3 create a capacitive voltage divider. C_3 is part of the active detuning circuit (blue) together with the variable inductor L and the PIN diode D. C_2 and C_M (green) provide both impedance matching of the loop and impedance transformation to establish preamplifier decoupling. Typical values for the components are: C_1 = 33 pF, C_2 = 56 pF, C_3 = 56 pF, C_4 = 2.2 nF, $C_T \approx 18$ pF, $C_M \approx 18$ pF, $L \approx 24.5$ nH, L_{RFC} = 2.7 μH.

123.25 MHz (Reykowski et al., 1995). To ensure accurate detuning of the loop elements, an active detuning circuit was implemented. It consists of one of the voltage dividing capacitors C_3 and a variable inductor L (Coilcraft Inc., 25-32 nH, 165-02A06L, Cary, IL, USA) in series to a PIN diode D (MA4P4002B-402; Macom, Lowell, MA, USA) (Edelstein et al., 1986). During transmit, a DC current is applied to forward bias the PIN diode. This in turn activates the detuning resonant circuit at the Larmor frequency and generates a high impedance in the loop to suppress current flow. The RF-choke L_{RFC} (Coilcraft Inc, 2.7 μH, 1812CS-333XJLC Cary, IL, USA) and C_4 block the RF signal to prevent passing into bias source.

While nearest neighbors use geometrical decoupling, next-nearest neighbors and further coil elements are decoupled by the impedance transformation of the input of the preamplifiers (Roemer et al., 1990). The capacitors C_2 and C_M and the preamplifier's input impedance form a resonant circuit, which enables a voltage-source measurement setup, where RF current flow is minimized. As a consequence, inductive coupling across elements is highly reduced and all coil elements receive independently, while maintaining a 50 Ω output impedance.

Both the matching and detuning network of the coil element are placed on the preamplifier's daughter board, rather than soldering these components directly to the coil former. Therefore, the daughter board is a part of the coil element. The printed circuit board (PCB) daughter board is connected to the loop with an intermittent pin connector. This setup allows a fast construction process of dense array coils.

According to the RF scanner architecture, pre-amplified signals from two loops elements are multiplexed onto one output coaxial cable. The bundled output cables are passed through cable traps to prevent RF common mode currents on the shield of the coaxial cable (Peterson et al., 2003). The cable traps comprise a wounded coaxial cable bundle, which form an inductance (≈109 nH), and a parallel ceramic high power capacitor (15.2 pF, Series 25, Voltronics, Danville, NJ), which resonates at Larmor frequency. Two traps are incorporated into the cables of the upper array coil segment and one cable trap is located directly in the bottom coil housing part.

2.3. Coil bench measurements

For bench measurements during the construction process, a custom-made coil plug simulator was used. It provides voltage for the preamplifiers (3 V) and the opportunity to apply a DC current (100 mA) to bias manually each PIN diode forward, which allows for active detuning of single coil elements. To gather information about bench level metrics, e.g. transmission and reflection measurements, a vector network analyzer (VNA) (ENA series, Agilent Technologies, Santa Clara, CA) and custom-built RF tools such as single / double probes and sniffer probes were used. These measurements included tuning to Larmor frequency, active detuning, preamplifier decoupling and geometrical nearest neighbor decoupling of each coil element.

The loops were tuned under a S_{21} control with a 50 Ω dummy load plugged into the preamplifier socket, while all other elements of the array were detuned. Active detuning was performed by using S_{21} measurement with the double-probe for each loop, while all other coil elements were detuned and the relevant loop under test was switched between the tuned and detuned state. The difference of both states at the Larmor frequency indicates the magnitude of active detuning. A similar S_{21} double-probe measurement was carried out to determine the effectiveness of the implemented preamplifier decoupling, first by plugging the preamplifier into the socket on the PCB and second by terminating the socket with a load impedance of 50 Ω. Again, all but the loop element to be tested were detuned.

Coupling of nearest neighbor elements was measured with direct S_{21} VNA measurement by using coaxial cables, which were directly plugged into the preamplifier sockets. During this measurement, all other coil elements were detuned. This measurement configuration was also used to verify 50 Ω coil impedance matching using S_{11} and S_{22} measurements (Keil and Wald, 2013; Reykowski et al., 1995).

Furthermore, unloaded-to-loaded coil quality factor ratio (Q_U/Q_L) of one representative coil element was measured within the populated but detuned array assembly, using the S_{21} double-probe method (Hoult, 1978). As a load, a fixed tissue brain sample in periodate-lysine-paraformaldehyde (PLP) solution was used.

2.4. MRI data acquisition and analysis

Imaging metrics were acquired on a clinical 3T MRI scanner (MAGNETOM, Skyra, Tim 4G, Dual Density Signal Transfer, Siemens AG, Healthineers, Erlangen, Germany), equipped with a customized gradient coil (AS302 CONNECTOM 1.0 gradient)[1] with a maximum gradient strength of 300 mT/m and a maximum slew rate of 200 T/m/s.

For evaluating the developed *ex vivo* whole brain array coil, we constructed a human-brain-shaped phantom using a 3D printer (Objet30 Pro, Stratasys, Eden Prairie, USA). The phantom was filled with agarose and dielectrically tuned to match the RF coil's loading condition with the PLP-packed *ex vivo* brain. The corresponding quantities were: 830ml distilled H_2O, 29 g NaCl, 12.5 g of agar powder (Sigma-Aldrich Corp., St. Louis, MO) and 936 g sugar. The matched loading condition was validated via an S_{11} measurement on the VNA's smith chart at Larmor frequency. The dielectric values of the phantom were measured to be $\sigma = 0.49$ S/m and $\epsilon_r = 66.3$ with a VNA equipped with a dielectric probe kit (85070E kit, Agilent Technologies, Santa Clara, CA).

2.4.1. Array coil characterization

For determining SNR and G-factor, the phantom was scanned with a proton density (PD)-weighted FLASH sequence (repetition time (TR)=200 ms, echo time (TE)=4.8 ms, flip angle (F) =15°, matrix (M): 192×192 (SNR) and 64×64 (G-factor and SNR in parallel imaging), field of view (FOV): 256×256 mm^2, slice thickness: 8 mm, bandwidth (BW): 200 Hz/pixel). Information about noise correlation was obtained with the same sequence but without RF excitation. The coil sensitivities for the G-factor calculations were derived from a pre-scan before the actual MRI data acquisition. This scan provided a low-resolution full FOV image of the phantom for each coil element, which was used to estimate the sensitivity profiles of the individual receiver coil.

Pixel-wise SNR maps were calculated using the noise-covariance-weighted, root sum-of-squares image reconstruction method from Kellman and McVeigh (2005). To evaluate the array coil's encoding capability for parallel imaging, SENSE G-factor maps were computed using the acquired noise correlation matrix and complex sensitivities of the coil elements (Pruessmann et al., 1999). The FOV of the G-maps was tightly enclosed to the phantom, in order to enhance the aliasing pattern inside the imaging object.

A valuable metric is the remaining image SNR after the parallel imaging acceleration has been performed. We calculated the remaining SNR by dividing the SNR globally by the square root of the reduction factor R and further locally with the noise amplification given by the G-factor.

For further characterization of the coil performance, we examined the encoding power for simultaneous multislice (SMS) acquisitions with blipped-controlled aliasing in parallel imaging (Feinberg et al., 2010; Larkman et al., 2001; Setsompop et al., 2012). To assess the encoding capability of combined SMS and in-plane acceleration, a reduction factor of $R = 2$ and a slice acceleration factor from $MB = 4$ up to $MB = 8$ with a 1/3 FOV shift were evaluated. Noise correlation and SNR and G-factor maps of the 48ch *ex vivo* brain coil were compared to a customized 64-channel (64ch) whole head receive array coil (Keil et al., 2013) with identical acquisition parameters.

In addition, time course stability of each coil element was measured with a single-shot, gradient-echo, echo planar imaging (EPI) sequence (time points: 500, TR = 1000 ms, TE = 30 ms, F = 90°, M: 64 × 64, FOV: 200 × 200 mm^2, slices: 16 slices of 15 mm, BW: 2298 Hz/pixel) with the brain phantom. This scan was repeated 16 times without pause, resulting in a 2 h stability scan protocol. The average intensity of a 15-pixel square region of interest (ROI) in the phantom center was detrended with linear and quadratic temporal trends and plotted. The stability was calculated as the variation of signal intensity from peak-to-peak as a percentage from the average signal intensity (Weisskoff, 1996).

2.4.2. Ex vivo *brain dMRI*

High-resolution (0.73 mm isotropic) diffusion imaging was performed on a whole *ex vivo* human brain packed with paraformaldehyde-lysine-periodate (PLP) in a tight-fitting, sealed plastic bag. The brain had been excised from a male who had died of non-neurological causes, and had been placed in fixative (10% formaldehyde) for 90 days before being transferred to PLP solution for long-term storage. Diffusion-weighted images were acquired using the same imaging protocol on the 48ch whole brain *ex vivo* coil and 64ch *in vivo* head coil to enable comparisons between the two coils. We used a 3D diffusion-weighted spin-echo segmented EPI sequence (imaging parameters: TR = 500 ms, TE = 65 ms, echo spacing: 1.22 ms, M: 160 × 268 × 208, FOV: 118 × 196 × 152 mm^3, BW: 1244 Hz/pixel, 16 shots, EPI factor = 10, no partial Fourier). A multi-shell sampling scheme was used that included 18 non-collinear diffusion encoding directions with $b = 4000$ s/mm^2 (gradient strength of 91 mT/m, $\delta = 16.1$ ms, $\Delta = 27.6$ ms), and 36 non-collinear diffusion encoding directions with $b = 10000$ s/mm^2 (gradient strength of 133 mT/m, $\delta = 16.1$ ms, $\Delta = 27.6$ ms). A total of 9 $b = 0$ volumes were acquired, interleaved every 6 diffusion-weighted volumes. The total acquisition time for the $b = 4000$ s/mm^2 scan was 10.3 h. The total acquisition time for the $b = 10000$ s/mm^2 scan was 20.6 h. The phase-encoding direction was anterior-posterior when considering the conventional sagittal plane. Since the brain in the constructed coil was rotated compared to the usual orientation of a patient, the anatomical axis of the phase-encoding direction was inferior-superior.

The image acquisition parameters were chosen so as to maximize SNR while avoiding prohibitively long scan times. The use of a 3D read-

---

[1] under development and not commercially available in the U.S. and its future availability cannot be assured.

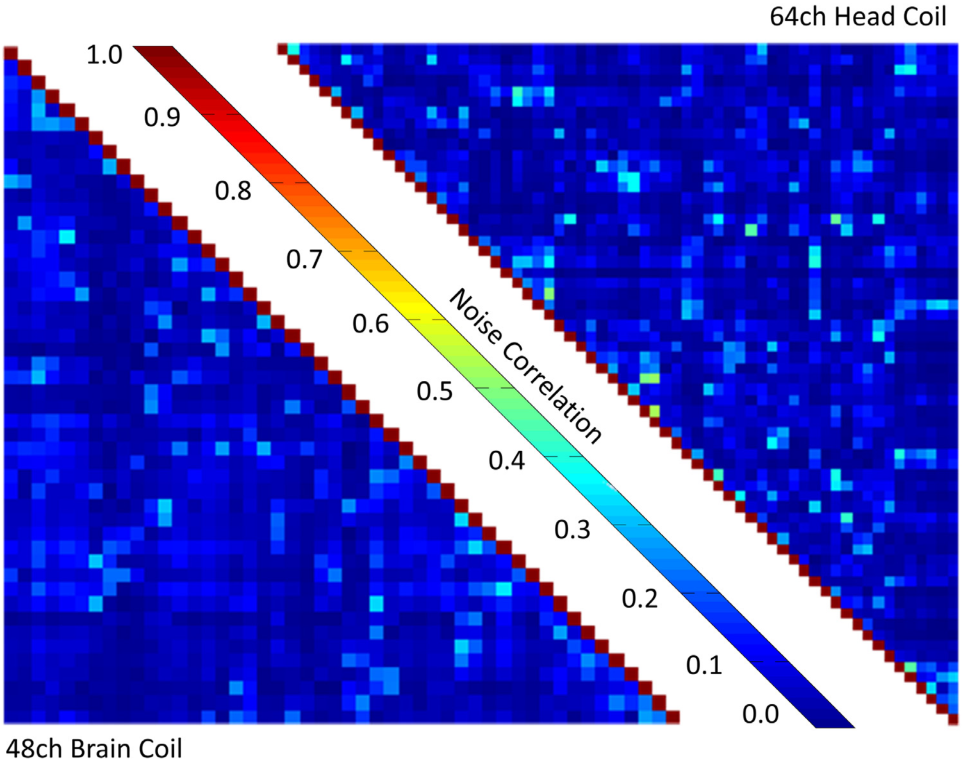

Fig. 3. Noise correlation matrix of the 48ch *ex vivo* brain coil and the 64ch *in vivo* head coil with the scale normalized to 1.

out with excitation of the entire imaging volume per TR enabled the use of a relatively short TR of 500 ms while preserving SNR efficiency (Miller et al., 0000). Due to the reduction of T_1 and T_2 values in fixed human brain tissue (340 ms and 45 ms, respectively (McNab et al., 2009)) compared to *in vivo* values, a relatively short TE of 65 ms was chosen to preserve SNR. To achieve the TE and *b*-values used here, the maximum gradient strength was calculated to be on the order of 90-130 mT/m based on the sequence design, which seeks to maximize gradient strength while keeping the diffusion time Δ as short as possible.

Diffusion-weighted volumes were corrected for eddy current distortions with the *eddy* tool from FSL (Andersson and Sotiropoulos, 2016). The multi-shot acquisition mitigated EPI distortions and thus no further distortion correction was performed prior to image analysis. We performed a diffusion tensor imaging (DTI) analysis (Basser, 1995) on the images from the lower shell, and a diffusion kurtosis imaging (DKI) analysis (Jensen et al., 2005) on the images from both shells. Finally, the full data set was used to fit a fiber orientation distribution (FOD) at each voxel with multi-shell, multi-tissue, constrained, spherical deconvolution (MSMT-CSD) (Dhollander et al., Montreal, 2019). Probabilistic tractography was then performed on these FODs (Tournier et al., Stockholm, 2010), with a minimum FOD amplitude of 0.2, a maximum bending angle of 45 degrees, and a minimum streamline length of 20. We seeded at every voxel in a white-matter mask, which we extracted by thresholding the average of the diffusion-weighted volumes to remove the PLP background.

3. Results

3.1. Coil bench measurements

The Q_U/Q_L-ratio of a 54 mm loop element was measured to be 233/46=5.1 with six surrounding but non-resonant neighboring loops. Thus, the array's loop elements operate in the sample noise dominated regime. The geometrical decoupling of nearest neighbors was S_{21} measured with an average value of -16 dB and ranged from -14 dB to -18 dB. Non-adjacent and thus non-overlapping coil elements, which are primarily decoupled via preamplifier decoupling, obtained an average decoupling value of -18 dB with a range from -17 dB to -19 dB. The isolation between tuned and detuned states caused by the active detuning circuit reached an average value of 42 dB.

3.2. Image performance

Time course stability tests show a peak-to-peak variation of 0.36% over 8.000 time-points EPI sequence measured in a ROI comprising 15×15 pixels.

3.2.1. Signal-to-noise-ratio in unaccelerated images

Fig. 3 shows the noise correlation matrix of the 48ch *ex vivo* coil and that of the 64ch *in vivo* coil. The *ex vivo* array has a range of noise correlations from 0.02% to 35.8% with an average value of 7.5%, while the *in vivo* array has noise correlations from 0.12% to 53.8% with an average value of 7.1% for the off-diagonal elements.

Fig. 4 compares the SNR maps from the newly developed 48ch *ex vivo* brain coil to that of the existing, custom 64ch whole head coil, in different planes of the agar phantom. For both coils, the measured SNR is highest in the outer periphery and decreases towards the center. The SNR gain of the newly constructed 48ch array coil reaches over the whole brain volume. It outperforms the larger 64ch *in vivo* head coil by a factor of 2.5, when the average SNR over the whole brain phantom is considered. The highest gain is found in the periphery of the phantom, especially in the regions where the 48ch brain coil has a substantially closer proximity to the sample. In the periphery and in the center of the phantom, a 2.9-fold and 1.3-fold SNR gain was measured, respectively.

Examples of SNR profiles can be found in Fig. 5. In all three slices, the SNR of the 48ch *ex vivo* brain coil exceeds that of the 64ch *in vivo* head coil over the entire profile.

3.2.2. Signal-to-noise-ratio and G-factor in parallel imaging

Fig. 6 shows the SENSE inverse G-factor maps in a representative coronal plane of the brain phantom for both one-dimensional and two-dimensional acceleration obtained from the 48ch *ex vivo* brain coil and

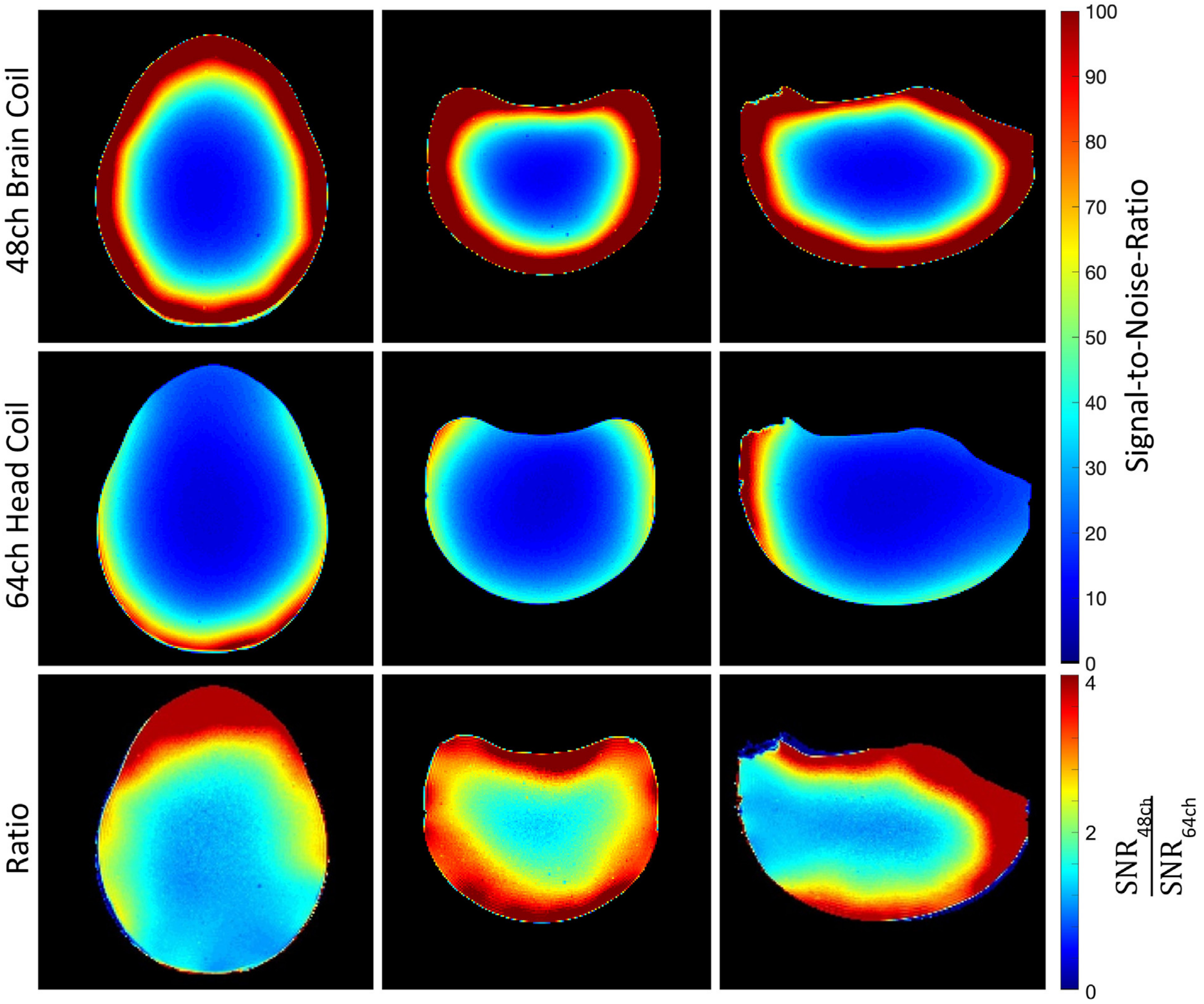

Fig. 4. Comparison of the SNR, normalized to 100, of a transverse (left), coronal (middle) and sagittal (right) slice of the brain phantom with the 48ch *ex vivo* brain coil (top row), the 64ch head coil (middle row) and ratio maps between the two coils (bottom row). The 48ch *ex vivo* brain coil shows a 1.3-fold SNR gain in the center and a 2.9-fold SNR improvement in the peripheral regions when compared to the 64ch head coil.

the 64ch *in vivo* head coil. The newly constructed 48ch coil provides significant improvement compared to the 64ch head coil for both in-plane acceleration types. Both coils show minimal noise amplifications for acceleration factors of $R = 2$, $R = 3$ and $R = 2{\times}2$. However, for higher accelerations ($R>3$) the 48ch *ex vivo* coil provides favorable encoding capabilities when compared to the 64ch *in vivo* head coil. At $R = 4$, the 48ch coil shows on average a 16% lower G-factor than the 64ch head coil. When comparing the peak G-factors between both, the 48ch coil shows a 21% improvement. The enhanced encoding power of the 48ch coil becomes even more apparent when very high acceleration factors are compared. The improved average and peak G-factor for $R = 7$ was measured to be 35% and 41% lower. At $R = 5{\times}5$ the noise amplifications could be reduced on average by 43%, while the peak G-factor decreased by 53%.

A more meaningful figure of merit is the SNR obtained from the accelerated image, where both the under-sampled k-space trajectory and the local noise amplification were taken into account. Fig. 7 illustrates the accelerated SNR for both coils using box plots. Since the constructed 48ch coil provides both a higher baseline SNR and lower G-factors, it highly outperforms the 64ch head coil across all acceleration scenarios. The average SNR from the 64ch coil only reaches the lower 25th percentile of the 48ch *ex vivo* coil. Further, it should be noted that the relative gain in average SNR increases with higher acceleration factors (*e.g.,* factor 2.4 for $R = 2$ and 3.9 for $R = 7$) for both one-dimensional and two-dimensional acceleration. For a direct comparison between 1D and 2D accelerations, when the reduction factor R was matched (R_{1D}=4 and R_{2D}=2×2=4), the average SNR of the 48ch ex-vivo coil was measured to be 600 and 657, respectively. For the 64ch head coil, these numbers were 210 and 268, respectively. Thus, both coils showed overall less noise amplification in the 2D-acceleration scheme.

3.2.3. Signal-to-noise-ratio and G-factor in simultaneous multislice imaging imaging

Fig. 8 compares the inverse G-factor maps for the SMS image reconstruction technique from a coronal slice of the brain phantom. Compared to the 64ch head coil, the constructed 48ch coil indicates overall substantially lower noise amplification for the SMS examination, as well as for combined SMS and in-plane acceleration. At a multiband factor of $MB = 4$, the 48ch coil generates negligible noise amplifications (g_{mean}=1.0002 and g_{max}=1.0569), while the 64ch head coil shows substantial noise gains of g_{mean}=1.1218 and g_{max}=1.6345. Furthermore, the dedicated 48ch *ex vivo* brain coil achieves similar to slightly better encoding capabilities at $MB = 8$ as the 64ch head coil at $MB = 4$ ($g_{mean48ch}$=1.0047 *vs.* $g_{mean64ch}$=1.1317 and $g_{max48ch}$=1.2913 *vs.* $g_{max64ch}$=1.2913). Therefore, the 48ch coil allows the application of a slice acceleration factor of $MB = 8$ with negligible noise gain.

To assess the accelerated SNR during SMS acquisitions, Fourier averaging needs to be taken into account: In the case of the $MB = 8$ ac-

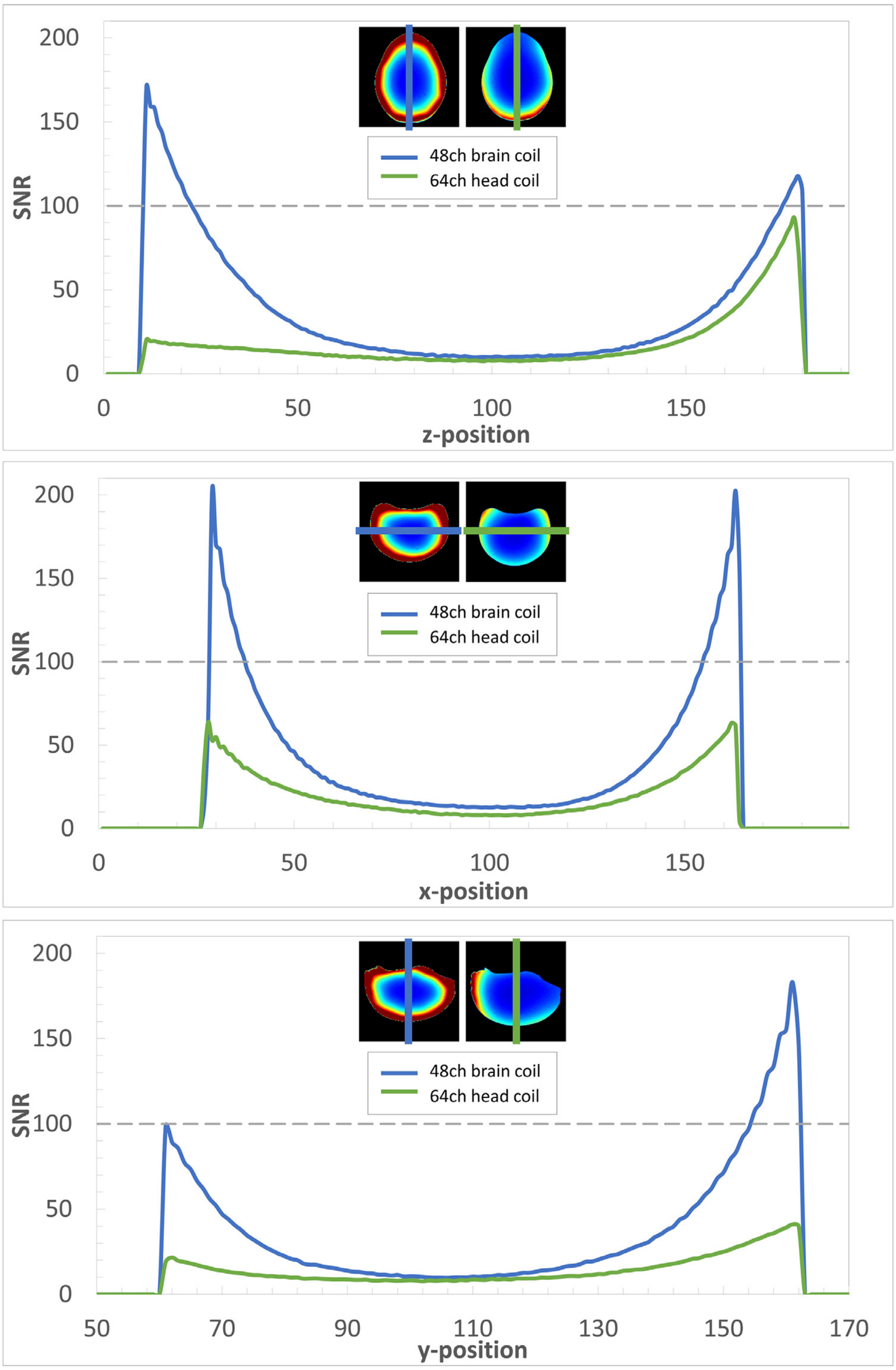

Fig. 5. SNR profiles of the 48ch *ex vivo* brain coil (blue) and the 64ch *in vivo* head coil (green) through the center of a transverse (top), a coronal (middle), and a saggital (bottom) slice. The dedicated 48ch *ex vivo* coil shows substantial SNR gains at the periphery in the brain phantom. Due to the close-fitting coil array with omnidirectional signal reception, even SNR improvements at the center of the brain phantom of ≈30% are feasible.

celeration, eight times more ^{1}H spins are simultaneously excited compared with a single-slice acquisition. Thus, for a multiband factor *MB*, the SNR efficiency can be improved up to a factor of $\sqrt{MB}$, if the imaging parameters between the non-accelerated and the SMS-accelerated case remain identical. Under these constant circumstances, the Fourier averaging translates to an SNR increase by a factor of up to $\sqrt{8}/g_{\text{max-48}} = 2.2$, when compared to a commonly used consecutive single-slice acquisition schemes. The $MB = 8$ achievable SNR obtained from the 64ch is only increased by a factor of up to $\sqrt{8}/g_{\text{max-64}} = 1.2$. In direct comparison, when the baseline SNR, Fourier averaging, and G-factors are taken into account, the 48ch coil achieves up to a 4.5-fold SNR improvement at $MB = 8$ compared to the 64ch head coil.

3.2.4. *Diffusion imaging in* ex vivo *brain*

Fig. 9 shows various maps obtained from the multi-shell dMRI scan of a *post mortem* human brain, acquired at 0.73 mm isotropic resolution with the 48ch *ex vivo* brain coil. The six columns show: *(i)* a $b = 0$ image, *(ii)* a diffusion-weighted image from the lower shell (b = 4000 s/mm^2), *(iii)* the fractional anisotropy (FA) map, *(iv)* the FA map color encoded

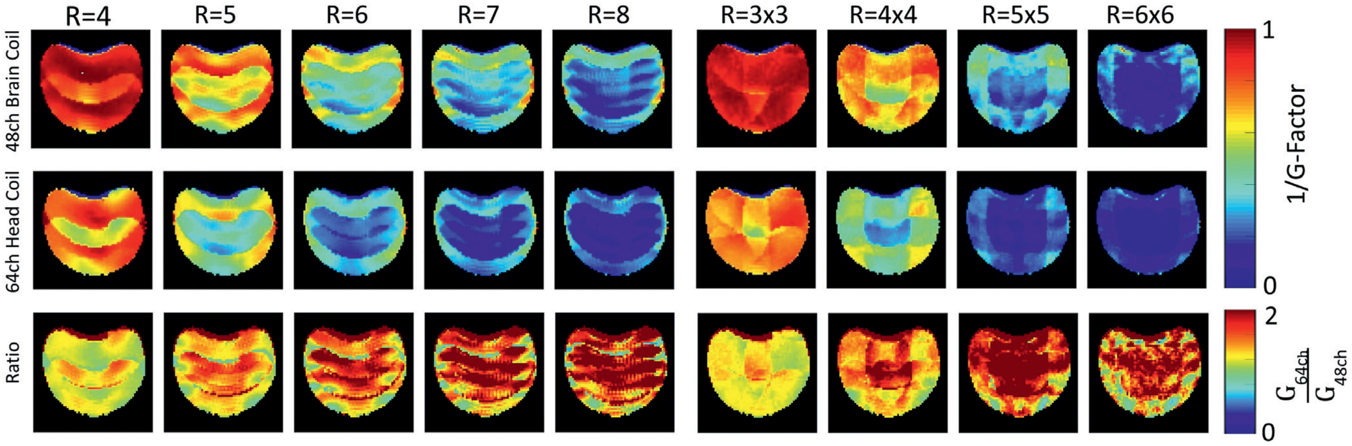

Fig. 6. Comparison of inverse phantom G-factor maps between the 48ch *ex vivo* brain coil (top row) and the 64ch head coil (middle row) for different acceleration factors (R) obtained from a representative coronal slice. The bottom row shows the ratio maps of the inverse G-factors obtained from both coils. The G-Factors from the 48ch *ex vivo* brain coil show overall lower noise amplification, when compared to the 64ch head coil.

by the principal eigenvector of the diffusion tensor, *(v)* a diffusion-weighted image from the higher shell (b = 10000 s/mm^2, and *(vi)* the mean kurtosis map.

For each map in the figure, an axial view is shown in row (a) and a coronal or sagittal view is shown in row (c). Row (b) shows magnified regions of interest that highlight fine anatomical detail in the striatum (red box, columns i-ii and iv-v) or in the basal ganglia and thalamus (green box, columns iii and vi). Note that the exquisite mean kurtosis contrast allows a clear delineation of internal structures such as the putamen, caudate nucleus, internal and external global palidus, and thalamus. Row (d) shows a magnified coronal view of the primary motor cortex (blue box, columns i-ii and iv-v), highlighting the presence of radial fibers, and a magnified sagittal view of the hippocampus (yellow box, columns iii and vi). These maps illustrate that, by combining the high gradient strengths available on the 3 T Connectome scanner with the high sensitivity of our *ex vivo* coil, we can collect dMRI data with high spatial resolution and high SNR, and map detailed gray and white matter anatomy, both in deep brain and near the cortical surface.

Fig. 10 compares the FODs and probabilistic tractography obtained from the multi-shell dMRI data collected with the 48ch *ex vivo* brain array and the 64ch *in vivo* head array. The higher SNR achieved by the newly developed *ex vivo* coil, in both superficial and deep brain areas, yielded less noisy FODs that better captured the course of the underlying fiber bundles. This resulted in higher-quality tractography. For example, the tractogram from the 48ch brain array data included fuller bundles of trans-callosal streamlines, as well as subcortical U-shaped streamlines. The lower SNR of the 64ch head coil led to more spurious peaks in the FODs, which had a negative impact on the ability of tactography to reconstruct these bundles.

4. Discussion

We designed, constructed, and evaluated a 48ch *ex vivo* brain array receive coil for high-resolution and high b-value dMRI of a whole *ex vivo* human brain on the 3 T Connectome scanner (McNab et al., 2013; Setsompop et al., 2013). The coil was characterized by both bench tests and image metrics. Bench tests included element measurements of the coil quality factor Q, active detuning, geometrical decoupling, and preamplifier decoupling. MRI evaluations included measurements of the noise correlation, pixel-wise SNR, and G-factor, as well as time course stability using a brain shaped agar phantom. We demonstrated the coil's performance in achieving high SNR with the acquisition of multi-shell 0.73 mm isotropic resolution diffusion-weighted MR images of a whole *ex vivo* brain.

4.1. Array coil characterization

In many applications, large channel count arrays with relatively small loop sizes such as the 54 mm loops used here are necessary to increase both reception sensitivity and encoding power. However, very small loop elements quickly lose their sample noise dominance. Under these circumstances, small elements do not translate to higher SNR acquisitions anymore. For *in vivo* imaging at 3T, this critical size is reached at about 60 mm diameter (Keil et al., 2011). In *ex vivo* brain imaging, however, loop sizes can be made substantially smaller than for *in vivo* imaging. This is attributed to the brain fixation medium, which has a higher conductivity compared to *in vivo* tissue and thus provides a higher fraction of sample noise. While the noise increases in the *ex vivo* sample, the electronic noise can be decreased by omitting *in vivo* human safety features in the coil element circuitry, such as passive detuning and RF-fuses. This condition results in an enhanced Q_U/Q_L-ratio when using small receiver elements. Therefore, the implemented loop size of ≈54 mm provides a relatively high Q_U/Q_L-ratio of 5.1, outperforming most coils optimized for *in vivo* applications with loop diameters ranging from 50 mm to 65 mm from our previous studies (Janssens et al., 2012; Keil et al., 2011; 2013). As a consequence, the minimum loop diameter at which sample noise dominance is maintained decreases for imaging fixed tissue brain samples in PLP solution, allowing us to contemplate very high-density arrays for *ex vivo* sample examinations.

Despite RF electrical optimizations, the mechanical coil former is an important and critical design aspect for *ex vivo* imaging. To improve SNR, the loops were populated very close to the sample, maximizing signal reception. Thus, the completely brain-enclosing coil former with uniformly distributed loop elements guarantees nearly omni-directional signal reception from the sample (decreased sensitivity was observed with some loops aligned to be almost parallel to the magnetic field B_0). However, an entirely surrounding coil array requires a split housing mechanism, which disturbs the loop layout and makes it difficult to maintain geometric decoupling at the split housing edge. Therefore, an overlapping edge structure was implemented, enabling adjacent loop elements to be geometrically decoupled across the two housing segments, while the overall array coil structure remains self-contained.

In array coil design, the central ultimate SNR is already approached with only 12 surrounding coil elements at 3 T (Wiesinger et al., 2005). Implementing higher loop element counts only yields SNR improvements at the periphery for a given geometry. Nevertheless, relative central SNR gains are achievable with tightly fitting array coils. Due to the lack of dedicated *ex vivo* receiver arrays, *in vivo* head coils are commonly used in many *ex vivo* brain studies (Iglesias et al., 2018; McNab et al.,

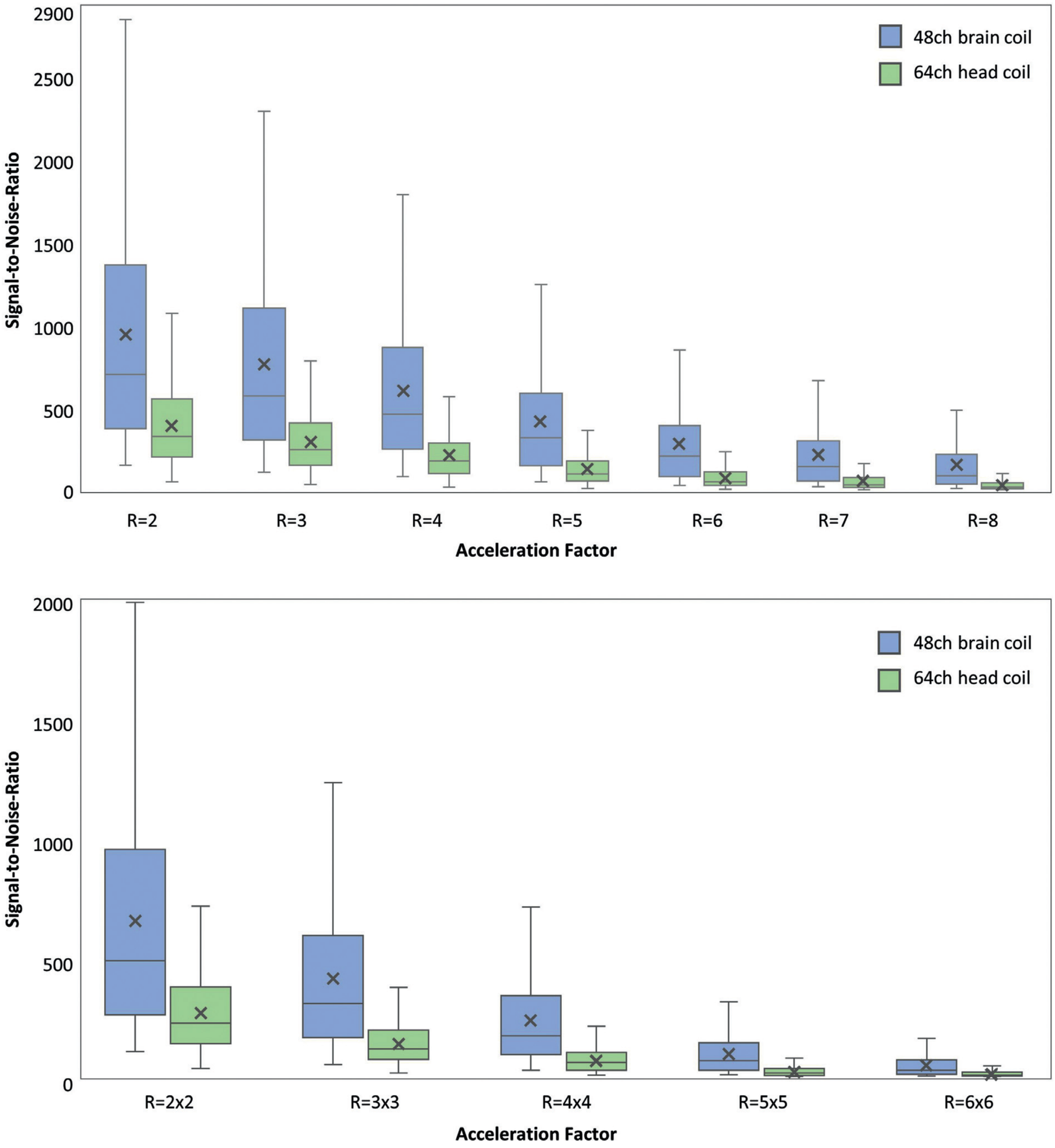

Fig. 7. Parallel imaging accelerated SNR as a function of acceleration factor (*R*) from the 48ch brain coil and the 64ch head coil for one-dimensional (top) and two-dimensional (bottom) accelerations. The box plots represent median (horizontal line), average (cross mark) lower/upper quartiles and minimum-maximum range (whiskers) without outliners. The constructed 48ch coil shows higher accelerated SNR in the entire range of acceleration factors.

2009; Shatil et al., 2016; 2018). However, these coils are not well suited in terms of sample fitting and SNR performance. Optimizing both the mechanical features for close fitting of samples and the RF circuitry can thus result in significant SNR gains in the brain. This implementation provides a 30% SNR increase of the 48ch coil at the phantom center when compared to the larger 64ch head coil. In addition, in the peripheral regions of the brain phantom, the tight-fitting form factor also provides favorable SNR gains, as evidenced by an almost 3-fold SNR improvement over the 64ch coil. The high SNR can be exploited to reduce the voxel size, enabling high spatial resolution MR imaging of a whole *ex vivo* brain.

The average noise correlation of 9% indicates a well decoupled array and highly independent operating receiver loops. Adjacent loops show much higher coupling values up to 36%, which can be attributed to insufficient overlap, resulting in a remaining mutual inductance and shared resistance especially in the sample voxels beneath the overlapping loop regions.

The constructed 48ch *ex vivo* brain coil shows remarkably better encoding performance when compared to the 64ch head coil. The encoding power of the 48ch coil enables approximately one additional acceleration unit, for both one-dimensional and two-dimensional accelerations, with the same noise amplification as the 64ch head coil. Improvements in G-factors are usually achieved by implementing higher channel counts on a given geometry. However, when comparing array coil formers of different sizes, similar improvements in G-factors can be achieved by (1) reducing the diameter of the coil elements at constant

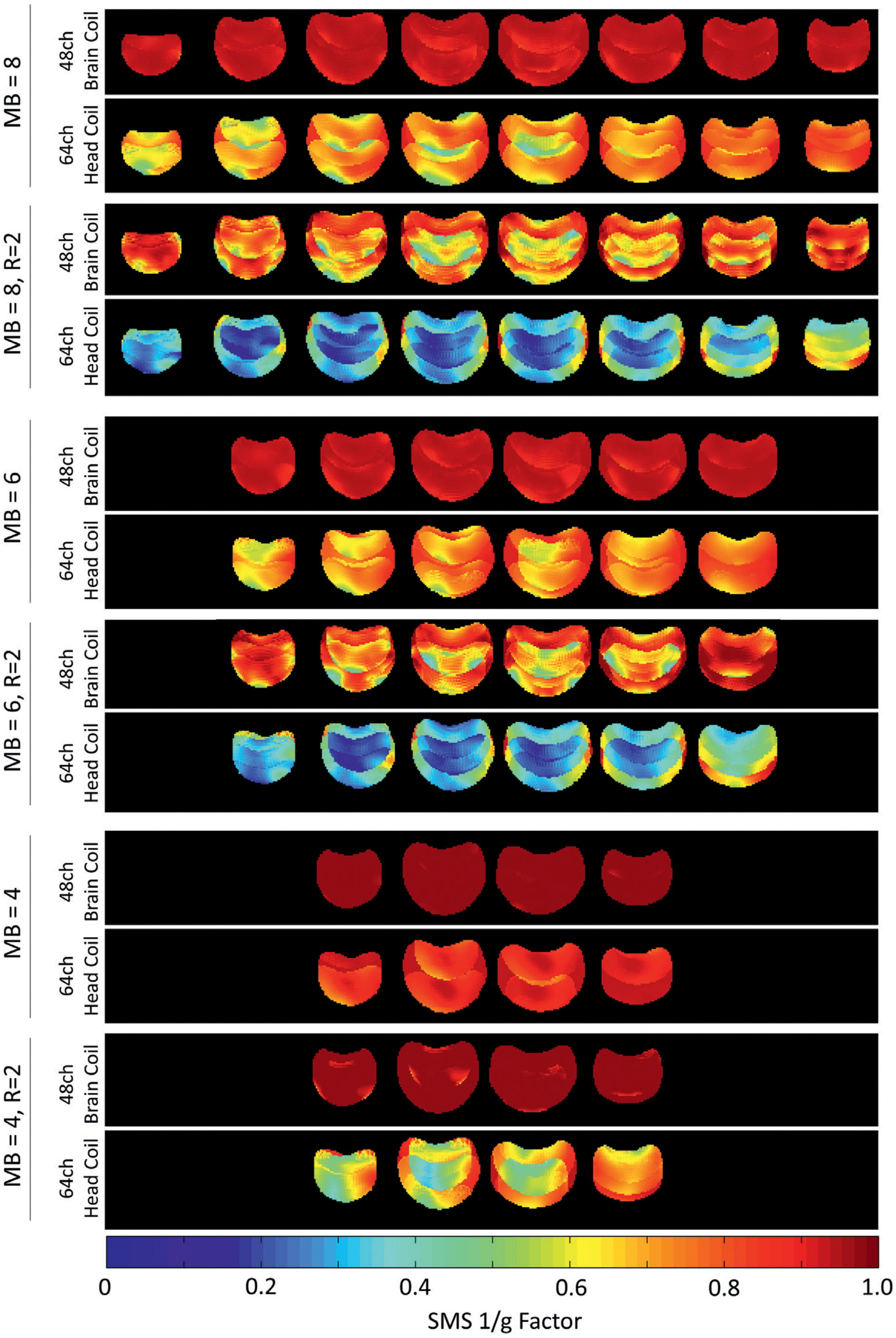

Fig. 8. Comparison of inverse G-factor maps of the brain phantom for accelerated imaging with SMS technique. The 48ch brain coil shows overall considerable lower noise amplification in comparison to the 64ch head coil.

or even lower channel counts, and (2) positioning the coil elements in close proximity to the sample. The tight-fitting, smaller loop elements of the constructed 48ch coil provide an overall stronger spatial modulation in the signal sensitivity's magnitude and phase. Consequently, this coil arrangement allows favorable encoding capabilities for unaliasing folded images (SENSE method) or synthesizing spatial harmonics (GRAPPA or SMASH methods). Additionally, the entirely enclosed *ex vivo* coil former of the 48ch coil leads to better spatial coverage for the aliased pixels when compared to a head array coil, which obviously has limited coverage along the inferior aspect and in the area covering the face.

When the total acceleration factor R is the product of the acceleration factors from two individual orthogonal phase-encoding directions, the images show less amplified noise in comparison to R-fold 1D accelerations. This can be attributed to the embedded sensitivity variations of the array coil being efficiently exploited in two spatial dimensions, allowing overall more favorable encoding capabilities in the image reconstruction.

Reducing scan time using parallel imaging techniques is not strictly essential when constraints on acquisition time are lifted for *ex vivo* examinations. On the other hand, 2D acquisitions are still often used despite their SNR inefficiency per unit time (Eichner et al., 2020; Miller

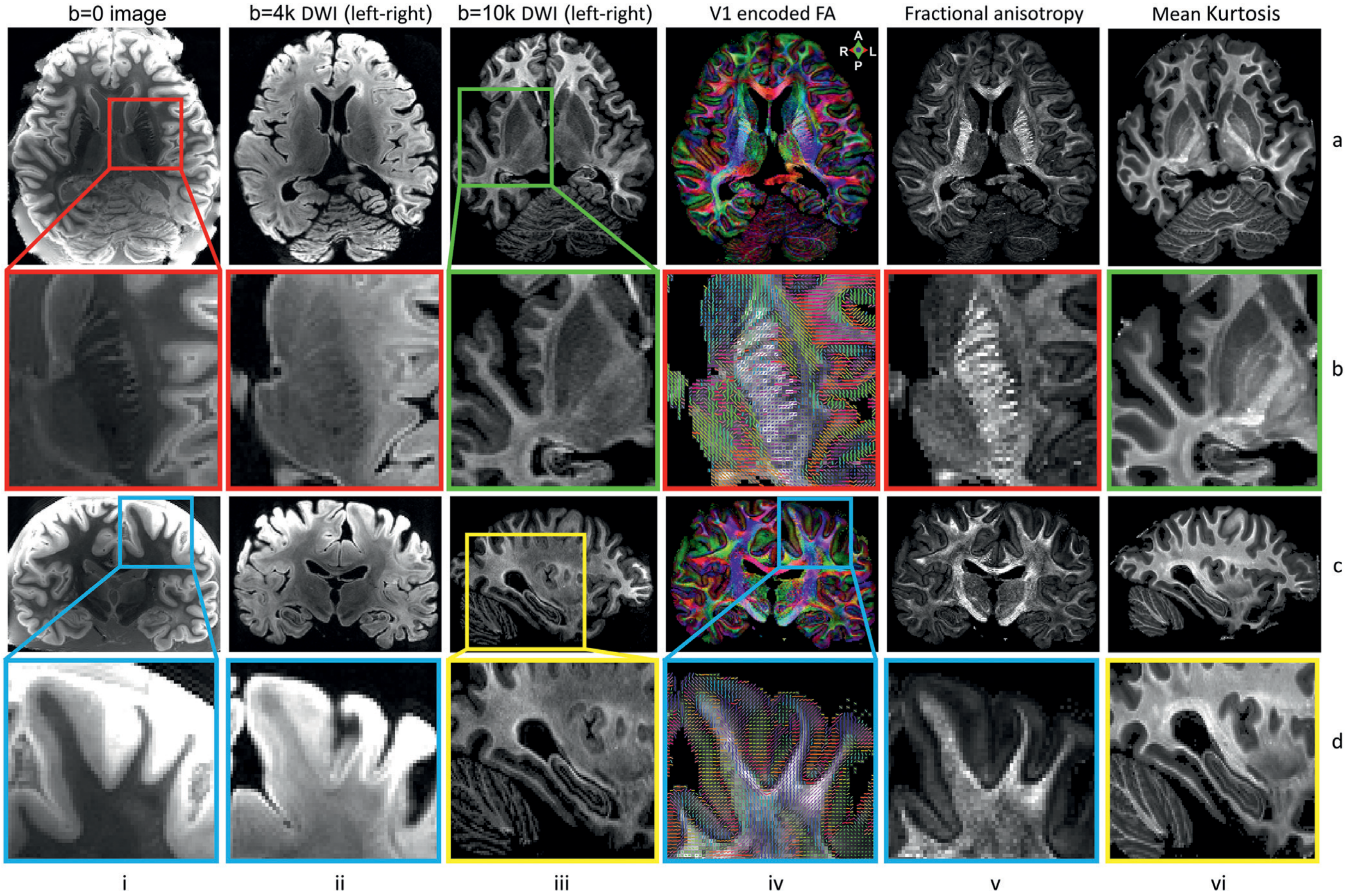

Fig. 9. High-resolution DTI and DKI results at 0.73 mm isotropic resolution with $b = 0$ images (column i), diffusion-weighted images (DWI) acquired at $b = 4000$ s/mm^2 along left-right diffusion-encoding direction (column ii), diffusion-weighted images (DWI) acquired at $b = 10000$ s/mm^2 along left-right diffusion-encoding direction (column iii), fractional anisotropy (FA) maps color encoded by the primary eigenvectors (V1) from DTI (column iv), FA maps (column v) and mean kurtosis maps (column vi). Row (a) shows axial views of each map. Row (b) shows enlarged regions of interest in the internal capsule (red box) and basal ganglia (green box). Row (c) shows coronal or sagittal views for each map. Row (d) shows enlarged regions of interest in subcortical white matter (blue box) and hippocampus (yellow box). The images highlight the fine-scale gray and white matter anatomy captured by the data, both in deep and superficial brain areas.

et al., 2011). For example, mapping tissue microstructural features throughout the whole human brain involves measurements at multiple b-values (Huang et al., 2020), and protocol optimization may be facilitated by 2D scans acquired at resolutions on the order of 0.8 to 1 mm isotropic. For such 2D acquisitions, slice acceleration enables the excitation and measurement of multiple slices (Feinberg et al., 2010; Setsompop et al., 2018; 2012). Unlike conventional parallel imaging, which requires under-sampled data acquisition, these techniques provide acceleration by exciting the spins in multiple slices at the same time using multi-band radiofrequency pulses. These newer multi-band MR acquisitions have the SNR advantages of 3D sampling based on Fourier averaging (Larkman et al., 2001; Setsompop et al., 2012). Therefore, SNR efficiency can be improved by up to a factor of $\sqrt{MB}$, if the imaging parameters remain the same. In practice, however, the SNR gain is reduced locally by the SMS G-factor of the coil and globally due to changes in the sequence parameters. At higher SMS acceleration factors, shorter repetition times are employed, which deceases the level of steady-state longitudinal magnetization. Therefore, the optimal SMS acceleration factor for an MRI study is a trade-off between the benefits of the simultaneously acquired volume and the negative impact from local noise amplifications and the chosen repetition times.

The SNR recovery achieved by the SMS method is highly advantageous for dMRI, which normally suffers from low signal strength. Therefore, it is advantageous for *ex vivo* array coils to provide a high encoding capability for SMS in order to accommodate modern acquisition techniques. Commonly used *in vivo* head coils do not optimally fulfill this requirement for SMS *ex vivo* scans, as they lack enough elements in the z-direction. The radially surrounding, z-directional, stacked elements of the constructed coil provide favorable spatial coverage for SMS image encoding, allowing the separation of multiple collapsed slices. In the case of an $MB = 8$ acceleration scheme, the combination of the enhanced SMS encoding power and the increased baseline SNR of the 48ch coil, would provide an up to 4.5-fold SNR improvement when compared to the 64ch head coil.

4.2. *Diffusion imaging in* ex vivo *brain*

Previous work comparing *ex vivo* dMRI to optical imaging suggests that high spatial resolution (1 mm or higher) improves the accuracy of dMRI-derived axonal orientation estimates, and may have a greater impact than high angular resolution or ultra-high b-values (Jones et al., 2020). While dMRI acquisitions with sub-mm resolution have been feasible in pre-clinical scanners, for smaller samples, they have remained a challenge for whole human brains. The 48ch *ex vivo* brain coil that we have developed here has enabled us to collect high-resolution (0.73 mm isotropic) dMRI data from a whole *ex vivo* human brain. We have shown that this coil achieves higher SNR than a 64ch *in vivo* head coil throughout the brain, leading to improved delineation of brain circuitry with dMRI tractography. The 48ch brain coil exhibits the highest SNR gains in the peripheral area of the imaged sample, which will be of particular utility for imaging fiber architecture in the cortex with high precision. Examples of this in our results are the radial fibers in the

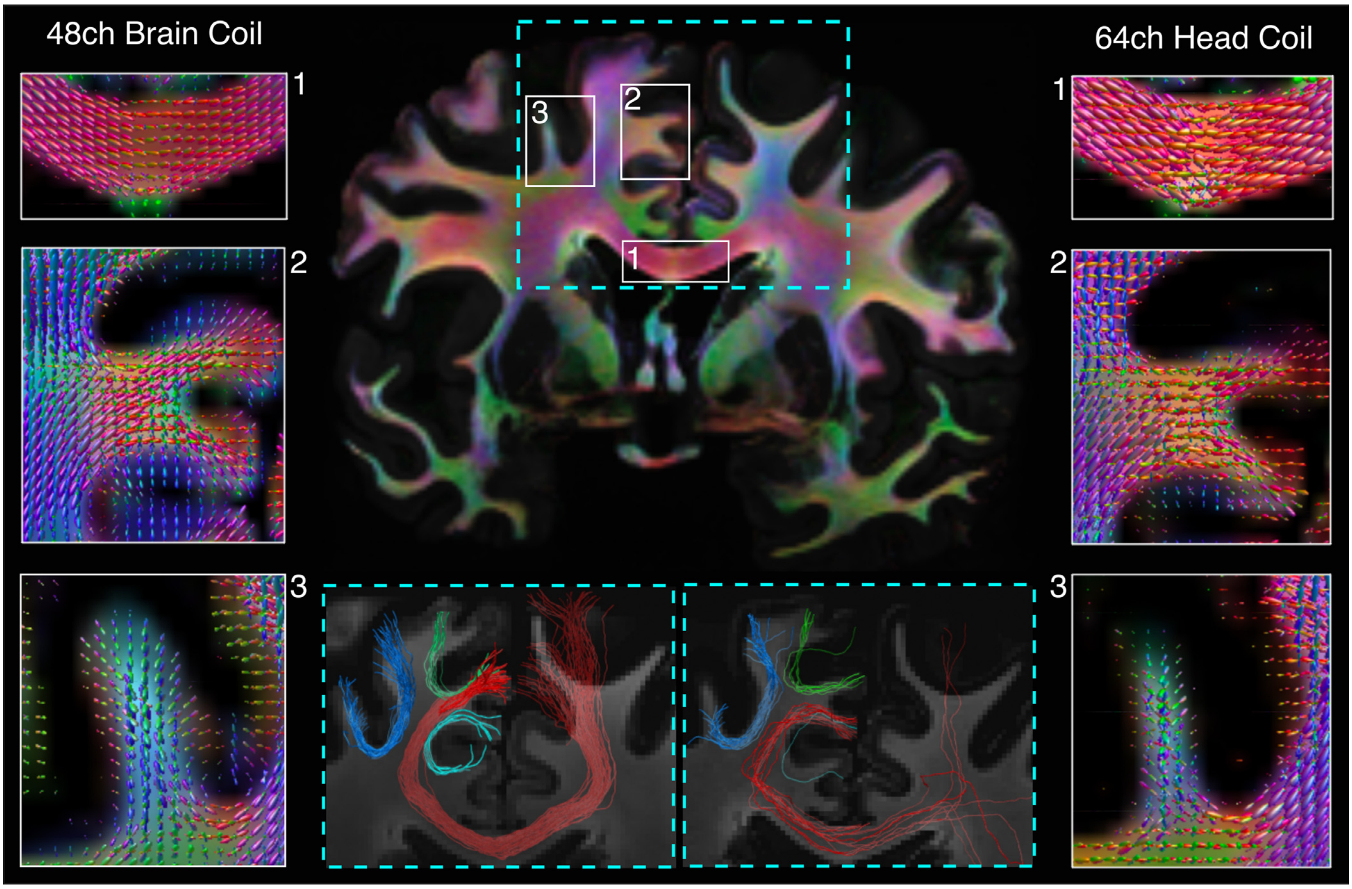

Fig. 10. Comparison of FODs and probabilistic tractography in the same *ex vivo* human brain, between data acquired with the 48ch *ex vivo* brain coil and the 64ch head coil. A whole-brain, coronal color map of the principal diffusion directions as obtained by CSD illustrates the location of the selected regions of interest. For the three smaller boxes in the corpus callosum (1), superior frontal gyrus (2), and middle frontal gyrus (3), we compare FODs obtained with the 48ch *ex vivo* brain coil (left) and the 64ch head coil (right). For the larger box centered over the corpus callosum (outlined in blue dashed lines), we show tractography results obtained with the two coils (see blue dashed insets at the bottom of the figure). We show tractography streamlines from the corpus callosum (in red) and adjacent U-fibers (blue, light blue, green). The higher SNR achieved by the 48ch *ex vivo* brain coil resulted in less noisy FODs, which in turn improved the quality of tractography in these bundles.

primary motor cortex in Fig. 9 (column iv, row d), as well as the subcortical U-shaped tracts in Fig. 10. Future work in laminar microstructure in the cortex will greatly benefit from this coil. The high sensitivity of the coil enables high spatial resolution in combination with very high b-values, as we have shown with our preliminary results at $b = 10000$ s/mm^2. Indeed, mean kurtosis maps obtained from the acquired data reveal exquisite contrast that captures the internal structure of the basal ganglia and hippocampus.

The coil presented here paves the way for sub-mm resolution *ex vivo* dMRI on whole human brains at the high *b*-values accessible on the 3 T Connectome scanner. This capability will allow us to map the connectional anatomy and microstructure of the human brain at unprecedented resolutions, as well as provide reference data for evaluating *in vivo* dMRI scans to gain deeper insight into human brain structure at multiple scales. Currently, 3D EPI suffers from ghosting artifacts when both spatial resolution and gradient amplitude are increased up to the limit of the Connectome scanner's capacity. In future work, we will address this issue by combining appropriate *k*-space reconstruction techniques (Ramos-Llorden et al., 2021) and the use of an additional field monitoring camera system (Mahmutovic et al., 2021). We expect this novel coil design, in combination with the current 3 T Connectome scanner equipped with 300 mT/m gradient strengths and next-generation gradient system planned for the Connectome 2.0 project (Yendiki et al., 2020), to advance our understanding of human brain circuitry in health and disease.

5. Conclusion

A 48ch close-fitting receive array coil for dMRI of whole *ex vivo* human brains at 3 T was designed, constructed, and tested with a brain-shaped phantom and an *ex vivo* brain. We characterized the coil with unloaded-to-loaded *Q*-ratio, noise correlation, SNR, G-factor, SMS G-factor and stability measurements in comparison to a 64ch whole-head *in vivo* coil. Compared to *in vivo* array coils, smaller loop sizes can be used for *ex vivo* brain samples due to increased loading characteristics of the fixed brain tissue. This allows the design of high-channel count arrays, improving both peripheral SNR and encoding performance for accelerated imaging. Due to the high SNR and parallelism, the designed coil is well-suited for high-resolution, high *b*-value *ex vivo* dMRI acquisitions and will enable to map the connectomics and microstructure of the human brain at multiple scales.

Credit authorship contribution statement

Alina Scholz: Conceptualization, Methodology, Software, Validation, Formal analysis, Investigation, Writing - original draft, Writing - review & editing, Visualization. **Robin Etzel:** Methodology, Formal analysis. **Markus W. May:** Methodology, Data curation. **Mirsad Mahmutovic:** Methodology, Software, Validation. **Qiyuan Tian:** Data curation, Software, Formal analysis, Visualization. **Gabriel Ramos-Llordén:** Data curation, Software, Formal analysis, Visualization. **Chiara Maffei:**

Data curation, Software, Formal analysis, Visualization. **Berkin Bilgiç:** Software. **Thomas Witzel:** Software. **Jason P. Stockmann:** Methodology. **Choukri Mekkaoui:** Software, Funding acquisition. **Lawrence L. Wald:** Resources, Project administration, Funding acquisition. **Susie Yi Huang:** Investigation, Writing - original draft, Formal analysis, Writing - review & editing, Resources, Project administration, Funding acquisition. **Anastasia Yendiki:** Conceptualization, Formal analysis, Writing - original draft, Writing - review & editing, Resources, Project administration, Funding acquisition. **Boris Keil:** Methodology, Formal analysis, Writing - original draft, Writing - review & editing, Resources, Project administration, Funding acquisition.

References

Andersson, J.L., Sotiropoulos, S.N., 2016. An integrated approach to correction for off-resonance effects and subject movement in diffusion MR imaging. Neuroimage 125, 1063–1078. doi:10.1016/j.neuroimage.2015.10.019.

Augustinack, J.C., Helmer, K., Huber, K.E., Kakunoori, S., Zöllei, L., Fischl, B., 2010a. Direct visualization of the perforant pathway in the human brain with ex vivo diffusion tensor imaging. Front. Hum. Neurosci. 4, 42. doi:10.3389/fnhum.2010.00042.

Basser, P.J., 1995. Inferring microstructural features and the physiological state of tissues from diffusion-weighted images. NMR Biomed. 8 (7), 333–344. doi:10.1002/nbm.1940080707.

Basser, P.J., Mattiello, J., LeBihan, D., 1994. MR Diffusion tensor spectroscopy and imaging. Biophys. J. 66 (1), 259–267. doi:10.1016/S0006-3495(94)80775-1.

Beaujoin, J., Palomero-Gallagher, N., Boumezbeur, F., Axer, M., Bernard, J., Poupon, F., Schmitz, D., Mangin, J.-F., Poupon, C., 2018. Post-mortem inference of the human hippocampal connectivity and microstructure using ultra-high field diffusion MRI at 11.7 T. Brain Struct. Funct. 223 (5), 2157–2179. doi:10.1007/s00429-018-1617-1.

Calamante, F., Tournier, J.-D., Kurniawan, N.D., Yang, Z., Gyengesi, E., Galloway, G.J., Reutens, D.C., Connelly, A., 2012. Super-resolution track-density imaging studies of mouse brain: comparison to histology. Neuroimage 59 (1), 286–296. doi:10.1016/j.neuroimage.2011.07.014.

Conturo, T.E., Lori, N.F., Cull, T.S., Akbudak, E., Snyder, A.Z., Shimony, J.S., McKinstry, R.C., Burton, H., Raichle, M.E., 1999. Tracking neuronal fiber pathways in the living human brain. Proc. Natl. Acad. Sci. 96 (18), 10422–10427. doi:10.1073/pnas.96.18.10422.

Dhollander, T., Mito, R., Raffelt, D., Connelly, A., Montreal, 2019. Improved white matter response function estimation for 3-tissue constrained spherical deconvolution. In: Proceedings of the 27th Annual Meeting of ISMRM, p. 555.

D'Arceuil, H.E., Westmoreland, S., de Crespigny, A.J., 2007. An approach to high resolution diffusion tensor imaging in fixed primate brain. Neuroimage 35 (2), 553–565. doi:10.1016/j.neuroimage.2006.12.028.

Edelstein, W., Hardy, C., Mueller, O., 1986. Electronic decoupling of surface-coil receivers for NMR imaging and spectroscopy. J. Magn. Reson. 67 (1), 156–161. doi:10.1016/0022-2364(86)90421-X.

Edlow, B.L., Mareyam, A., Horn, A., Polimeni, J.R., Witzel, T., Tisdall, M.D., Augustinack, J.C., Stockmann, J.P., Diamond, B.R., Stevens, A., Tirell, L.S., Folkerth, R.D., Wald, L.L., Fischl, B., Van der Kouwe, A., 2019. 7 Tesla MRI of the ex vivo human brain at 100 micron resolution. Sci. Data 6 (1), 1–10. doi:10.1038/s41597-019-0254-8.

Eichner, C., Paquette, M., Mildner, T., Schlumm, T., Pléh, K., Samuni, L., Crockford, C., Wittig, R.M., Jäger, C., Möller, H.E., Friederici, A.D., Anwander, A., 2020. Increased sensitivity and signal-to-noise ratio in diffusion-weighted MRI using multi-echo acquisitions. Neuroimage 221, 117172. doi:10.1016/j.neuroimage.2020.117172.

Feinberg, D.A., Moeller, S., Smith, S.M., Auerbach, E., Ramanna, S., Glasser, M.F., Miller, K.L., Ugurbil, K., Yacoub, E., 2010. Multiplexed echo planar imaging for sub-second whole brain FMRI and fast diffusion imaging. PLoS ONE 5 (12). doi:10.1371/journal.pone.0015710.

Fritz, F., Sengupta, S., Harms, R., Tse, D., Poser, B., Roebroeck, A., 2019. Ultra-high resolution and multi-shell diffusion MRI of intact ex vivo human brains using kT-dsteam at 9.4 t. Neuroimage 202, 116087. doi:10.1016/j.neuroimage.2019.116087.

Hoult, D., 1978. The NMR receiver: a description and analysis of design. Prog. Nucl. Magn. Reson. Spectrosc. 12 (1), 41–77. doi:10.1016/0079-6565(78)80002-8.

Huang, S.Y., Tian, Q., Fan, Q., Witzel, T., Wichtmann, B., McNab, J.A., Bireley, J.D., Machado, N., Klawiter, E.C., Mekkaoui, C., Wald, L.L., Nummenmaa, A., 2020. High-gradient diffusion MRI reveals distinct estimates of axon diameter index within different white matter tracts in the in vivo human brain. Brain Struct. Funct. 225, 1277–1291. doi:10.1007/s00429-019-01961-2.

Iglesias, J.E., Insausti, R., Lerma-Usabiaga, G., Bocchetta, M., Van Leemput, K., Greve, D.N., Van der Kouwe, A., Fischl, B., Caballero-Gaudes, C., Paz-Alonso, P.M., 2018. A probabilistic atlas of the human thalamic nuclei combining ex vivo MRI and histology. Neuroimage 183, 314–326. doi:10.1016/j.neuroimage.2018.08.012.

Janssens, T., Keil, B., Farivar, R., McNab, J.A., Polimeni, J.R., Gerits, A., Arsenault, J., Wald, L.L., Vanduffel, W., 2012. An implanted 8-channel array coil for high-resolution macaque MRI at 3 T. Neuroimage 62 (3), 1529–1536. doi:10.1016/j.neuroimage.2012.05.028.

Jensen, J.H., Helpern, J.A., Ramani, A., Lu, H., Kaczynski, K., 2005. Diffusional kurtosis imaging: the quantification of non-gaussian water diffusion by means of magnetic resonance imaging. Magn. Reson. Med. 53 (6), 1432–1440. doi:10.1002/mrm.20508.

Jones, R., Grisot, G., Augustinack, J., Magnain, C., Boas, D.A., Fischl, B., Wang, H., Yendiki, A., 2020. Insight into the fundamental trade-offs of diffusion MRI from polarization-sensitive optical coherence tomography in ex vivo human brain. Neuroimage 214, 116704. doi:10.1016/j.neuroimage.2020.116704.

Keil, B., Alagappan, V., Mareyam, A., McNab, J.A., Fujimoto, K., Tountcheva, V., Triantafyllou, C., Dilks, D.D., Kanwisher, N., Lin, W., Grant, P.E., Wald, L.L., 2011. Size-optimized 32-channel brain arrays for 3 T pediatric imaging. Magn. Reson. Med. 66 (6), 1777–1787. doi:10.1002/mrm.22961.

Keil, B., Blau, J.N., Biber, S., Hoecht, P., Tountcheva, V., Setsompop, K., Triantafyllou, C., Wald, L.L., 2013. A 64-channel 3T array coil for accelerated brain MRI. Magn. Reson. Med. 70 (1), 248–258. doi:10.1002/mrm.24427.

Keil, B., Wald, L.L., 2013. Massively parallel MRI detector arrays. J. Magn. Reson. 229, 75–89. doi:10.1016/j.jmr.2013.02.001.

Kellman, P., McVeigh, E.R., 2005. Image reconstruction in SNR units: a general method for SNR measurement. Magn. Reson. Med. 54 (6), 1439–1447. doi:10.1002/mrm.20713.

Kumar, A., Edelstein, W. A., Bottomley, P. A.,. Noise figure limits for circular loop mr coils.

Lagana, M., Rovaris, M., Ceccarelli, A., Venturelli, C., Marini, S., Baselli, G., 2010. DTI parameter optimisation for acquisition at 1.5 T: SNR analysis and clinical application. Comput. Intell. Neurosci. 2010, 8. doi:10.1155/2010/254032.

Larkman, D.J., Hajnal, J.V., Herlihy, A.H., Coutts, G.A., Young, I.R., Ehnholm, G., 2001. Use of multicoil arrays for separation of signal from multiple slices simultaneously excited. J. Magn. Reson. Imaging 13 (2), 313–317. doi:10.1002/1522-2586(200102)13:2<313::AID-JMRI1045>3.0.CO;2-W.

Mahmutovic, M., Scholz, A., Kutscha, N., May, M., Schlumm, T., Möller, R., Pine, K., Edwards, L., Weiskopf, N., Brunner, D., Möller, H., Keil, B., 2021. A 64-channel brain array coil with an integrated 16-channel field monitoring system for 3T MRI. In: Proceedings of the 29th Annual Meeting of ISMRM, p. 0623.

McNab, J.A., Edlow, B.L., Witzel, T., Huang, S.Y., Bhat, H., Heberlein, K., Feiweier, T., Liu, K., Keil, B., Cohen-Adad, J., Tisdall, M.D., Folkerth, R.D., Kinney, H.C., Wald, L.L., 2013. The human connectome project and beyond: initial applications of 300 mT/m gradients. Neuroimage 80, 234–245. doi:10.1016/j.neuroimage.2013.05.074.

McNab, J.A., Jbabdi, S., Deoni, S.C., Douaud, G., Behrens, T.E., Miller, K.L., 2009. High resolution diffusion-weighted imaging in fixed human brain using diffusion-weighted steady state free precession. Neuroimage 46 (3), 775–785. doi:10.1016/j.neuroimage.2009.01.008.

Miller, K. L., Stagg, C. J., Douaud, G., Jbabdi, S., Smith, S. M., Behrens, T. E., Jenkinson, M., Chance, S. A., Esiri, M. M., Voets, N. L., Jenkinson, N., Aziz, T. Z., Turner, M. R., Johansen-Berg, H., McNab, J. A.,. Diffusion imaging of whole, post-mortem human brains on a clinical MRI scanner. NeuroImage.

Miller, K.L., Stagg, C.J., Douaud, G., Jbabdi, S., Smith, S.M., Behrens, T.E., Jenkinson, M., Chance, S.A., Esiri, M.M., Voets, N.L., Jenkinson, N., Aziz, T.Z., Turner, M.R., Johansen-Berg, H., McNab, J.A., 2011. Diffusion imaging of whole, post-mortem human brains on a clinical MRI scanner. Neuroimage 57 (1), 167–181. doi:10.1016/j.neuroimage.2011.03.070.

Modo, M., Hitchens, T.K., Liu, J.R., Richardson, R.M., 2016. Detection of aberrant hippocampal mossy fiber connections: ex vivo mesoscale diffusion MRI and microtractography with histological validation in a patient with uncontrolled temporal lobe epilepsy. Hum. Brain Mapp. 37 (2), 780–795. doi:10.1002/hbm.23066.

Mollink, J., Kleinnijenhuis, M., van Cappellen van Walsum, A.-M., Sotiropoulos, S.N., Cottaar, M., Mirfin, C., Heinrich, M.P., Jenkinson, M., Pallebage-Gamarallage, M., Ansorge, O., Jbabdi, S., Miller, K.L., 2017. Evaluating fibre orientation dispersion in white matter: comparison of diffusion MRI, histology and polarized light imaging. Neuroimage 157, 561–574. doi:10.1016/j.neuroimage.2017.06.001.

Mori, S., Zhang, J., 2006. Principles of diffusion tensor imaging and its applications to basic neuroscience research. Neuron 51 (5), 527–539. doi:10.1016/j.neuron.2006.08.012.

Okano, H., Mitra, P., 2015. Brain-mapping projects using the common marmoset. Neurosci. Res. 93, 3–7. doi:10.1016/j.neures.2014.08.014.

Pallebage-Gamarallage, M., Foxley, S., Menke, R.A., Huszar, I.N., Jenkinson, M., Tendler, B.C., Wang, C., Jbabdi, S., Turner, M.R., Miller, K.L., Ansorge, O., 2018. Dissecting the pathobiology of altered MRI signal in amyotrophic lateral sclerosis: a post mortem whole brain sampling strategy for the integration of ultra-high-field MRI and quantitative neuropathology. BMC Neurosci. 19 (1), 11. doi:10.1186/s12868-018-0416-1.

Peterson, D.M., Beck, B.L., Duensing, G.R., Fitzsimmons, J.R., 2003. Common mode signal rejection methods for MRI: reduction of cable shield currents for high static magnetic field systems. Concepts Magn. Reson. Part B Magn. Reson. Eng. 19 (1), 1–8. doi:10.1002/cmr.b.10090.

Pfefferbaum, A., Sullivan, E.V., Adalsteinsson, E., Garrick, T., Harper, C., 2004. Post-mortem MR imaging of formalin-fixed human brain. Neuroimage 21 (4), 1585–1595. doi:10.1016/j.neuroimage.2003.11.024.

Plantinga, B.R., Roebroeck, A., Kemper, V.G., Uludağ, K., Melse, M., Mai, J., Kuijf, M.L., Herrler, A., Jahanshahi, A., ter Haar Romeny, B.M., Temel, Y., 2016. Ultra-high field MRI post mortem structural connectivity of the human subthalamic nucleus, substantia nigra, and globus pallidus. Front. Neuroanat. 10, 66. doi:10.3389/fnana.2016.00066.

Pruessmann, K.P., Weiger, M., Scheidegger, M.B., Boesiger, P., 1999. SENSE: Sensitivity encoding for fast MRI. Magn. Reson. Med. 42 (5), 952–962. doi:10.1002/(SICI)1522-2594(199911)42:5<952::AID-MRM16>3.0.CO;2-S.

Ramos-Llorden, G., Lobos, R.A., Kim, T.H., Tian, Q., Tounetki, S., Witzel, T., Keil, B., Yendiki, A., Bilgic, B., Haldar, J.P., Huang, S., 2021. Improved multi-shot EPI ghost correction for high gradient strength diffusion MRI using structured low-rank modeling k-space reconstruction. In: Proceedings of the 29th Annual Meeting of ISMRM, p. 1346.

Reykowski, A., Wright, S.M., Porter, J.R., 1995. Design of matching networks for low noise preamplifiers. Magn. Reson. Med. 33 (6), 848–852. doi:10.1002/mrm.1910330617.

Roebroeck, A., Miller, K.L., Aggarwal, M., 2019. Ex vivo diffusion MRI of the human brain: technical challenges and recent advances. NMR Biomed. 32, e3941. doi:10.1002/nbm.3941.

Roebroeck, A., Sengupta, S., Bastiani, M., Schillak, S., Tramm, B., Waks, M., Lataster, A., Herrler, A., Tse, D., Poser, B., 2015. High resolution MRI neuroanatomy of the whole human brain post mortem with a specialized 9.4 T RF-coil. In: Proceedings of the Organization for Human Brain Mapping, p. 1856. doi:10.13140/RG.2.2.21380.07041.

Roemer, P.B., Edelstein, W.A., Hayes, C.E., Souza, S.P., Mueller, O.M., 1990. The NMR phased array. Magn. Reson. Med. 16 (2), 192–225. doi:10.1002/mrm.1910160203.

Scholz, A., May, M., Etzel, R., Mahmutovic, M., Kutscha, N., Wald, L.L., Yendiki, A., Keil, B., 2019. A 48-Channel ex vivo Brain Array Coil for Diffusion-Weighted MRI at 3T. In: Proceedings of the 27th Annual Meeting of ISMRM, p. 1494.

Sengupta, S., Fritz, F., Harms, R., Hildebrand, S., Tse, D., Poser, B.A., Goebel, R., Roebroeck, A., 2018. High resolution anatomical and quantitative MRI of the entire human occipital lobe ex vivo at 9.4 t. Neuroimage 168, 162–171. doi:10.1016/j.neuroimage.2017.03.039.

Setsompop, K., Fan, Q., Stockmann, J., Bilgic, B., Huang, S., Cauley, S., Nummenmaa, A., Wang, F., Rathi, Y., Witzel, T., LL, W., 2018. High-resolution in vivo diffusion imaging of the human brain with generalized slice dithered enhanced resolution: simultaneous multislice (gslider-SMS). Magn. Reson. Med. 141–151. doi:10.1002/mrm.26653.

Setsompop, K., Gagoski, B.A., Polimeni, J.R., Witzel, T., Wedeen, V.J., Wald, L.L., 2012. Blipped-controlled aliasing in parallel imaging for simultaneous multislice echo planar imaging with reduced g-factor penalty. Magn. Reson. Med. 67 (5), 1210–1224. doi:10.1002/mrm.23097.

Setsompop, K., Kimmlingen, R., Eberlein, E., Witzel, T., Cohen-Adad, J., McNab, J.A., Keil, B., Tisdall, M.D., Hoecht, P., Dietz, P., Cauley, S., Tountcheva, V., Matschl, V., Lenz, V., Heberlein, K., Potthast, A., Thein, H., Van Horn, J., Toga, A., Schmitt, F., Lehne, D., Rosen, B., Wedeen, V., Lawrence, L., 2013. Pushing the limits of in vivo diffusion MRI for the human connectome project. Neuroimage 80, 220–233. doi:10.1016/j.neuroimage.2013.05.078.

Shatil, A.S., Matsuda, K.M., Figley, C.R., 2016. A method for whole brain ex vivo magnetic resonance imaging with minimal susceptibility artifacts. Front. Neurol. 7, 208. doi:10.3389/fneur.2016.00208.

Shatil, A.S., Uddin, M.N., Matsuda, K.M., Figley, C.R., 2018. Quantitative ex vivo MRI changes due to progressive formalin fixation in whole human brain specimens: longitudinal characterization of diffusion, relaxometry, and myelin water fraction measurements at 3T. Front. Med. 5, 31. doi:10.3389/fmed.2018.00031.

Tournier, J.-D., Calamante, F., Connelly, A., Stockholm, 2010. Improved probabilistic streamlines tractography by 2nd order integration over fibre orientation distributions. In: Proceedings of the 18th Annual Meeting of ISMRM, p. 1670.

Weisskoff, R.M., 1996. Simple measurement of scanner stability for functional NMR imaging of activation in the brain. Magn. Reson. Med. 36 (4), 643–645. doi:10.1002/mrm.1910360422.

Wiesinger, F., De Zanche, N., Pruessmann, K., 2005. Approaching ultimate SNR with finite coil arrays.. In: Proceedings of the 13th Annual Meeting of ISMRM, p. 672.

Wiggins, G.C., Triantafyllou, C., Potthast, A., Reykowski, A., Nittka, M., Wald, L., 2006. 32-Channel 3 tesla receive-only phased-array head coil with soccer-ball element geometry. Magn. Reson. Med. 56 (1), 216–223. doi:10.1002/mrm.20925.

Yendiki, A., Witzel, T., Huang, S.Y., 2020. Connectome 2.0: cutting-edge hardware ushers in new opportunities for computational diffusion MRI. In: Bonet-Carne, E., Hutter, J., Palombo, M., Pizzolato, M., Sepehrband, F., Zhang, F. (Eds.), Computational Diffusion MRI. Springer, Switzerland, pp. 3–12. doi:10.1007/978-3-030-52893-5_1.

Zeng, H., 2018. Mesoscale connectomics. Curr. Opin. Neurobiol. 50, 154–162. doi:10.1016/j.conb.2018.03.003.

Received: 6 January 2021 | Revised: 10 March 2021 | Accepted: 11 March 2021

DOI: 10.1002/mrm.28791

FULL PAPER

Magnetic Resonance in Medicine

A size-adaptive 32-channel array coil for awake infant neuroimaging at 3 Tesla MRI

Anpreet Ghotra[1] | **Heather L. Kosakowski**[2] | **Atsushi Takahashi**[2] | **Robin Etzel**[1] | **Markus W. May**[1] | **Alina Scholz**[1] | **Andreas Jansen**[3,4] | **Lawrence L. Wald**[5,6] | **Nancy Kanwisher**[2] | **Rebecca Saxe**[2] | **Boris Keil**[1,4]

[1]Institute of Medical Physics and Radiation Protection, Department of Life Science Engineering, TH Mittelhessen University of Applied Sciences, Giessen, Germany

[2]Department of Brain and Cognitive Sciences and McGovern Institute, Massachusetts Institute of Technology, Cambridge, MA, USA

[3]Department of Psychiatry and Psychotherapy, University of Marburg, Marburg, Germany

[4]Center for Mind, Brain and Behavior (CMBB), Marburg, Germany

[5]Athinoula A. Martinos Center for Biomedical Imaging, Department of Radiology, Harvard Medical School, Massachusetts General Hospital, Charlestown, MA, USA

[6]Harvard-MIT Division of Health Sciences and Technology, Cambridge, MA, USA

Correspondence
Anpreet Ghotra, Institute of Medical Physics and Radiation Protection, TH Mittelhessen University of Applied Sciences, Giessen 35390, Germany.
Email: anpreet.ghotra@lse.thm.de

Funding information
MINT Foundation; MIT

Purpose: Functional magnetic resonance imaging (fMRI) during infancy poses challenges due to practical, methodological, and analytical considerations. The aim of this study was to implement a hardware-related approach to increase subject compliance for fMRI involving awake infants. To accomplish this, we designed, constructed, and evaluated an adaptive 32-channel array coil.
Methods: To allow imaging with a close-fitting head array coil for infants aged 1-18 months, an adjustable head coil concept was developed. The coil setup facilitates a half-seated scanning position to improve the infant's overall scan compliance. Earmuff compartments are integrated directly into the coil housing to enable the usage of sound protection without losing a snug fit of the coil around the infant's head. The constructed array coil was evaluated from phantom data using bench-level metrics, signal-to-noise ratio (SNR) performances, and accelerated imaging capabilities for both in-plane and simultaneous multislice (SMS) reconstruction methodologies. Furthermore, preliminary fMRI data were acquired to evaluate the in vivo coil performance.
Results: Phantom data showed a 2.7-fold SNR increase on average when compared with a commercially available 32-channel head coil. At the center and periphery regions of the infant head phantom, the SNR gains were measured to be 1.25-fold and 3-fold, respectively. The infant coil further showed favorable encoding capabilities for undersampled *k*-space reconstruction methods and SMS techniques.

Conclusions: An infant-friendly head coil array was developed to improve sensitivity, spatial resolution, accelerated encoding, motion insensitivity, and subject tolerance in pediatric MRI. The adaptive 32-channel array coil is well-suited for fMRI acquisitions in awake infants.

KEYWORDS

accelerated MRI, magnetic resonance imaging, neonatal imaging, pediatric imaging, pediatric MRI coil, phased array coil

1 | INTRODUCTION

Functional magnetic resonance imaging (fMRI) has proven valuable to noninvasively characterize adult brain functions over the last 25 years. Recently, substantial effort has been made to bring fMRI to the pediatric population, and it has already given great insight into the maturational processes that take place after birth across multiple fields of inquiry. Applications of fMRI with infants and toddlers have become a rapidly expanding field of research. However, the use of MRI during infancy and toddlerhood remains a challenging undertaking due to practical, methodological, and analytical problems that arise when imaging this young population.

While early pediatric functional brain imaging studies were conducted using sedation and anesthesia,[1] over the last 15 years, many fMRI scans with infants have been carried out during natural sleep.[2-4] Implementing task-based fMRI with awake infants poses challenges regarding infant handling, motion reduction, and subject compliance. Nevertheless, obtaining high-quality functional images from awake infants provides precise details about the early development of human perception, cognition, and behavior.[5,6]

After the first months of birth, brain development is characterized by rapid growth. In particular, the gray matter volume expands 106% in the first year,[7] and in total, the neonate's average head circumference increases from 35 to 43 cm during the first 6 months, reaching 46 cm at the end of the first year.[8] This early period is also crucial in brain development, as axonal-dendritic connections are formed, followed by myelination and neuronal specification.[9] However, postnatal brain plasticity is also associated with increased vulnerability to developing errors in normal orchestration, neuronal connectivity, and the integration of neuronal activity.

The rapid changes in head sizes raise a major concern when it comes to obtaining optimum signal reception in infant brain MRI applications during early life, where a close-fitting coil helmet design is critical to gain maximum sensitivity from high-density coil arrays. One way of achieving this goal is to use customized head coils for infants[4] or even a set of differently sized head array coils to enable use of MRI for a wider range of the pediatric population while maintaining a snug fit of the coil to the subject's head.[10] However, the latter coil concept involves some inconveniences in terms of costs and workflow. Another solution in providing close-fitting detector design is employing an arrangement of freely adjustable coil elements.[11] Nevertheless, with the need for large coil counts, this solution has some practical implications and requires substantial technical efforts in terms of geometric fixation.

A major consideration for tightly fitting coil helmets is the limitation in using conventional MRI sound protection gear for attenuating the scanner's acoustic noise. To address this, researchers use thin pediatric earmuff pads, which compromise sound attenuation, and thus, reduce the subject's overall tolerance in completing an MRI scan.

Given the small market volume for pediatric imaging, none of the commercial vendors provide state-of-the-art pediatric-sized head coils exceeding 16 channels. Therefore, both clinical and research institutions often use adult head coils when conducting pediatric brain MRI. This renders the brain suboptimal in terms of sensitivity reception and encoding capabilities for accelerated imaging. In addition, the infant's anatomy of a short neck raises difficulties in placing the subject's head at the isocenter of the adult head coil with the shoulders touching the lower end of the head coil; this prevents the infant's head from fully entering the coil.

Multiple aspects of the coil array must be addressed to bring task-based infant neuro-fMRI to the next level of sensitivity, spatial resolution, accelerated encoding, motion insensitivity, and subject tolerance. In the present work, the concept of an adjustable coil array is explored for awake infant brain imaging. We exploit the improved SNR and parallelism to accelerate image encoding, minimizing the total acquisition time and providing flexibility to collect a larger number of shorter scans.

2 | METHODS

2.1 | Coil design and construction

The 32-channel pediatric head coil was developed to accommodate head sizes for infants aged 1-18 months. Thus, a substantial and integral part of our coil design was the identification and implementation of the optimal coil helmet. While circumference statistics as a function of age are well documented,[8,12,13] there is no source of 3-dimensional (3D) head-form shapes for infants of different age groups. Therefore, our modular coil former is based on the surface contours of aligned 3D MRI pediatric head scans from 20 groups of age-matched 1-, 6-, 12-, and 18-month-old infants. Each computed average age-matched head model was scaled to the 95th percentile of the statistical corresponding head circumferences.[8]

Following the concept of "one-size-fits-all," we implemented a coil helmet design with 3 anatomical-shaped independent coil segments (Figure 1). We used a computer-aided design (CAD) software (Rhino3D V.6.0, Robert McNeel & Associates, Seattle, WA, USA) to 3D model the array coil housing. The posterior part is integrated into the coil base so that the infant can be easily laid down without any other restrictive coil parts. After the infant is placed on the posterior coil part, 2 anterior coil segments can be laterally slid in around the infant's head. This mechanism allows continuous lateral coil-to-head adaption. In the anterior-posterior (AP) direction, the helmet can be adjusted in 4 increments of 5 mm each accommodating head sizes with AP diameters from 155 to 170 mm. This facilitates MR brain imaging of newborns to infants of approximately 18 months. In the most tightest helmet setting, the coil can accommodate infants with a head circumference of up to 44 cm, corresponding to an age of 6-7 months. For newborns up to 3 months, there is a small remaining space of approximately 1 to 1.5 cm between the infant's head and the coil former. For larger head sizes, ranging from 44 to 49 cm circumference, the coil helmet allows expansion in both the left-right and AP directions (Supporting Information Figures S1 and S2).

Instead of lying flat on the patient table, we designed the coil base as an inclined cradle seat to improve the subject's overall MRI scanning compliance. The cradle was designed to accommodate toddler of 18 months. For younger (and smaller) infants, cushions can be added to raise the lower cradle part, so that the infant's head comfortably accesses the head coil.

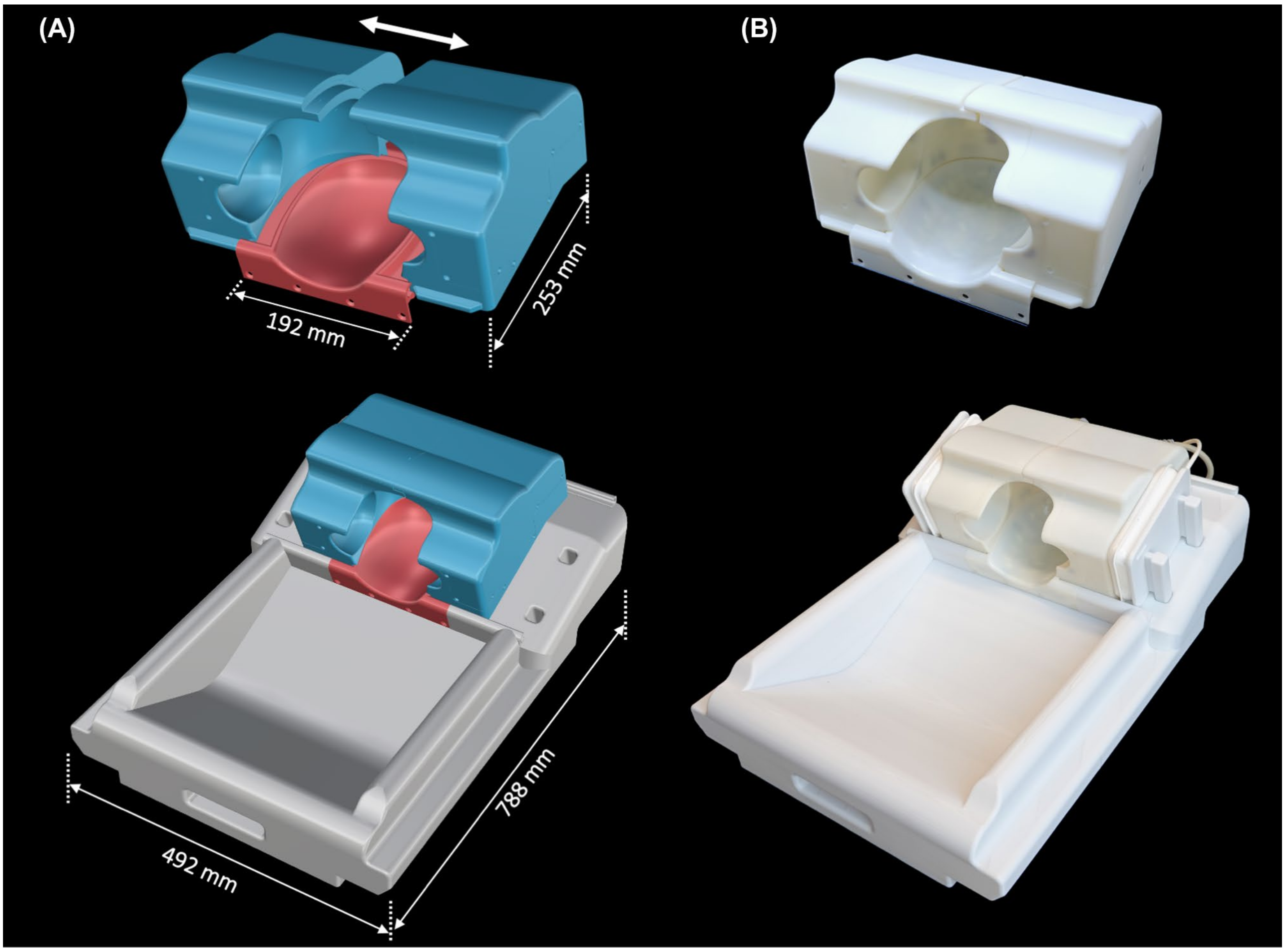

FIGURE 1 CAD design (A) and 3D printed model (B) of the adaptive array coil setup. The coil setup consists of an adjustable receiver array and an inclined cradle as a coil base. The posterior part (red) of the array coil is directly incorporated into the coil base, while the anterior parts (blue) allow adaptability to various infant head sizes (neonate to 18 months). Head immobilization is achieved using inflatable cushions, which are placed on the outer side of the anterior coil segments. The total weight of the infant coil amounts to 6.8 kg

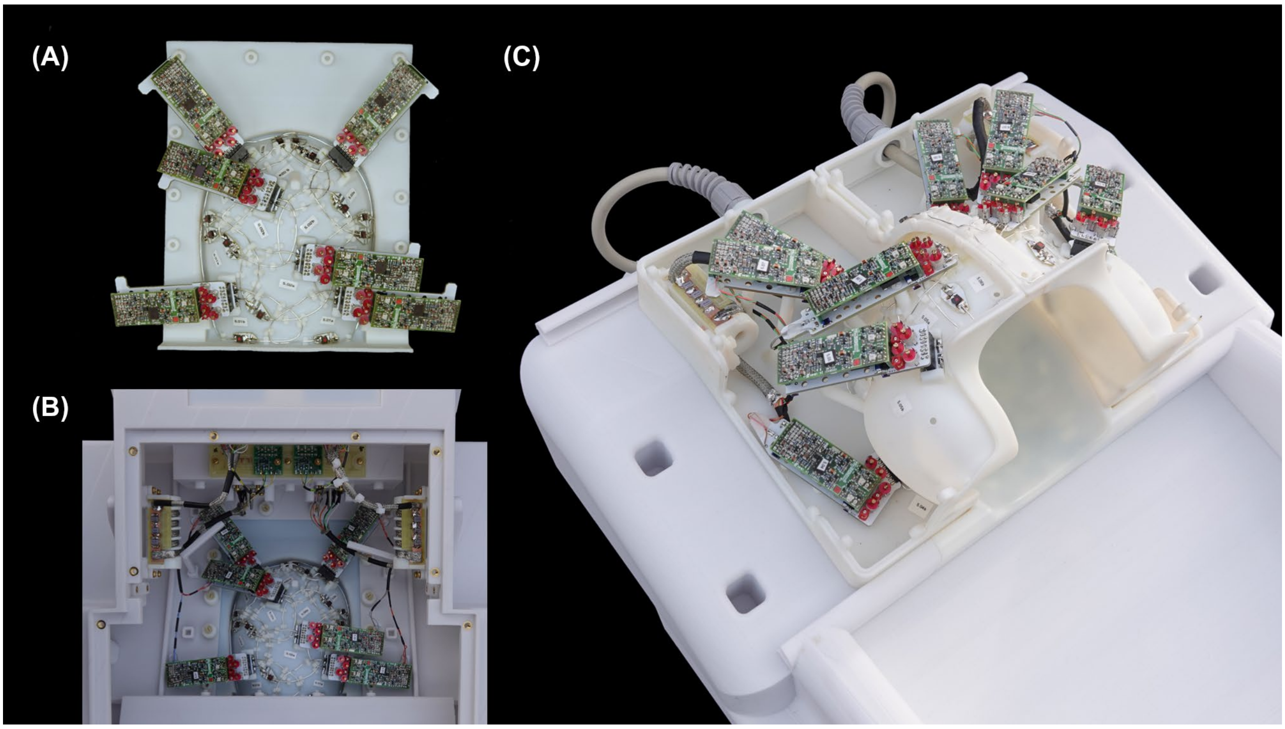

FIGURE 2 Constructed and populated coil array. The posterior coil part (A) comprises 12 coil elements, and it is integrated into the housing base (B). The 2 anterior segments (C) consist of 10 elements each and are laterally adjustable for individual infant head sizes. Integrated earmuff compartments allow the usage of bulky sound attenuation gear while maintaining a snug fit of the lateral coil array segments

When incorporating high-density head array coils with a tight fit around the subject's head, the need to provide enough accommodation for the subject's ear protection must be considered. Consequently, a critical design component was the implementation of dedicated earmuff compartments in both the right and left anterior coil housing sections. For further head immobilization, we placed inflatable cushions on the outer side of the anterior coil parts. This gentle pressure also seals the ear protection gear and reduces the infant head motion. We chose an open-faced coil topology without eye coil elements to prevent anxiety of participants and facilitate visual stimulation during task-based fMRI studies. All coil housing parts, including the covers and cradle, were 3D printed in polycarbonate (Fortus 360, Stratasys Ltd., Eden Prairie, MN, USA).

The optimum channel count for the constructed brain array was determined by the following: (a) the given geometrical constraints of the helmet, (b) the knowledge of the extent of anatomical coverage desired, and (c) the substantial loss of sample noise domination when going below a certain loop coil size. At 3 T MRI field strength, loop coil diameters of about 60 mm provide an unloaded-to-loaded Q-ratio of approximately 4, which is considered to be well sample noise dominated.[10]

Given the multiple constraints, a suitable element count for the developed coil former ranges from 30 to 34 channels. Recent advances in MR systems have ensured that nearly all 3-Tesla scanners currently installed utilize ≥ 32 receive channels. Therefore, we have implemented 32 loop elements into the constructed coil array.

We subdivided the total channel count into the posterior part with 12 elements, while the 2 anterior head parts house 10 elements each (Figure 2 and Supporting Information Figure S3). The majority of the loop elements were implemented with a diameter ranging from 58 to 67 mm. Some elements on the edges of the coil housing had to be shaped arbitrarily. The 2 larger loop elements surrounding the earmuff compartments comprise elliptical loop diameters of $d_1 = 85\,\mathrm{mm}$ and $d_2 = 91\,\mathrm{mm}$. The array layout was established using critical overlap for direct neighboring element decoupling. This geometrically decoupled structure is also maintained when nearest neighbors are located in different coil part segments. Mechanically, this was achieved by incorporating an overlapping rim structure into the interconnecting areas of the housing parts, allowing the loops on separated sections to be geometrically decoupled.

2.2 | Electronics

Each loop element was constructed from a 1.2-mm thick silver-plated copper wire. The geometrical loop layout was implemented by small standoffs, integrated into the coil former design, in which the wires snapped into the desired position. We subdivided each wire loop element into 2 segments, between which a tuning capacitor C_{T1} was soldered.

On the opposite side, we incorporated a subconnector, where the preamplifier's daughterboard was mounted (Figure 3). The matching and detuning circuitry is placed on the front end of the preamplifier board rather than soldering those components directly onto the coil former. Therefore, the daughterboard contributes as a part of the coil circuit. The daughterboards were mechanically mounted on the helmet via 3D-printed plastic standoffs.

The coil's output network comprises a series variable capacitor C_M (GFX2700NM Sprague Goodman, Westbury, NY, USA) and a capacitive voltage divider (C_{TM}, C_{T2}) (Series 11, Knowles Capacitors, Norwich, UK), where C_{TM} contributes to both tuning and matching. C_{T2} forms with the inductance L and the PIN diode D the active detuning circuit, where C_{T2} and L are set to resonance when the PIN diode (MA4P4002B-402, Macom, Lowell, MA) is forward biased. Thus, a high impedance is inserted into the loop in series. This prevents current flow at Larmor frequency during transmission. In case the active detuning fails, we have incorporated a passive detuning circuit using a pair of cross-parallel passive diodes D_X (MADP-011048-TR3000, Macom, Lowell, MA, USA) with an additional series capacitor C_D. The latter blocks the active bias current but also tunes out the extra inductance resulting from the additional length of the copper trace. For a final safety feature, we have implemented a series fuse F (1999-6000-5700, current rating: 570 mA, Data Modul AG, Munich, Germany) for passive protection against large coil currents.

The fine adjustment of the resonance frequency was achieved by carefully controlling the variable tuning capacitor C_{T3}; the combination of C_M and C_{TM} matches the coil element's output under loaded conditions to a noise-matched impedance of 50 Ω. C_M and C_{TM} also provide the necessary impedance transformation for accomplishing preamplifier decoupling.[14] In this case, C_M transforms the preamplifier's input impedance to a parallel inductance across C_{TM}. Hence, this parallel LC circuit is set to resonance and introduces a high impedance in the coil loop (Supporting Information Figure S4). In this mode, minimal current flows in the loop, and inductive coupling to other coil elements are minimized. A twin preamplifier (Siemens Healthineers AG, Erlangen, Germany) was used to connect to a pair of adjacent coil elements. The preamplifier output cables within the 3 housing segments are bundled and passed through 3 cable traps to suppress common mode currents. The cable trap formers were 3D-printed, consist of 6 sinusoidal windings, and were tuned to Larmor resonant frequency using 3 series capacitors (33 pF, 39 pF, and 43 pF).

The 2 sliding anterior coil parts have separate plugs (ODU-MAC ZERO White Line, ODU GmbH & Co. KG, Mühldorf a. Inn, Germany), which connect to the posterior cradle base instead of directly to the scanner. The cradle base is then connected to the patient table using a sliding connection mechanism integrated into the coil housing. Consequently, the infant coil setup does not require any conventional coil plugs (Figure 4), which greatly optimizes imaging workflow conditions. This feature also facilitates the process of natural sleep studies, where the infant can be prepared and settled into sleep in a separate room and then placed onto the patient's scanner table with the entire coil setup.

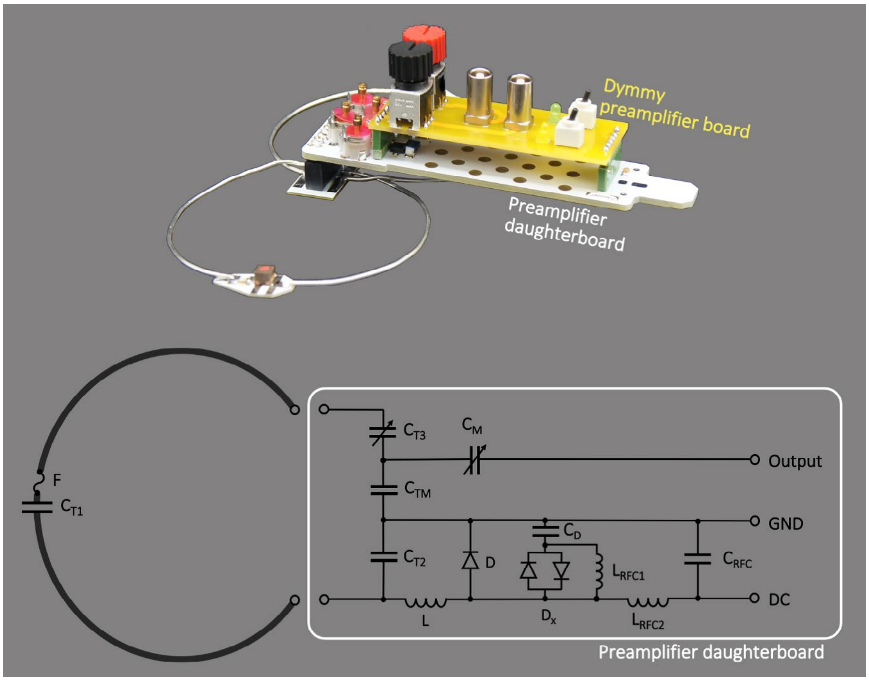

FIGURE 3 Top: Loop coil element with its daughterboard and the developed dummy preamplifier board. The coil connects with a subconnector to the daughterboard, which comprises the output circuitry of the coil. Bottom: Corresponding circuit schematic of one coil element. Values for a 65-mm dia. loop element: $C_{T1} = 18\,\text{pF}$, $C_{T2} = 56\,\text{pF}$, $C_{T3} \approx 16\,\text{pF}$, $C_{TM} = 36\,\text{pF}$, $C_M \approx 24\,\text{pF}$, $C_D = 180\,\text{pF}$, $C_{RFC} = 1\,\text{nF}$, $L \approx 25\,\text{nH}$, $L_{RFC1} = L_{RFC2} = 2.7\,\mu\text{H}$

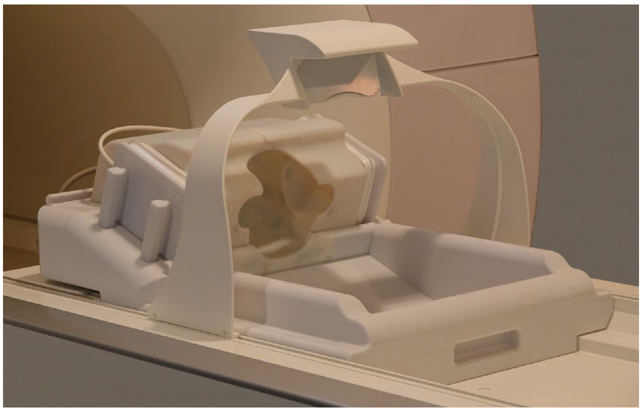

FIGURE 4 Completed infant array coil installed on the scanner's patient table. The adaptive head coil is integrated into an inclined cradle base to allow an inclined position of the infant, which ultimately improves the subject's compliance. The mirror is attached directly to the patient table and can be slid to the needed position

2.3 | Coil bench measurements

The constructed infant array was adjusted and optimized with various radiofrequency (RF) bench-level metrics using vector network analyzer equipped with a 48-channel RF switch matrix (ZNB-4 and ZN-Z84, Rohde & Schwarz GmbH & Co. KG, Munich, Germany). The unloaded-to-loaded coil quality factor ratio (Q_U/Q_L) of one representative 65-mm diameter coil element was assessed within the populated but detuned array assembly using the S_{21} double-probe method.[15] After populating the receive elements on the coil formers, the daughterboards were attached to the elements' subconnector sockets (Figure 3). All elements were pre-tuned to resonate at the Larmor frequency, and the active detuning circuitry was adjusted to switch off each element on the bench setup. We used a custom-made coil plug simulator to control each channel's detuning bias. However, the specific MRI scanner's RF architecture requires a shared bias control of 2 coil elements. Therefore, we developed a preamplifier dummy board (Figure 3), which allows the independent control of the paired coil loops. The preamplifier dummy board was designed to further provide (a) a 50 Ω termination of the loop, (b) the complex input impedance of the preamplifier, and (c) a pass-through connection for obtaining S_{11} measurement of the coil element. Each of the termination settings can be dialed in via a 3-way rotary switch. For fine adjustments, the loop under testing was brought into the tuned state, while all neighboring elements were actively detuned. By performing an S_{11} measure, we tuned and matched the coil to 123.25 MHz and 50 Ω under loaded conditions. Active detuning was adjusted by carefully controlling the variable inductance L of the active detuning circuit under a S_{21} double-probe measurement. Preamplifier decoupling was monitored with the same S_{21} measure, while the loops were terminated with the complex input impedance, emulated by the preamplifier dummy board. Small adjustment offsets of preamplifier decoupling were compensated by slightly varying the series matching capacitor C_M. Finally, all cable traps were tuned to block currents at Larmor frequency using a pair of custom-made current probes via S_{21} measurements.

2.4 | MRI acquisition and reconstruction

Initial imaging of the constructed infant array coil was carried out with a 3 Tesla MRI Scanner (MAGNETOM, Prisma, Siemens Healthineers AG, Erlangen, Germany). We used phantom imaging to determine the safety parameters, SNR, and acceleration capability metrics. Three size-matched infant head phantoms were filled with agarose and dielectrically tuned with NaCl (0.5%) and $NiCl_2$ (2.82 g/1 L H_2O) to match the human average brain tissue at 3 T. The dielectric values were measured to be $\sigma = 0.63$ S/m and $\epsilon_r = 78$ (DAK-12, Schmid & Partner Engineering AG, Zurich, Switzerland).

Initial infant in vivo images were collected in a sleep study and an awake task-based fMRI study. Proton density-weighted gradient-echo images obtained from phantom scans were acquired to compute the signal-to-noise ratio (SNR), g-factor, and noise correlations (repetition time $\mathrm{TR} = 30\,\mathrm{ms}$, echo time $\mathrm{TE} = 6\,\mathrm{ms}$, flip angle $\mathrm{FA} = 15°$, slice thickness $\mathrm{SL} = 4\,\mathrm{mm}$, number of slices $\mathrm{nSL} = 20$, matrix $\mathrm{M} = 128 \times 128$, field-of-view $\mathrm{FOV} = (160 \times 160)\,\mathrm{mm}^2$, bandwidth $\mathrm{BW} = 200\,\mathrm{Hz/pixel}$, number of averages $\mathrm{AVG} = 4$). The noise correlation was derived by the same sequence, where no RF excitation pulse was applied. The SNR maps were calculated for images combined from noise-covariance weighted root sum-of-squares (cov-RSS) of the individual channel images, where the weights utilize coil sensitivity maps and noise covariance information.[14,16] We computed the SENSE g-factor maps[17] for simultaneous multislice (SMS) imaging.[18,19] The maximum g-factor was determined after applying a 5×5 pixel sliding window filter to the g-factor maps to avoid biasing the maximum g-factor by noise singularities. These measurements were compared to a commercially available 32-channel adult head coil.

Prior to in vivo infant imaging, we performed a battery of service scans to assess coil safety for human use.[10,20] In brief, potential RF heating was measured (Fluke 61 IR Thermometer, Fluke, Everett, WA, USA) by increasing the RF power above 200% SAR, where the detuned coil and phantom were scanned for 15 minutes within a 30 μT B_1-field with a body coil's duty cycle of 10%. Potential gradient heating was assessed with ultrafast gradient readouts to induce eddy current heating from the gradient switching. For both RF and gradient heating tests, the safety watchdog was switched off for SAR and gradient stimulation, respectively. The infant coil was considered to be safety validated when the local temperature increase was under 2°C.

In vivo infant imaging was performed under the approved institutional review board (IRB) protocol at the Massachusetts Institute of Technology. Initial infant brain imaging was carried out in 2 fMRI studies with sleeping and awake infants (Figure 5). In the sleeping fMRI study, 38 infants participated, ranging from 2.0 to 11.9 weeks of age. For comparison with the adult coil, 15 infants were scanned using the constructed infant array coil, and 23 infants were scanned with the 32-channel adult head coil. Infants had adequate hearing protection, consisting of thin-layered sticky mini-muffs (first layer) surrounded by plastic shell muffs (second layer). Within hearing protection, we integrated infant-specific, MR-compatible headphones (Sensimetrics Corp., Gloucester, MA). Acoustic attenuation levels were measured using a sound meter (Svantek 979, SVANTEK Sp zo.o., Warsaw, Poland) attached to a microphone (GRAS 46AO 1/2" CCP Pressure Standard Microphone Set, GRAS Sound ″ Vibration, Holte , Denmark) with an ear and cheek simulator (GEAS 43AG, Holte , GRAS Sound & Vibration Denmark).

During the fMRI acquisitions, the sleeping infants perceived auditory stimuli, where they listened to 4 different sound conditions played at 75 dB. Infants listened to 72 seconds of auditory stimulation followed by 18 seconds of silence for as long as the infant was asleep, but no longer than 30 minutes. For the fMRI acquisition, we used an echo planar imaging (EPI) sequence ($\text{TR} = 2$ seconds, $\text{TE} = 30\,\text{ms}$, $\text{FA} = 90°$, $\text{SL} = 2\,\text{mm}$, slice gap $= 0\,\text{mm}$, 52 near-axial slices, $\text{M} = 104 \times 104$, $\text{FOV} = (208 \times 208)\,\text{mm}^2$, SMS multiband (MB) factor $= 2$) and for a structural scan, we used a motion-corrected, 3D anatomical, vNav-MPRAGE sequence[21-23] ($\text{TR} = 2520\,\text{ms}$, 4 echoes with echo time $\text{TE}_1 = 1.69\,\text{ms}$, $\text{TE}_2 = 3.55\,\text{ms}$, $\text{TE}_3 = 5.41\,\text{ms}$, $\text{TE}_4 = 7.27\,\text{ms}$ echoes combined with the root mean square, $\text{FA} = 7°$, $\text{SL} = 1\,\text{mm}$, 144 near-axial slices, $\text{M} = 160 \times 160 \times 144$, $\text{FOV} = (160 \times 160 \times 144)\,\text{mm}^3$). We analyzed the rigid body motion parameters (translation and rotation movement) from the BOLD-EPI images obtained from both head coils. First, we computed the number of volumes that were greater than 3 different thresholds (0.5, 1.0, or 2.0 mm translation or degrees of rotation). The total number of high-motion volumes for each threshold was divided by the total number of volumes to create a single number, reflecting the percentage of high-motion volumes for each subject. The percentage of high-motion volumes was averaged across subjects for each threshold.

In the awake fMRI study, 43 infants (3-9 months old) were scanned while watching videos of faces, bodies, objects, and scenes. EPI data were collected with 44 near-axial slices ($\text{TR} = 3\,\text{s}$, $\text{TE} = 30\,\text{ms}$, $\text{FA} = 90°$, $\text{SL} = 2\,\text{mm}$, slice gap $= 0\,\text{mm}$, $\text{M} = 80 \times 80$, $\text{FOV} = (160 \times 160)\,\text{mm}^2$). We also collected data from 2 infants with the same acquisition sequence used in the sleeping study ($\text{TR} = 2\,\text{s}$, $\text{TE} = 30\,\text{ms}$, $\text{FA} = 90°$, $\text{SL} = 2\,\text{mm}$, slice gap $= 0\,\text{mm}$, 52 near-axial slices, $\text{M} = 104 \times 104$, $\text{FOV} = (208 \times 208)\,\text{mm}^2$, $\text{MB} = 2$). Functional data were skull-stripped (FSL BET2), registered, intensity normalized, and spatially smoothed with a 33 mm full width at half maximum (FWHM) Gaussian kernel (FSL SUSAN). High motion volumes ($< 0.5°$ rotation or 0.5 mm rotation) were scrubbed prior to data analysis. Functional data were analyzed according to our previous study.[5] In brief, a whole-brain voxel-wise general linear model (GLM) was used with custom MATLAB scripts (R2019b, The Mathworks Inc., Natick, MA). The GLM included 4 condition regressors, 6 motion regressors, a linear trend regressor, and 5 principal component analysis (PCA) noise regressors. Condition regressors were defined as a boxcar function for the duration of the stimulus presentation. Infant inattention or sleep was accounted for using a single impulse nuisance regressor, which was defined as a boxcar function with a 1 for each TR. In case the infant was not looking at the stimuli, the condition boxcar function for the corresponding TR was changed to 0 for all condition regressors. Boxcar condition and sleep regressors were convolved with an infant hemodynamic response function (HRF) characterized by a longer time to peak

FIGURE 5 Infant in constructed 32-channel array coil. MR-safe infant-specific headphones were applied to the infant, and infants were placed comfortably in a cradle-shaped bassinet (A). Anterior coils accommodate headphones, close comfortably around the infant's head, and are held in place by inflatable pillows (B)

and a deeper undershoot compared with the standard adult HRF.[24] PCA noise regressors were computed using a method similar to GLMDenoise,[25] as defined by Deen et al.[5] Using in-house MATLAB scripts, one-subject-level contrast maps were computed as the difference between faces and scenes and a second as the difference between faces and objects.

3 | RESULTS

The majority of the 32 coil elements comprised a loop with a diameter of 65 mm, which showed a $Q_{\mathrm{UL}}/Q_{\mathrm{L}} = 4.3$ when surrounded by the 6 non-resonating neighboring elements. Thus, the constructed loops are sample noise dominated. Upon sample loading, a resonance frequency shift of −0.3 MHz was measured. For the 2 larger eye loops (elliptical shaped, $d_1 = 85$ mm and $d_2 = 91$ mm), we measured an unloaded-to-loaded Q-ratio of 8.6 and a loading frequency shift of −0.6 MHz.

The impedance matching to 50 Ω of the coil elements remained nearly constant due to the adjustability of the coil array to different size infant head phantoms. Only the smallest head phantom, which corresponds to newborns, had a small space between the coil former and phantom, resulting in a slightly underloaded matching condition (−22 dB).

The decoupling between the tuned and active detuned states provided an average isolation of (43 ± 2) dB. The interelement coupling is shown in Supporting Information Figure S5 as an S-matrix. Adjacent pairs of loops showed an average geometrical decoupling of $-(15 \pm 3)$ dB. The decoupling of the next nearest neighbors ranged from −58.4 to −13.2 dB with a mean value of −28.9 dB. All decoupling values were further reduced by (17 ± 2) dB via preamplifier decoupling. The decoupling measurements were obtained when the adaptable array coil segments were positioned for their smallest sample size (default position). Cable trap tuning was measured with a set of current probes and yielded 41 dB RF current suppression at Larmor frequency.

Figure 6 shows the comparison of SNR maps between the constructed infant head coil and the commercially available adult head coil obtained from unaccelerated images, which were combined with the covariance weighted root sum-of-square (cov-RSS) reconstruction method. Both coils were loaded with an infant head phantom filled with agarose. We measured a 2.7-fold increase in SNR in the phantom region corresponding to the infant's brain. The peripheral and central regions of the brain phantom showed 3-fold and 1.25-fold SNR gains, respectively, when the constructed coil was compared with the adult coil. The SNR comparison between 3 different coil adjustment settings with its corresponding head phantoms is shown in Supporting Information Figure S1.

The noise correlation information for both when the array coil is in its default position and when the lateral coil segments are not fully closed (for larger head sizes) are shown in Figure 7. In the default position, the noise correlation ranged from 0.2% to 38.5% with an average of 11.3%. When the coil housing was adjusted for larger head sizes, we measured an average noise correlation of 9.1% (range from 0.1% to 44.8%). In comparison, when the small infant head phantom was

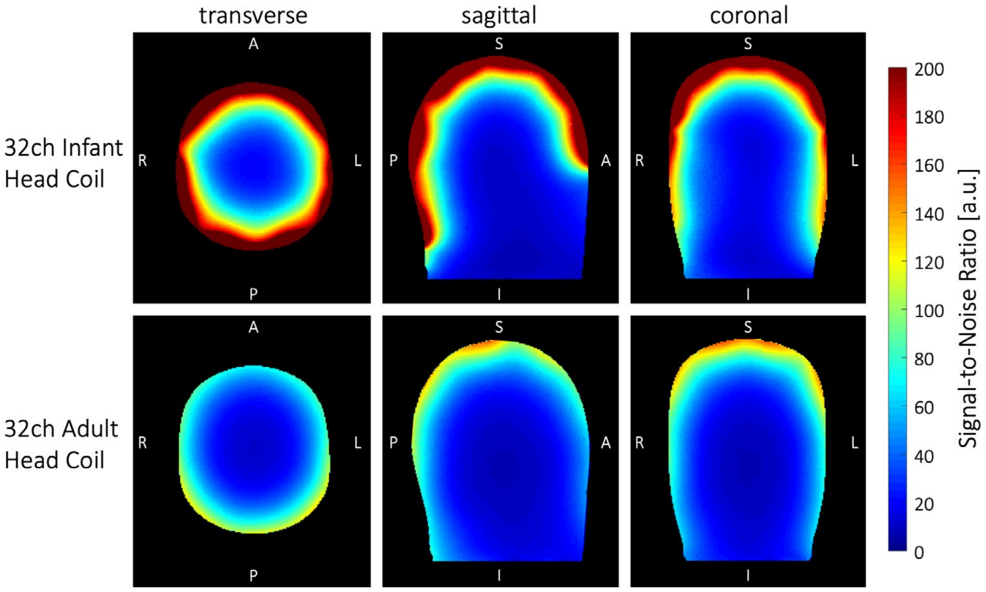

FIGURE 6 SNR comparison between the constructed 32-channel infant head coil and the commercial 32-channel adult head coil obtained from unaccelerated phantom images combined with the cov-RSS reconstruction method. The infant coil array shows a 2.7-fold SNR increase across the whole brain region in comparison to the adult head coil. In the peripheral and central regions, the infant coil outperforms the adult coil by 3-fold and 1.25-fold SNR gains, respectively

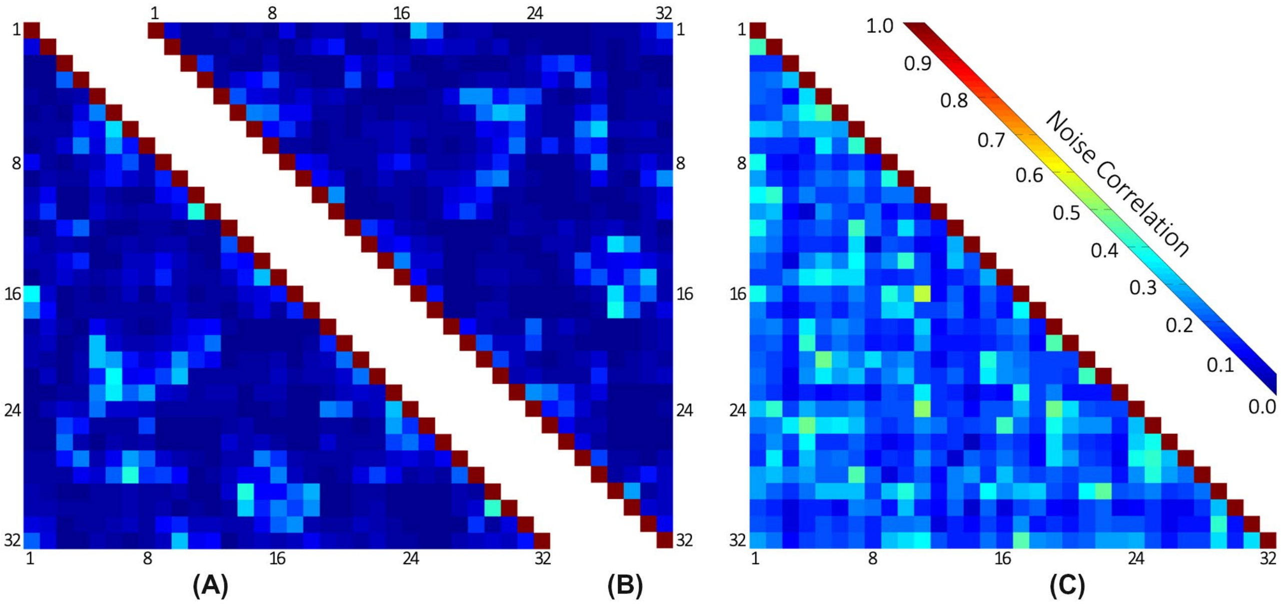

FIGURE 7 Noise correlation comparison between the infant array (A) when it is in its default position (smallest adaptive size), (B) when it is adjusted for larger head sizes, and (C) when the infant head phantom is placed in the adult head array coil. The average off-diagonal matrix elements for (A), (B), and (C) are 11.3 % (range 0.2 %-38.5 %), 9.1 % (range 0.1 %-44.8 %), and 21.6 % (range 6.3 %-61.4 %), respectively

placed in the adult head coil, a highly increased average noise correlation of 21.6% was observed (range from 6.3% to 61.4%).

Since modern neuroimaging takes advantage of the recently introduced accelerated SMS imaging technique, we particularly evaluated the array coil's encoding characteristics for multislice acquisitions (Figure 8). For an acceleration MB factor of 6, the 32-channel infant coil showed almost no noise amplification during the SMS reconstruction method (max. $g_{\max}$-factor across 6 slices = 1.06), where the 32-channel adult coil showed a maximum SMS $g_{\max}$-factor of 1.22. When SMS is combined with in-plane undersampled k-space acceleration techniques, acceleration factors of $MB = 4$ and $R = 2$ are feasible. Here, we measured a peak noise amplification of $g_{\max} = 1.2$ and $g_{\max} = 2.5$ with the infant coil and with the adult coil, respectively.

The 32-channel infant array coil passed all safety tests. The amount of power from the RF body coil dissipated in the detuned array was less than 5 %. Component heating obtained from high duty cycle RF fields and eddy currents were measured to be less than 2 ° C.

The hearing protection attenuated 19.8 dB at 500 Hz, 23.3 dB at 1 kHz, 26.8 dB at 4 kHz, and 28.1 dB at 10 kHz. Thus, passing the heating and sound level tests, the 32-channel infant coil was approved for in vivo infant MRI measurements.

Figure 9 shows the comparison of infant head motion using the 32-channel adult coil and the 32-channel constructed infant coil during the sleeping auditory fMRI study. Infants placed in the dedicated adaptive head coil showed substantial lower head motion when compared with the adult coil. When the infants fell asleep, we collected enough data for data analysis (≥ 90TRs) from 91% of infants in the adult coil and 100% of infants in the infant coil.

Figure 10 shows preliminary data from a single awake infant (6 months old) with 13.5 minutes of low-motion data on the 2 following canonical contrasts: faces > scenes and faces > objects. The high-resolution EPI images obtained from the infant array coil enabled the acquisition of high-quality functional data of an awake infant performing a task-based study. Of the 43 infants who were recruited for the awake study, we collected enough low-motion data ($< 0.5°$ rotation or 0.5 mm rotation) for analysis (≥ 95TRs) from 23 out of 43 infants (53%).

4 | DISCUSSION

In this study, we designed, constructed, and evaluated a size-adaptive 32-channel infant head coil, which was especially developed for scanning awake infants. The coil was compared to a commercially available adult head coil and evaluated with bench tests and phantom imaging. Although 32-channel head array coils are well understood at 3 T,[10,20,26-30] there are additional challenges when using the concept of an adaptable head coil design for awake infants. Several design considerations had to be addressed for a functional coil former when imaging this young population. First, a convenient segmentation of the coil former needed to be implemented. To provide easy coil handling while the infant is placed inside the head coil, we subdivided the coil former into 3 segments. The posterior coil part is anatomically shaped to adapt to the occipital lobe of the infant's head, while the 2 anterior housing

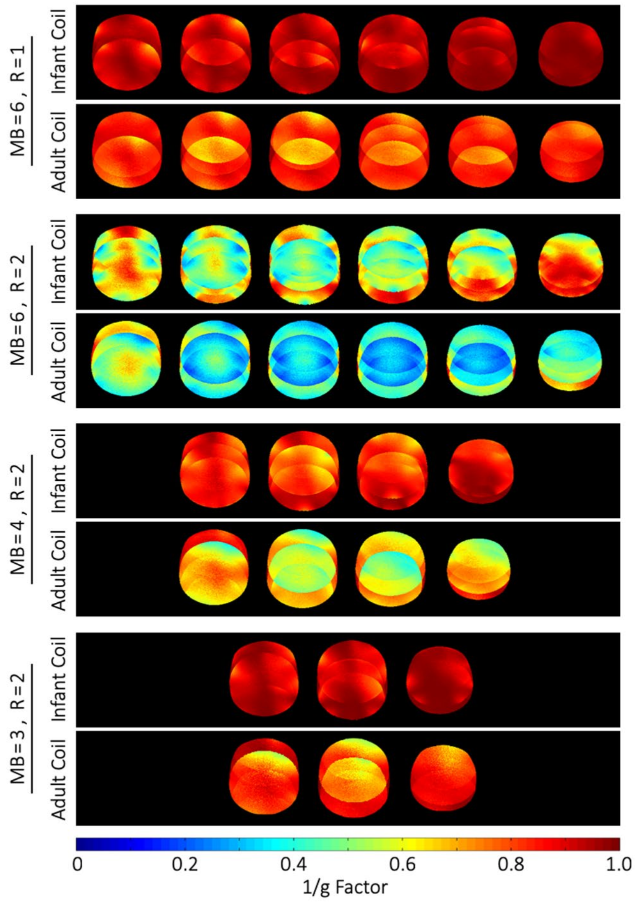

FIGURE 8 Comparison of accelerated image encoding capabilities when using simultaneous multislice (SMS) reconstruction techniques. The constructed infant head coil shows substantially lower noise amplification during SMS or combined SMS/in-plane acceleration

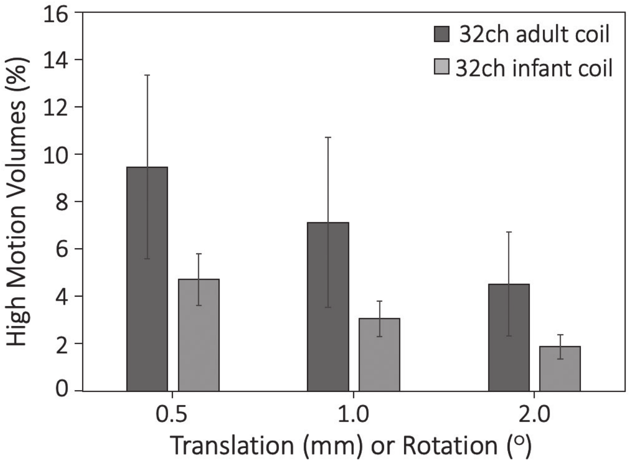

FIGURE 9 Subject volume-to-volume motion in 32-channel adult and 32-channel infant coils. Infants participated in a sleeping auditory fMRI study. Headphones were applied, and infants were placed in either a standard 32-channel adult coil ($n = 23$) or the 32-channel infant coil ($n = 15$). Data were collected using the same EPI, and volume-to-volume motion (mm of translation and degrees of rotation) was calculated. Infants scanned with the adult coil had a higher average percentage of volumes that exceeded motion thresholds at 0.5 mm (mean = 9.5, s.e.m. = 3.8), 1.0 mm (mean = 7.1, s.e.m. = 3.6), and 2.0 mm (mean = 4.5, s.e.m. = 2.2) than the infant coil at 0.5 mm (mean = 4.7, s.e.m. = 1.1), 1.0 mm (mean = 3.1, s.e.m. = 0.7), and 2.0 mm (mean = 1.9, s.e.m. = 0.5)

parts are laterally adjustable. This 3-segment design provides a compromise between a high degree of geometrical adaptability, and it greatly simplifies the handling of the coil setup on the scanner's patient table.

Maintaining a tight fit of the 32 channels around the subject's head is critical in gaining SNR. However, it potentially limits the usage of proper ear protection. Therefore, we needed to rethink how to incorporate the ear protection gear into the helmet. By implementing compartments in the lateral housing parts, we could maintain a snug fit of the coil and simultaneously ensure appropriate sound protection by using thin-layered mini-muffs and additional plastic shell muffs. In total, we obtained a reduction of acoustic noise ranging from 19.8 dB (500 Hz) to 28.1 dB (10 kHz) for the MRI relevant acoustic frequencies. The inflatable cushions have proven valuable for firmly sealing the earmuffs and achieving a close fitting of the array coil. For accomplishing higher completion rates of infant MRI scans, a critical design component was the incorporation of an inclined cradle seat. In this position, the infant can maintain eye contact with parents during the setup process on the patient's table. According to our infant MRI scan experiences obtained from initial studies, the infant favors the inclined position over the regular supine position, which is typically used during adult MRI brain examinations. In general, this position of the infant is similar to that in a car seat, which infants and toddlers are already used to.

When a head coil former is subdivided into multiple segments and employs 32 small receive loop elements, several technical issues need to be addressed. Distributing the loops while maintaining the geometrically overlapped regions across coil former segments becomes more difficult. The mechanical implementation of the housing splits was accomplished by a rim structure allowing neighboring loop elements of adjacent coil former segments to overlap. Consequently, the geometrically given constraints forced many loop elements within the array to be non-circular and to bend over the housing's rim structure.

The capability of the array to adapt to different head sizes changes the critical overlap in the region of the housing splits. While the geometrical overlap was optimized at the default housing position (smallest head size), the critical overlap could clearly not be maintained when the array coil was adjusted for larger head sizes. This yielded a slight increase of coil coupling between adjacent loops across the housing segments, which could be seen in a noise correlation rise of approximately 6 dB for affected loop pairs. The established preamplifier decoupling of 17 dB provides enough overhead to prevent the negative impact of losing the coil's load impedance of 50 Ω because

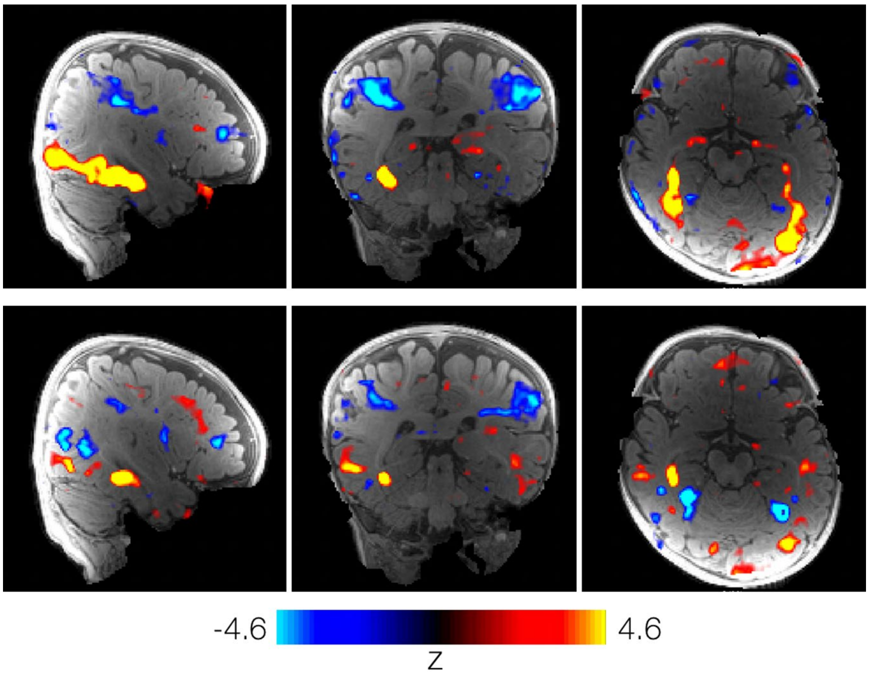

FIGURE 10 Comparison of 2 canonical contrast faces > scenes (top) and faces > objects (bottom) in an example subject. Data were collected using EPI sequence with $MB = 2$ from an awake 6-month-old infant watching colorful videos of faces, bodies, objects, and scenes. After motion scrubbing, 13.5 minutes of data were available for inclusion in the analysis. Face activation (red) is in the same areas for both the contrast of faces > scenes (top) and faces > objects (bottom). Similar data were collected from other subjects

of the changed and increased mutual inductive coupling. Thus, it is still possible to maintain the critical load impedance to drive the preamplifier with its lowest noise figure. The slightly increased coupling can then be compensated by incorporating the noise covariance statistics in the image combination algorithm. Interestingly, while observing a higher noise correlation of the cross housing adjacent loop pairs, the average noise correlation decreased by 2.2% when the coil setup was adjusted for larger head sizes. This can potentially be attributed to the overall larger geometrical distance between coil elements within the housing subdivisions.

However, when placing a relatively small head size into the adult head coil, the small head size significantly underloads the coil array. This negatively affects the matching of the coil elements, which yields a suboptimal noise figure of the preamplifier's performance. Furthermore, the underloaded condition increases the *Q*-factor of the adult coil's elements, which causes increased intercoil element coupling. This can be seen in an elevated level of the average noise correlation.

As we have shown in previous pediatric brain studies,[5,10,31,32] a dedicatedly designed tight-fitting array coil for the pediatric population provides substantial SNR benefits over adult head coils. Our constructed adjustable array coil shows similar results. On average, the infant coil outperforms the adult head coil by a factor of 2.7 of SNR gain in the brain region. The improved SNR can be invested into smaller voxel sizes, providing MR brain images with higher resolution. Furthermore, the loss of critical coil overlap between the split segments of the expanded array did not negatively impact the overall SNR performance, indicating that the pre-whitening process of the cov-RSS image reconstruction method compensated well for the increased couplings. In the widest coil helmet setting, the small gap between the segments slightly modulated the SNR pattern at the periphery of the phantom. However, small gaps between loop elements are not considered critical in array coils, as can be seen in a very common head coil design, the gapped-array design.[33]

The enhanced performance in parallel imaging encoding can be attributed to the smaller loop sizes and to the close-fitting array. In particular, this improves the steepness of the sensitivity profiles (eg, SENSE) in the signal given area or the synthesis of the spatial harmonics for *k*-space-based reconstruction techniques (eg, GRAPPA). The literature clearly shows *g*-factor improvements by employing a higher channel count. However, in infant brain imaging, we can achieve similar improvements by reducing the overall loop diameters while keeping the channel count unaltered.

Recently, SMS imaging has been introduced to accelerate image acquisitions with minimal penalty of SNR loss. In advanced functional neuroimaging, the SMS technique is combined with regular in-plane parallel imaging methods to take advantage of the shortened echo train to minimize image distortion during EPI fMRI scans. Hence, our constructed infant coil was optimized to provide sufficient encoding power in both slice direction and 2-dimensional in-plane directions. The SMS *g*-factor maps show substantial improvements using the infant array coil when compared with the adult head coil. Thus, the developed coil is well-suited to accelerate image encoding and to shorten overall image acquisition time, which has proven critical to increase the completion rate when performing MR infant neuroimaging.

Imaging the pediatric population in both clinical and research settings remains a challenging undertaking because of methodological requirements. One of the biggest constraints in completing a pediatric fMRI scan is associated with motion artifacts. Due to mechanical advances, the developed infant coil setup increased infants' comfort with the inclined position and reduced the range of allowable head motion. However, for further improvement of motion restriction during fMRI scans, prospective motion compensation techniques can be combined with our developed infant array coil. Currently established motion correction techniques, which show promising results, use optical methods to detect the subject's head movement. Since we designed the coil with an open-faced topology, it could potentially facilitate optical prospective motion compensation methods.

5 | CONCLUSIONS

By optimizing the shape and functionality of an infant brain array coil to allow head size adaptability, high-level sound protection, and head motion restriction, we improved infant brain MRI in terms of sensitivity, spatial resolution, and accelerated encoding capabilities. Furthermore, we changed the paradigm of imaging infants from a flat supine position to a half-seated position; combined with the coil's integrated ear protection, this increased the subject's tolerance for undergoing MRI neuroexaminations. We could demonstrate SNR gains, fast image encoding power, and improved scan completion rates by capitalizing on technical advances for both coil array technology and mechanical features that were tailored to the infant population.

DATA AVAILABILITY STATEMENT

The data that support findings of this study are openly available in github at https://github.com/keyarray/infantmricoil, reference number.[34]

ORCID

Anpreet Ghotra http://orcid.org/0000-0001-6445-9062
Heather L. Kosakowski http://orcid.org/0000-0001-5689-0426
Atsushi Takahashi http://orcid.org/0000-0002-5182-4320
Robin Etzel http://orcid.org/0000-0002-8783-589X
Markus W. May https://orcid.org/0000-0003-3869-9681
Alina Scholz https://orcid.org/0000-0002-3324-6889
Lawrence L. Wald http://orcid.org/0000-0001-8278-6307
Nancy Kanwisher http://orcid.org/0000-0003-3853-7885
Boris Keil http://orcid.org/0000-0003-0805-8330

REFERENCES

1. Konishi Y, Taga G, Yamada H, Hirasawa K. Functional brain imaging using fMRI and optical topography in infancy. *Sleep Med*. 2002;3(Suppl 2):S41-S43.
2. Dinstein I, Pierce K, Eyler L, Solso S, Malach R, Behrmann M, Courchesne E. Disrupted neural synchronization in toddlers with autism. *Neuron*. 2011;70:1218-1225.
3. Damaraju E, Caprihan A, Lowe JR, Allen EA, Calhoun VD, Phillips JP. Functional connectivity in the developing brain: a longitudinal study from 4 to 9 months of Age. *Neuroimage*. 2014;84:169-180.
4. Hughes EJ, Winchman T, Padormo F, Teixeira R, Wurie J, Sharma M, Fox M, Hutter J, Cordero-Grande L, Price AN, Allsop J, Bueno-Conde J, et al. A dedicated neonatal brain imaging system. *Magn Reson Med*. 2017;78:794-804.
5. Deen B, Richardson H, Dilks DD, Takahashi A, Keil B, Wald LL, Kanwisher N, Saxe R. Organization of High-Level Visual Cortex in Human Infants. *Nat Commun*. 2017;8:13995.
6. Ellis CT, Skalaban LJ, Yates TS, Bejjanki VR, Córdova NI, Turk-Browne NB. Re-imagining fMRI for awake behaving infants. *Nat Commun*. 2020;11:4523.
7. Gilmore JH, Shi F, Woolson SL, Knickmeyer RC, Short SJ, Lin W, Zhu H, Hamer RM, Styner M, Shen D. Longitudinal development of cortical and subcortical gray matter from birth to 2 years. *Cereb Cortex*. 2012;22:2478-2485.
8. WHO. *The WHO Child Growth Standards*. https://www.who.int/tools/child-growth-standards/standards/head-circumference-for-age. Accessed April 1, 2005.
9. Poduslo SE, Jang Y. Myelin development in infant brain. *Neurochem Res*. 1984;9:1615-1626.
10. Keil B, Alagappan V, Mareyam A, McNab JA, Fujimoto K, Tountcheva V, Triantafyllou C, Dilks DD, Kanwisher N, Lin W, Grant PE, Wald LL. Size-Optimized 32-channel brain arrays for 3 T pediatric imaging. *Magn Reson Med*. 2011;66:1777-1787.
11. Rios NL, Foias A, Lodygensky G, Dehaes M, Cohen-Adad J. Size-Adaptable 13-channel receive array for brain MRI in human neonates at 3 T. *NMR in Biomedicine*. 2018;31:e3944.
12. Nellhaus G. Head circumference from birth to eighteen years. Practical composite international and interracial graphs. *Pediatrics*. 1968;41:106-114.
13. Roche AF, Mukherjee D, Guo SM, Moore WM. Head circumference reference data: birth to 18 years. *Pediatrics*. 1987;79:706-712.
14. Roemer PB, Edelstein WA, Hayes CE, Souza SP, Mueller OM. The NMR phased array. *Magn Reson Med*. 1990;16:192-225.
15. Hoult DI, The NMR. Receiver: a description and analysis of design. *Prog Nucl Magn Reson Spectrosc*. 1978;12:41-77.
16. Kellman P, McVeigh ER. Image reconstruction in SNR units: a general method for SNR measurement. *Magn Reson Med*. 2005;54:1439-1447.
17. Pruessmann KP, Weiger M, Scheidegger MB, Boesiger P. SENSE: sensitivity encoding for fast MRI. *Magn Reson Med*. 1999;42:952-962.
18. Setsompop K, Gagoski BA, Polimeni JR, Witzel T, Wedeen VJ, Wald LL. Blipped-Controlled Aliasing in Parallel Imaging for Simultaneous Multislice Echo Planar Imaging with Reduced g-Factor Penalty. *Magn Reson Med*. 2012;67:1210-1224.
19. Feinberg DA, Moeller S, Smith SM, Auerbach E, Ramanna S, Gunther M, Glasser MF, Miller KL, Ugurbil K, Yacoub E. Multiplexed echo planar imaging for sub-second whole brain FMRI and fast diffusion imaging. *PLoS ONE*. 2010;5:e15710.
20. Keil B, Blau JN, Biber S, Hoecht P, Tountcheva V, Setsompop K, Triantafyllou C, Wald LL. A 64-channel 3T array coil for accelerated brain MRI. *Magn Reson Med*. 2013;70:248-258.
21. van derKouwe AJW, Benner T, Salat DH, Fischl B. Brain morphometry with multiecho MPRAGE. *Neuroimage*. 2008;40:559-569.
22. Tisdall MD, Hess AT, Reuter M, Meintjes EM, Fischl B, van der Kouwe AJW. Volumetric vavigators (vNavs) for prospective motion correction and selective reacquisition in neuroanatomical MRI. *Magn Reson Med*. 2012;68:389-399.

23. Tisdall MD, Reuter M, Qureshi A, Buckner RL, Fischl B, van der Kouwe AJW. Prospective motion correction with volumetric navigators (vNavs) reduces the bias and variance in brain morphometry induced by subject motion. *Neuroimage*. 2016;127:11-22.
24. Arichi T, Fagiolo G, Varela M, Melendez-Calderon A, Allievi A, Merchant N, Tusor N, Counsell SJ, Burdet E, Beckmann CF, Edwards AD. Development of BOLD signal hemodynamic responses in the human brain. *Neuroimage*. 2012;63:663-673.
25. Kay KN, Rokem A, Winawer J, Dougherty RF, Wandell BA. GLMdenoise: a fast, automated technique for denoising task-based fMRI data. *Front Neurosci*. 2013;7:247.
26. Keil B, Wald LL. Massively parallel MRI detector arrays. *J Magn Reson*. 2013;229:75-89.
27. Farivar R, Grigorov F, van der Kouwe AJ, Wald LL, Keil B. Dense, Shape-Optimized Posterior 32-Channel Coil for Submillimeter Functional Imaging of Visual Cortex at 3T. *Magn Reson Med*. 2016;76:321-328.
28. Chu YH, Hsu YC, Keil B, Kuo WJ, Lin FH. A 32-channel head coil array with circularly symmetric geometry for accelerated human brain imaging. *PLoS One*. 2016;11.
29. Wiggins GC, Triantafyllou C, Potthast A, Reykowski A, Nittka M, Wald LL. 32-channel 3 Tesla receive-only phased-array head coil with soccer-ball element geometry. *Magn Reson Med*. 2006;56:216-223.
30. Lattanzi R, Grant AK, Polimeni JR, Ohliger MA, Wiggins GC, Wald LL, Sodickson DK. Performance evaluation of a 32-element head array with respect to the ultimate intrinsic SNR. *NMR Biomed*. 2010;23:142-151.
31. Cohen MA, Dilks DD, Koldewyn K, Weigelt S, Feather J, Kell AJ, Keil B, Fischl B, Zöllei L, Wald L, Saxe R, Kanwisher N. Representational similarity precedes category selectivity in the developing ventral visual pathway. *Neuroimage*. 2019;197:565-574.
32. Richardson H, Gweon H, Dodell-Feder D, Malloy C, Pelton H, Keil B, Kanwisher N, Saxe R. Response patterns in the developing social brain are organized by social and emotion features and disrupted in children diagnosed with autism spectrum disorder. *Cortex*. 2020;125:12-29.
33. Ledden PJ, Mareyam A, Wang S, van Gelderen P, Duyn J. 32-channel receive-only SENSE array for brain imaging at 7T. In Proceedings of the International Society for Magnetic Resonance in Medicine, Berlin, Germany, 2007. #242.
34. Keil B. *Github Repository*. 2021. https://github.com/keyarray/infantmricoil.

SUPPORTING INFORMATION

Additional Supporting Information may be found online in the Supporting Information section.

FIGURE S1 Adjustment mechanism for infant head sizes and corresponding SNR comparison. A, For newborns up to 2 months, the coil is not entirely filled and a small space of 1-1.5 cm remains between the head and the coil former. In this case, the coil is in the narrowest helmet setting. B, In the same coil setting, the coil can accommodate infants with a head circumference of up to 44 cm (equivalent to 6-8 months). C, For larger head sizes, the coil former allows expansion in the left-right and anterior-posterior directions, essentially losing the critical overlap of adjacent loops across the housing segments and causing small gaps. The latter slightly modulates the SNR pattern at these specific locations on the periphery of the phantom. D, The 3 representative head sizes of a, b, and c are positioned at the center of the 32-channel adult coil for direct dimensional comparison. The exact dimensions of the adult coil housing were obtained from a CT scan and redrawn in the CAD program

FIGURE S2 Adaptability of the 32-channel infant coil in the anterior-posterior direction. In the standard helmet position (tightest fit), the array coil provides 155 mm of anterior-posterior length (A). The coil segments can optionally also run on top of the rails at the back (B) or at the front (C). This allows an increase in helmet size of 5 and 10 mm, respectively. When the coil segments are placed on top of both rail structures, the helmet size can be increased by a maximum of 15 mm. This setup allows head circumferences of up to 49 cm to be accommodated

FIGURE S3 Loop configuration of the constructed infant 32-channel coil array. The posterior coil former segment consists of 12 loop elements (pink). Each lateral segments (blue and green) comprise 10 loop coils

FIGURE S4 Impedance transformation circuitry for a representative loop element with 65 mm diameter. The resonance is set to Larmor with $C_{\mathrm{T1}} = 8.7\,\mathrm{pF}$, $C_{\mathrm{T2}} = 56\,\mathrm{pF}$, and $C_{\mathrm{TM}} = 36\,\mathrm{pF}$. The coil impedance Z_c is preset by the chosen value of C_{TM} and further transformed to $Z_0 = 50\,\Omega$ with the series matching capacitor $C_{\mathrm{M}} = 24\,\mathrm{pF}$. Preamplifier decoupling is established by transforming the complex input impedance of the preamplifier $Z_{\mathrm{p}} = (8 + j87)\,\Omega$ via $C_{\mathrm{M}} = 24pF$ to a parallel inductance Z_1 across C_{TM}. This parallel *LC* circuit is set to resonate at the Larmor frequency causing a high series impedance in the coil loop

FIGURE S5 S-matrix assessment of the infant 32-channel coil. The S-matrix was measured with an 48-channel RF switch matrix VNA, when the array coil was in its default position and loaded with an agar infant head phantom. The diagonal matrix elements represent the matching of each loop coil, ranging from −26.3 to −34.1 dB. The off-diagonal matrix elements show the inductive coupling between the loop coils, ranging from −58.4 to −13.2 dB with a mean of −28.9 dB. Note, the inter-element coupling was measured when each loop coil was terminated with 50 Ω using the RF switching matrix. In the actual setup, the coupling between the coils is further reduced by terminating the coil with its preamplifier which establishes the preamplifer decoupling

How to cite this article: Ghotra A, Kosakowski HL, Takahashi A, et al. A size-adaptive 32-channel array coil for awake infant neuroimaging at 3 Tesla MRI. *Magn Reson Med*. 2021;86:1773–1785. https://doi.org/10.1002/mrm.28791